UNIVERSITY OF CALIFORNIA SAN DIEGO

Analysis of Cardiovascular Disease using Cardiac Computed Tomography and Deep Learning

A dissertation submitted in partial satisfaction of the

requirements for the degree Doctor of Philosophy

in

Bioengineering

by

Zhennong Chen

Committee in charge:

Professor Elliot McVeigh, Chair
Professor Francisco Contijoch
Professor Albert Hsiao
Professor Kevin King
Professor Andrew McCulloch

2022

The Dissertation of Zhennong Chen is approved, and it is acceptable in quality and form for publication on microfilm and electronically.

University of California San Diego

2022

DEDICATION

To my parents for their unconditional love and support through it all

TABLE OF CONTENTS

Dissertation Approval Page iii

Dedication iv

Table of Contents v

List of Abbreviations x

List of Figures xii

List of Tables xv

Acknowledgements xvi

Vita xviii

Abstract of the Dissertation xx

Chapter 1: Background 1

1.1 Cardiovascular Disease 1

1.2 Left Ventricle and its Function 2

1.3 Non-invasive Cardiac Imaging: Different Modalities 4

1.3.1 Anatomical Imaging 4

1.3.2 Functional Imaging 7

1.4 Quantification Techniques 10

1.4.1 Coronary Stenosis Quantification 11

1.4.2 Regional Myocardial Strain Quantification 13

1.5 Deep Learning in CT 14

1.5.1 Deep Learning in CAD 16

1.5.2 Deep Learning in Myocardial Function Analysis 17

1.6 Thesis Outline 19

Chapter 2: Precise Measurement of Coronary Stenosis Diameter with CCTA Using CT Number Calibration 22

2.1 Introduction 22

2.2 Materials and Methods 23

2.2.1 Hole phantom 23

2.2.2 Patient derived vessel stenosis phantom 24

2.2.3 CT imaging protocols 26

2.2.3.1 CT imaging during phantom motion 27
2.2.4 Creation of calibration curves from the 3D printed hole phantom 28
2.2.4.1 Measurement of vessel intraluminal maximum voxel value – IMVV 28
2.2.4.2 Full Width at Half Maximum Determination, D_{FWHM} 28
2.2.4.3 Theoretical derivation of CT number calibration curve 28
2.2.4.4 Empirical calibration curve 29
2.2.5 Segmentation of lesions in the vessel stenosis phantom 30
2.2.6 Estimation of the vessel diameter using the CT-number-Calibrated diameter technique, D_C 31
2.2.6.1 Vessel diameter estimation in larger vessels 32
2.2.6.2 Vessel diameter estimation in smaller vessels 32
2.2.7 Comparison of D_{gt}, D_{FHWM}, D_C 33
2.3 Results 33
2.3.1 Example CT number calibration curve derived from the hole phantom 33
2.3.2 Comparison of theoretical and empirical CT number calibration curve 34
2.3.3 CT number calibration curve is CT acquisition parameter dependent 35
2.3.4 Motion artifacts and motion correction in CT number calibration curve 39
2.3.5 FWHM calibration curve from hole phantom 39
2.3.6 Estimation of vessel diameter in the vessel stenosis phantom 41
2.4 Discussion 43
2.4.1 Main Findings 43
2.4.1.1 The Definition of cutoff diameter 44
2.4.1.2 Calibration curves are CT acquisition parameter dependent 44
2.4.1.3 CT-number-Calibrated diameter in moving objects 45
2.4.2 Accuracy of vessel diameter measurement is important for FFR_{CT} 46
2.4.3 Limitations 47
2.4.4 Conclusion 48
2.5 Acknowledgement 49
Chapter 3: Thresholding of Regional Shortening Measured from 4D Cardiac CT Angiograms Accurately Detects the Presence of LV Wall Motion Abnormalities 50

3.1 Introduction 50
3.2 Materials and Methods 51
3.2.1 CT data collection 51
3.2.2 Segmental wall motion abnormality visual labels 53
3.2.3 Quantitative image analysis – Pipeline of RS_{CT} measurement 54
3.2.3.1 Image processing 54
3.2.3.2 Image analysis 54
3.2.4 Data split 55
3.2.5 RS_{CT} optimal threshold 55
3.2.6 Data adequacy 56
3.2.7 Interobserver agreement 57
3.2.8 Statistical evaluation 57
3.3 Results 58
3.3.1 Data info 58
3.3.2 Performance of RS_{CT} for detection of wall motion abnormality 59
3.3.2.1 Histograms of peak RS_{CT} in the training and validation cohorts 59
3.3.2.2 ROC curves for RS_{CT}, Definition of optimal RS_{CT} threshold 60
3.3.2.3 RS_{CT}* performance on validation data 62
3.3.3 Exploratory analysis of AHA-segment-specific optimal regional $RS_{CT,AHA}$* 63
3.3.4 Data adequacy 64
3.3.5 Interobserver agreement 66
3.4 Discussions 67
3.4.1 Main Findings 67
3.4.1.1 AHA-segment-specific optimal threshold 67
3.4.2 Data adequacy 68
3.4.3 Limitations 68
3.4.4 Clinical Significance 69
3.4.5 Conclusion 69
3.5 Acknowledgement 69

Chapter 4: Automated Cardiac Volume Assessment and Cardiac Long- and Short-Axis Imaging Plane Prediction from ECG-gated CT Volumes Enabled By Deep Learning 71
4.1 Introduction 71
4.2 Materials and Methods 73
4.2.1 Training population 73
4.2.2 Manual segmentation and volumetric assessment 74
4.2.3 Manual imaging planes and plane vectors 74
4.2.4 Model architecture 75
4.2.5 Model training 75
4.2.6 Model evaluation and statistics 76
4.2.7 Testing population 82
4.2.8 Statistical evaluation 83
4.3 Results 83
4.3.1 Chamber segmentation and assessment of function 84
4.3.2 Quantitative evaluation of DL-predicted imaging plane vectors 84
4.3.3 Intra and inter-reader differences in imaging plane vectors 85
4.3.4 Visual assessment of plane quality 87
4.3.5 Quantitative assessment of slice position via AHA wall assessment 87
4.3.6 Run-time for DL-based approach 89
4.3.7 Assessment of the utility of DL-predicted planes on test cases 90
4.4 Discussions 92
4.4.1 Main Findings 92
4.4.2 Existing approaches 93
4.4.3 Clinical importance 93
4.4.4 Limitations 94
4.4.5 Conclusion 95
4.5 GitHub Repository 95
4.6 Acknowledgement 96
Chapter 5: Detection of Left Ventricular Wall Motion Abnormalities from Volume Rendering of 4DCT Cardiac Angiograms Using Deep Learning 97

5.1 Introduction 97
5.2 Materials and Methods 94
5.2.1 CT data collection 99
5.2.2 Production of volume rendering video of LV blood-pool 99
5.2.3 Classification of wall motion 101
5.2.4 DL framework design 106
5.2.5 Cross-validation and testing 107
5.2.6 Experiment settings 108
5.2.7 Model performance and LVEF 108
5.2.8 Comparison with expert visual assessment 108
5.2.9 Statistical evaluation 109
5.3 Results 110
5.3.1 Model performance – per-video and per-study classification 110
5.3.2 Model performance – re-bin into 6 regional LV views 111
5.3.3 Model performance – compare with expert assessment 112
5.3.4 Data-size reduction 113
5.4 Discussion 115
5.4.1 Main Findings 115
5.4.2 Benefits of our approach 115
5.4.3 Model performance for each LV view 116
5.4.4 Concerns about expert comparison study 117
5.4.5 Limitations 117
5.4.6 Conclusion 118
5.5 GitHub Repository 119
5.6 Acknowledgement 119
Chapter 6: Conclusions and Future Directions 120
6.1 Contributions 120
6.2 Future directions and outlook 124
References 129

LIST OF ABBREVIATIONS

AHA: American Heart Association

AUC: Area Under Curve

CAC: Coronary Artery Calcification

CAD: Coronary Artery Disease

CCTA: Coronary Computed Tomography Angiogram

CH: Heart Chamber

CI: Confidence Interval

CNN: Convolutional Neural Network

CT: Computed Tomography

DL: Deep Learning

ED: End Diastole

EF: Ejection Fraction

ES: End Systole

FCN: Fully Convolutional Network

FFR: Fractional Flow Reserve

FFR_{CT}: FFR measured non-invasively from CT

FWHM: Full Width Half Maximum

GAN: Generative Adversarial Network

GPU: Graphic Processing Unit

HU: Hounsfield Unit

IMVV: Intraluminal Maximum Voxel Value

LAX: Long-Axis

LV: Left Ventricle

MI: Myocardial Infarction

MRI: Magnetic Resonance Imaging

MV: Mitral Valve

NRI: Net Reclassification Improvement

PSF: Point Spread Function

RNN: Recurrent Neural Network

ROC: Receiver Operator Curve

ROI: Region of Interest

RS_{CT}: Regional Shortening derived via 4DCT

SAX: Short-Axis

SQUEEZ: Stretch Quantifier for Endocardial Engraved Zones

SSF: SnapShot Freeze

VR: Volume Rendering

WMA: Wall Motion Abnormality

LIST OF FIGURES

Figure 1.1. AHA 17-segment model 4

Figure 2.1. The 3D printed hold phantom. The phantom is a cylinder of photopolymer resin with 24 cylindrical holes whose programmed diameters range from 0.8mm to 4.0mm. The HU of the resin was ~100 as the background, and the holes were filled with 10% iodixanol mixed with water giving approximately 1000 HU in the 3~4mm holes for 100kVp images 24

Figure 2.2. A vessel stenosis phantom. (A) 3D mesh of a human coronary tree derived from patient CT data. (B) isolation of one lesion from the coronary tree (C) A 3D-printed vessel stenosis phantom having the exact geometry of the 18 lesions. (D) CT 3D rendered image of the vessel stenosis phantom. (E) Distribution of severity and size of the 17 lesions 25

Figure 2.3. Computation of center points and the cross-sectional planes of the vessel. (A) Computation of center points of the vessel by 3-D medial surface thinning algorithm. (B) Computation of cross-sectional plane of the vessel 31

Figure 2.4. An example of the empirical CT number calibration curve obtained from the CT data of the hole phantom 34

Figure 2.5. Comparison of theoretical and empirical CT number calibration curve. (A) is the normalized PSF of the 5th CT acquisition (120kVp, small focal spot, standard reconstruction). (B) shows the comparison of the measured values with predicted values from Equation 2.2 with σ = 0.45mm 35

Figure 2.6. CT number calibration curve. (A) and (B) shows the influence of x-ray tube current energies only exist before the normalization. (C) and (D) show the difference between curves for different focal spot sizes exist both before and after the normalization. (E) and (F) show the effect of reconstruction kernels both before and after the normalization 37

Figure 2.7. Normalized CT number calibration curve of stationary, moving and motion-corrected phantom CT images. CT data was acquired with 120kV, 350mA, 280ms rotation, small spot size, and standard reconstruction kernel. Using Snapshot Freeze (SSF), the observed vessel voxel values in moving vessels essentially returns to the value measured in stationary vessels 40

Figure 2.8. FWHM calibration curve. The measured diameter, D_{FWHM} has a linear relationship (dashed line represents a linear fit, function: D_{FWHM}=0.989×true diameter-0.025, r^2>0.999) with the true diameter for vessels larger than the cutoff diameter 40

Figure 2.9. Estimation of vessel diameter as a function of position through a particular stenosis (ground truth diameters: proximal 4.10mm, lesion 0.90mm, 78.0% stenosis). As shown in the graph, the CT-number-Calibrated diameter estimates are very close to the ground truth for all range of sizes, but FWHM diameter underestimates the percentage stenosis 42

Figure 2.10. Comparison of the CT-number-Calibrated diameter estimates, D_C (open squares) and FWHM estimates, D_{FWHM} (open triangles) with each ground truth diameter, D_{gt} for the smallest diameter in each lesion in the stenosis phantom 43

Figure 3.1. Inclusion and exclusion criteria 52

Figure 3.2. Histogram of the number of segments for peak RS_{CT} intervals for (a) training and (b) validation cohort. A zoomed-in histogram was made for RS_{CT} interval with the highest overlap in class (-0.20 to -0.15). The optimal threshold $RS_{CT}^* = -0.20$ is also shown 61

Figure 3.3. ROC curve of RS_{CT} as a decision classifier in the training cohort. The threshold ranges from -0.6 at the most left to 0 at the most right. AUC = 0.991. The optimal threshold RS_{CT}^* (black dot) was -0.20 leading to sensitivity = 0.95 and specificity = 0.95. SE = sensitivity. SP = specificity 62

Figure 3.4. ROC curves of regional shortening $RS_{CT,AHA}^*$ for each of 16 AHA segment. The entire dataset (n=100) was used here. Black dots represent the individual optimal threshold $RS_{CT,AHA}^*$ for different AHA segments 65

Figure 3.5. Data adequacy. Line with circular dots represent the change of mean value of optimal thresholds and the line with asterisks represent upper and lower boundary of 95% confidence interval (CI) 65

Figure 4.1. DL model training approach and model architecture. (A): Steps in the DL model training pipeline. (B) U-Net architecture with added branch consisting of 4 fully connected layers after the last max-pooling layer in the down-sampling path was used 77

Figure 4.2. Example of images provided to the expert reader for visual assessment. (A) shows how the three LAX planes (red: 2CH, green: 3CH, and blue: 4CH) were displayed. (B) shows the SAX stack. (C) is Annotation of AHA segment visualization 81

Figure 4.3. Close agreement between DL and manual chamber segmentation and function assessment. (A) Dice coefficient for the LV and LA. (B) Dice coefficient for three CT scanners. (C) Dice coefficient for three types of clinical indications (D) Hausdorff distance for LV and LA. (E) Correlation of LV EF derived using manual and deep-learning segmentation 85

Figure 4.4. Comparison of LAX plane location and angulation differences between readers and DL. Plane displacement (A) and orientation (B) differences were shown 86

Figure 4.5. DL agrees with manual slice planning and correctly visualizes corresponding AHA segments. (A): an example to show DL plane images look similar as manual annotation. (B): close agreement between the manual planes (reported in cyan) and DL (yellow) to intersect with the correct AHA segment 89

Figure 4.6. Utility of deep-learning slice planning in evaluation of regional wall motion abnormalities (A) and longitudinal assessment (B) of patients 91

Figure 4.7. Graphical Abstract showing high performance of both segmentation and plane prediction by our DL framework 95

Figure 5.1. Automatic Generation and Quantitative Labeling of Volume Rendering Video. This figure contains two parts: Rendering Generation. automatic generation of VR video (left column, white background, step 1-4 in red) and Data Labeling: quantitative labeling of the video (right column, light grey background, step a-d in blue) 104

Figure 5.2. Deep Learning Framework. This framework with a pre-trained convolutional neural network and a recurrent neural network (trained end-to-end) predicts a binary classification of the presence of WMA in the video 107

Figure 5.3. DL classification accuracy vs. LVEF. The per-video (black) and per-study (grey) accuracy are shown in studies with (LVEF<40%), (40≤LVEF ≤60%) and (LVEF>60%). * indicates the significant difference 112

LIST OF TABLES

Table 1.1. Non-invasive image modalities to evaluate myocardial function 10

Table 2.1. Seven sets of CT parameters used in the CT examinations. Focal spot size = 1.0 x 0.7mm for Small, and 1.6 x 1.2mm for Large, and 2.0 x 2.1mm for Extra Large 27

Table 3.1. Patient Cohort Information 59

Table 3.2. Classification performance of RS_{CT}* in the training and validation cohorts 62

Table 3.3 Classification performance of RS_{CT}* for each AHA segment 64

Table 3.4. Re-Classification in validation cohort by using $RS_{CT,AHA}$* instead of RS_{CT}* 66

Table 4.1. Comparison of LAX Plane Location and Angulation Differences between Readers and Deep Learning 87

Table 4.2. Diagnostic Adequacy of Manual and Deep-Learning Imaging Planes as Scored by Cardiothoracic Imaging Expert 88

Table 4.3. Assessment of AHA Wall Visualization for Manual and DL-based Cardiac Planes. Percentage of cases in which the LAX plane correctly intersects corresponding AHA wall was shown 88

Table 4.4. Diagnostic Adequacy of Deep-Learning Imaging Planes in the Testing Group as Scored by Imaging Experts 90

Table 4.5. The Close Agreement of Classification of EF Between Visual Estimation by Expert Readers and Automated Quantification via DL LV Segmentation. The classification of EF into <40%, 40-50%, and >50% with the DL approach agreed with visual prediction in 88.9% and 80.5% of cases for Reader 2 and 3, respectively 91

Table 5.1. DL Classification Performance in Cross-validation and Testing 113

Table 5.2. DL Classification Performance in CT studies with 40 < LVEF <60%. 47 CT studies with 40%<LVEF<60% were in the cross-validation and 41 CT studies were in the testing 114

Table 5.3. Results re-binned into Six Projection Views. This table shows the per-video classification of our DL model when detecting WMA from each regional view of LV 114

Table 5.4. Comparison between DL and Expert Visual Assessment. Per-study comparison were run on 100 CT studies randomly selected from the testing cohort 115

ACKNOWLEDGEMENT

I would like to thank my parents, Yuan Chen and Weiqun Jiang, most especially. You are the biggest support all the time. Without you, this work would not have been possible. Dad and Mom, I love you all the time.

I would also express my deepest gratitude to my thesis advisors, Dr. Elliot McVeigh and Dr. Francisco Contijoch, for leading me into the research field of medical imaging and for your countless and inspirational mentorship and guidance over the past five years. Without you two, my research work cannot be so rigorous, high-quality, and clinically meaningful. You two taught me how to be a real scientist who can do science that make this world better. I am also grateful that you two always encourages me and gives me much freedom to pursue what I am passionate about, which makes my PhD life very delightful.

I would also like to thank all my thesis committee members, Dr. Albert Hsiao, Dr. Andrew McCulloch, and Dr. Kevin King, for providing me valuable suggestions on my thesis. I would also like to thank all my co-authors, who have made fundamental contributions to my published papers.

Chapter 2, in full, is a reprint of the material as it appears in "Precise Measurement of Coronary Stenosis Diameter with CCTA using CT number calibration", **Zhennong Chen**, Francisco Contijoch, Andrew Schluchter, Leo Grady, Michiel Schaap, Web Stayman, Jed Pack, Elliot McVeigh, 2019. The dissertation author was a primary author of this paper.

Chapter 3, in full, has been submitted for publication of the material as it may appear in "Thresholding of Regional Shortening Measured from 4D Cardiac CT Angiograms Accurately Detects the Presence of LV Wall Motion Abnormalities", **Zhennong Chen**, Francisco Contijoch,

Andrew M. Kahn, Seth Kligerman, Hari Narayan, Ashish Manohar, Elliot McVeigh, 2022. The dissertation author was a primary author of this paper.

Chapter 4, in part, is a reprint of the material as it appears in "Automated Cardiac Volume Assessment and Cardiac Long-and Short-Axis Imaging Plane Prediction from ECG-gated CT Volumes Enabled by Deep Learning", **Zhennong Chen**, Marzia Rigolli, Davis Marc Vigneault, Seth Kligerman, Lewis Hahn, Anna Narezkina, Amanda Craine, Katherine Lowe, Francisco Contijoch, 2021. The dissertation author was a primary author of this paper.

Chapter 5, in part, is a reprint of the material as it appears in "Development of Deep Learning Pipeline for Direct Observation of Wall Motion Abnormality from 4DCT", **Zhennong Chen**, Francisco Contijoch, Elliot McVeigh, 2022. The dissertation author was a primary author of this paper.

Chapter 5, in part, is a reprint of the material as it appears in "Detection of LV Wall Motion Abnormalities from Volume Rendering of 4DCT Cardiac angiograms Using Deep Learning", **Zhennong Chen**, Francisco Contijoch, Gabrielle M. Colvert, Ashish Manohar, Andrew M. Kahn, Hari Narayan, Elliot McVeigh, 2022. The dissertation author was a primary author of this paper.

VITA

2017 BS in Biotechnology at the University of California San Diego

2022 PhD in Bioengineering at the University of California San Diego

PUBLICATIONS

Z. Chen, F. Contijoch, G. Colvert, A. Manohar, A. Kahn, H. Narayan, E. McVeigh, "Detection of Left Ventricular Wall Motion Abnormalities from Volume Rendering of 4DCT Cardiac Angiograms Using Deep Learning", *Frontiers in Cardiovascular Medicine*, 2022, DOI:10.3389/fcvm.2022.919751.

Z. Chen, F. Contijoch, E. McVeigh, "Development of Deep Learning Pipeline for Direction Observation of Wall Motion Abnormality from 4DCT", *Medical Imaging 2022: Biomedical Applications in Molecular, Structural and Functional Imaging*, 2022, DOI: http://doi.org/10.1117/12.2607387

Z. Chen, M. Rigolli, D. M. Vigneault, S. Kligerman, L. Hahn, A. Narezkina, A. Craine, K. Lowe, F. Contijoch, "Automated Cardiac Volume Assessment and Cardiac Long-and Short-Axis Imaging Plane Prediction from ECG-gated CT Volumes Enabled by Deep Learning", *European Heart Journal: Digital Health*, 2021, DOI: https://doi.org/10.1093/ehjdh/ztab033

Z. Chen, F. Contijoch, A. Schluchter, L. Grady, M. Schaap, W. Stayman, J. Pack, E. McVeigh, "Precise Measurement of Coronary Stenosis Diameter with CCTA using CT Number Calibration", *Medical Physics*, 2019, DOI: https://doi.org/10.1002/mp.13862

A. Manohar, G. Colvert, J. Ortuno, **Z. Chen**, J. Yang, B. Colvert, W. Bandettini, M. Chen, M. Ledesma-Carbayo, E. McVeigh, "Regional Left Ventricular Endocardial Strains Estimated from Low-dose 4DCT: Comparison with Cardiac Magnetic Resonance Feature Tracking", 2022, *Medical Physics*, Accepted.

A. Manohar, G. Colvert, J. Yang, **Z. Chen**, M. Ledesma-Carbayo, M. Kronborg, A. Sommer, B. Norgaard, J. Nielsen, E. McVeigh, "Prediction of CRT Response Using a Lead Placement Score Derived from 4DCT", *medRxiv*, 2022, DOI: http://doi.org/10.1101/2022.03.23.22272846

E. McVeigh, A. Pourmorteza, M. Guttman, V. Sandfort, F. Contijoch, S. Budhiraja, **Z. Chen**, D. Bluemke, M. Chen, "Regional Myocardial strain Measurements from 4DCT in Patients with Normal LV Function", *Journal of Cardiovascular Computed Tomography*, 2018, DOI: https://doi.org/10.1016/j.jcct.2018.05.002

F. Contijoch, D. Groves, **Z. Chen**, M. Chen, E. McVeigh, "A Novel Method for Evaluating Regional RV Function in the Adult Congenital Heart with Low-dose CT and SQUEEZ

Processing", *International Journal of Cardiology*, 2017, DOI: https://doi.org/10.1016/j.ijcard.2017.08.040

FIELD OF STUDY

Major Field:

Cardiovascular Imaging, Computed Tomography, Deep Learning

ABSTRACT OF THE DISSERTATION

Analysis of Cardiovascular Disease using Cardiac Computed Tomography and Deep Learning

By

Zhennong Chen

Doctor of Philosophy in Bioengineering

University of California San Diego, 2022

Professor Elliot McVeigh, Chair

Cardiovascular disease is the leading cause of death in the United States. 30~50% of cardiovascular disease is caused by coronary artery disease (CAD). CAD is caused by the development of coronary stenosis (the narrowing of the coronary arteries), which restricts blood supply to the myocardium and causes myocardial ischemia and eventually heart attack. Accurate

quantification of coronary stenosis is crucial to evaluate the severity of CAD and plan appropriate treatments. Further, the accurate detection and quantification of impaired myocardial function also have great prognostic value in patients with CAD. Computed Tomography (CT) was initially focused on evaluating CAD through CT coronary angiography; the recent developments in 4D CT allow the acquisition of full 3D volumes across the entire cardiac cycle and thus enable the assessment of myocardial function. This dissertation introduces novel analytical and deep learning-based techniques to analyze coronary stenosis and myocardial dysfunction from CT. For stenosis, we develop a novel quantification algorithm to overcome the demanding challenge of quantifying small stenosis *below* the image resolution and greatly enhance the accuracy of the estimates of stenosis severity. For myocardial dysfunction, we demonstrate that 3D myocardial regional shortening (RS_{CT}) measured from CT is an outstanding quantitative classifier to detect regional myocardial wall motion abnormality (WMA). However, the clinical utility of regional myocardial function quantifications such as RS_{CT} measurements is limited by the dependence on manual image analysis. To solve this unmet need, we develop a deep learning (DL) framework to automatically and simultaneously accomplish two essential image processing tasks: (1) segmenting heart chambers and (2) reformatting CT volumes into clinically standard planes. Furthermore, regional myocardial function analysis is computationally expensive to perform for each patient, whereas a trained DL model can be easily deployed and can quickly generate results. Thus, we present the *first* DL approach to detect regional WMA from high-resolution 4DCT empowered by unique features available from dynamic volume rendering. Overall, these novel techniques have outstanding promise to replace time-consuming manual work and lead to automatic, fast, and accurate diagnosis of cardiovascular disease.

Chapter 1: Background

1.1 Cardiovascular Disease

Cardiovascular disease is the leading cause of death for men, women, and people of most racial and ethnic groups in the United States, accounting for 1 in every 4 deaths[1]. It also remains the most common cause of death across European Society of Cardiology countries[2]. Of all the cardiovascular disease cases, 30% -50% were caused by coronary artery disease (CAD)[3,4], with five major risk being: high blood pressure, high cholesterol, diabetes, obesity and smoking[5,6]. CAD is caused by the development of the thickening or hardening of the coronary arteries due to the buildup of atherosclerotic plaque made of fats, cholesterol, calcium, and other substances. The plaque buildup leads to coronary stenosis (meaning the narrowing of blood vessels), restricting the blood supply to the heart muscle (myocardium) and causing myocardial ischemia[7]. If a coronary artery becomes completely blocked by the plaque or if the plaque ruptures, it can lead to myocardial infarction (commonly called heart attack) which is an acute medical emergency.

The gold-standard test for assessing the functional significance of CAD is invasive fractional flow reserve (FFR). FFR is calculated as the ratio of mean pressure downstream of a coronary stenosis to the pressure in the aorta under conditions of maximal hyperemia to dilate the coronary microcirculation and increase coronary blood flow. An FFR value of 0.80 or less (i.e., a drop in maximal blood flow of 20% or more caused by stenosis) indicates the stenosis is causal of myocardial ischemia[8] and may need to be treated by revascularization. A multi-center trial shows[9] that FFR-guided revascularization significantly improved the clinical outcome in patients with stable CAD when compared with medical therapy alone; and the same trial shows

that FFR-guided revascularization significantly improved the outcome when compared with coronary angiography-guided revascularization[10].

1.2 Left Ventricle and its Function

The left ventricle (LV) is the chamber of the heart which pumps blood to the body and its function can be impaired by coronary artery disease. Accurate and reproducible morpho-functional assessment of the LV is crucial as LV morphology, volumes, ejection fraction (EF) and regional function are critical parameters used in the diagnosis[11], clinical management, prognostication, and follow-up of numerous cardiovascular diseases[12,13]. The assessment of LV parameters is included in clinical guidelines[11–13] and is used for both inclusion criteria and endpoints in clinical trials[14].

Myocardial ischemia caused by CAD reduces the heart muscle's ability to pump blood. Thus, the LV walls (including an inner endocardium, the "mid-wall" myocardium and an outer epicardium) do *not* contract normally during the heartbeat. LV ejection fraction (EF) is the most used clinical LV parameter to assess the global LV function to pump blood and is defined as the **Equation 1.1**:

$$EF = \frac{(End\ diastolic\ volume) - (End\ systolic\ volume)}{(End\ diastolic\ volume)} \times 100\% \quad (Equation\ 1.1)$$

where end-diastolic volume and end-systolic volume refer to the volume of blood just prior to the heartbeat and at the peak contraction of the heartbeat, respectively. The reduced LVEF (<= 45%) is correlated with an increase in poor cardiovascular outcome in patients with CAD[15,16]. Unfortunately, LVEF has a number of important limitations including geometric assumptions and load dependency[17], and the significant reduction in EF is usually a late consequence of disease. Instead, researchers have started to use myocardial deformation parameters such as

global longitudinal strain (GLS), global circumferential strain (GCS), and global radial strain (GRS), which directly measure the myocardial contractility along different directions during the LV contraction. These parameters serve as superior prognostic predictors in patients with myocardial ischemia than LVEF[18–21].

However, in patients with highly regional dysfunction, or myocardial dyssynchrony (the lack of synchrony of contraction in different ventricles/ different myocardial segments of LV), or patients with heart failure symptoms and preserved EF (LVEF > 50%)[22,23], these global metrics are no longer effective in capturing LV function. Regional assessment of myocardial function is needed to understand the extent of myocardial infarction and to locate the regional abnormality. In fact, the presence of regional LV wall motion abnormality (WMA) is an independent predictor of adverse cardiovascular events in patients with cardiovascular diseases[24,25]; further, it has greater prognostic values after acute myocardial infarction than global metrics[26,27]. A standardized model for the interpretation of regional LV abnormalities is the 17-segment model (see **Figure 1.1**) proposed by the American Heart Association (AHA)[28]. These individual myocardial segments are assigned to different coronary artery territories (LAD, left anterior descending; LCX, left circumflex; RCA, right coronary artery) to indicate which artery has a stenosis. A detailed correspondence of the 17 segments with each coronary artery can be found in these references[29,30]. Wall motion index (WMI) is one qualitative metric to classify the regional LV wall motion into a score of 1 to 4 where 1 means normal, 2 means hypokinesia, 3 means akinesia and 4 means dyskinesia. Further, the measurement of physical parameters of myocardium such as regional myocardial strain can provide a quantitative and more sensitive assessment of the regional LV wall motion.

1.3 Non-invasive Cardiac Imaging: Different Modalities

It's important to detect CAD at an early stage to guide optimal patient management. In section 1.1 the invasive FFR has been introduced as a gold-standard way to detect functionally significant CAD while its drawback is obvious. It is an invasive method requiring diagnostic cardiac catheterization. Therefore, a number of non-invasive imaging techniques have been developed and used extensively. Currently, two non-invasive imaging approaches for the diagnosis of CAD are utilized: (1) anatomical imaging, to visualize the anatomy of the coronary stenosis; and (2) functional imaging, to assess the hemodynamic consequences of a coronary stenosis and to assess the resultant myocardial function. In the following two sub-sections, I introduce the common non-invasive imaging techniques for each of these two approaches.

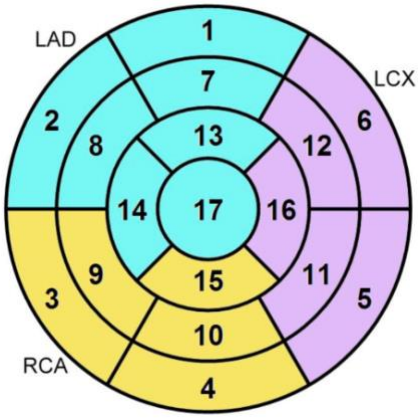

	number	name
Basal Segments	1	basal anterior (A)
	2	basal anteroseptal (AS)
	3	basal inferoseptal (IS)
	4	basal inferior (I)
	5	basal inferolateral (IL)
	6	basal anterolateral (AL)
Mid-cavity Segments	7	mid anterior (A)
	8	mid anteroseptal (AS)
	9	mid inferoseptal (IS)
	10	mid inferior (I)
	11	mid inferolateral (IL)
	12	mid anterolateral (AL)
Apical Segments	13	apical anterior (A)
	14	apical septal (S)
	15	apical inferior (I)
	16	apical lateral (L)
	17	apex

Figure 1.1 AHA 17-segment model.

1.3.1 Anatomical Imaging

The three most developed non-invasive coronary imaging modalities are coronary computed tomography angiography (CCTA), magnetic resonance coronary angiography (MRCA) and positron emission tomography (PET). Here the first two are introduced.

CCTA is a noninvasive 3D imaging test that is used to visualize and identify coronary artery disease. Before CCTA examination, the intravenous iodinated contrast agent at a rate of 5-7mL/sec is injected into the patient. The contrast agent significantly increases the attenuation of the blood and thus makes the coronary vessels bright in the image. CCTA is usually performed on ≥64-detector row computed tomography (CT) scanners. There are two main advantages of CCTA. First, it provides the direct visualization of coronary artery plaque including non-calcified, partially calcified and completely calcified plaques. From CCTA, one can also detect the features of a vulnerable plaque with a high risk of rupture, including the presence of positive remodeling, spotty calcification, low attenuation plaque and/or the "napkin ring" sign[31,32]. Second, CCTA can be used to measure the degree of luminal diameter narrowing (in the other words, percentage of stenosis) resulting from the coronary artery plaque. Based on the percentage, the stenosis can be classified into five grades: no stenosis (0%), minimal (1-24%), mild (25%-49%), moderate (50-69%), severe (70-99%), or occluded (100%)[33]. Since 2016, a more standardized grading and reporting system called CAD-RADS[31] has been implemented in some clinics. CCTA has demonstrated the high diagnostic accuracy of detecting obstructive coronary stenosis at both thresholds of 50% and 70% stenosis. In the well-known prospective multi-center trial ACCURACY (Assessment by Coronary Computed Tomographic Angiography of Individuals Undergoing Invasive Coronary Angiography)[34] with a total of 230 subjects underwent both CCTA and invasive coronary angiography (which served as the clinical ground truth for the presence of a stenosis), CCTA demonstrated sensitivity, specificity, positive and negative predictive values to detect ≥50% or ≥70% stenosis of: 95%, 83%, 64% and 99%, respectively, and 94%, 83%, 48% and 99%, respectively. The 99% negative predictive value makes CCTA an excellent test to rule out CAD.

Subsequently, a series of large randomized clinical trials have been performed to rigorously determine the clinical utility of CCTA. The PROMISE[35] (Prospective Multicenter Imaging Study for Evaluation of Chest Pain, n =10,003) trial shows that there is no difference in the primary composite endpoint after the cardiovascular procedure between the CCTA testing group and the stress testing group in patient with intermediate-risk symptom. The SCOT-HEART[36] (Scottish Computed Tomography of the HEART, n = 4146) trial has reported the use of CCTA in addition to standard care in patients with stable chest pain leads to a significantly lower rate of death or nonfatal myocardial infarction at 5 years than standard care alone. Several trials conducted in the Emergency Department including the CT-STAT[37] (Coronary Computed Tomographic Angiography for Systematic Triage of Acute Chest Pain Patients to Treatment, n = 1370), ROMICAT-II[38] (Rule Out Myocardial Infarction/ischemia Using Computed Assisted Tomography, n = 100) and ACRIN-PA[39] (CT Angiography for Safe Discharge of Patients with Possible Acute Coronary Syndromes, n = 699) have shown that compared with the standard care, CCTA reduces both the time required to establish a diagnosis and the overall length of stay. These trials also show a negative CCTA result in low- to intermediate-risk patient safely excluded CAD.

The main challenges of CCTA examinations include cardiac motion artifacts related to high heart rate or arrhythmia and the high radiation exposure. For motion artifacts, the administration of β-blocker can lower the heart rate before imaging. The motion-correction postprocessing algorithms such as SnapShot-Freeze[40] or ResyncCT[41] can also be used to reduce the motion artifacts after image acquisition. To reduce the radiation exposure, the prospective electro-cardiographic (ECG)-gating (x-ray only turned on during the part of the cardiac cycle) is introduced to reduce the exposure by up to 90%[42,43]. Furthermore, despite the high diagnostic

sensitivity of CCTA, better CCTA techniques are needed to improve the current low specificity (around ~85%[34,44]) by avoiding calling non-obstructive coronary as obstructive stenosis.

MRCA can depict the lumen of the artery without the ionizing radiation. A multi-center study[45] showed that the MRCA has 93% sensitivity and 42% specificity to identify patients with CAD. Due to the limitations in spatial resolution and long-scan times, MRCA remains a topic or research.

1.3.2 Functional Imaging

Stress myocardial perfusion imaging is the most widely used to assess the hemodynamic consequences of CAD. A stress image is obtained at peak exercise stress and a rest image is obtained once the myocardial perfusion demand has returned to baseline. The difference of two images determines the effect of physical stress on the flow of blood through the coronary arteries and the heart muscle. Stress perfusion imaging can be performed with various imaging modalities such as MR, CT, PET or SPECT.

In section 1.2, the prognostic value of the myocardial function and regional LV wall motion abnormality in patient with cardiovascular diseases has been demonstrated. CAD is a regional disorder that may affect some territories of the heart more than others. Thus, several non-invasive imaging techniques have been developed to enable the measurement of regional myocardial function: echocardiography, cardiac magnetic resonance imaging (MRI), and cardiac CT.

Echocardiography is currently the most used in clinics to evaluate myocardial function - it can be performed at the bedside and experienced readers obtain extremely useful information about LV function rapidly. Unfortunately, it is operator dependent and can be limited by poor

acoustic windows[46]. Foreshortening in the long axis[47] and through-plane motion can lead to errors in quantitative measurements. A newer technology called speckle-tracking echocardiography provides new insights in the objective quantitative assessment of global and regional LV and RV function. By tracking the displacement of the speckles during the cardiac cycle, strain and strain rate can be measured. The detailed explanation of this technique can be found in this reference[48]. It has been extensively studied to show its clinical applications in evaluation of CAD[49]. The ongoing development of 3DE (three dimensional) speckle tracking echocardiography includes the ability to track speckles in 3-dimensions and thus enables the measurement of 3D myocardial strains[50].

MRI tagging is considered as the gold standard for accurate myocardial deformation measurements. By altering the longitudinal magnetization of some regions of the samples before imaging, the contrast between these regions and the rest of sample is created, resulting in the dark lines ("tags") on the image. Researchers realized the usefulness of MRI tagging in cardiac imaging since the 90s[51,52]. The deformation of trackable tags is the direct depiction of the regional myocardium deformation and thus is accurate to detect wall motion abnormalities in myocardial ischemia[25,53]. Despite its usefulness, MR tagging has not been used in clinical practice due to the lack of use of cardiac MRI in general, its long scan times (the requirement of several breath holds is not ideal for very sick patients), complicated image analysis , and the contraindications for patients with implanted devices.

As shown in the previous section, CT was initially utilized to evaluate coronary artery stenosis. Recently, the single-heartbeat CT scan enables the assessment of myocardial function by acquiring a series of functional images spanning the full cardiac cycle in just one heartbeat. CT data acquired in one R to R interval (two successive R-waves of the QRS signal on the ECG)

are usually reconstructed into 10 to 20 phases (every 5% ~ 10% R to R interval) to show the deformation of the heart at each cardiac phase of the entire cardiac cycle. We call this type of CT scanning which records multiple images over time as "4DCT". In clinics, myocardial wall motion is usually visualized on movies of 4DCT data reformatted into a set of two-dimensional (2D) long-axis and short-axis planes[28]. Three-dimensional (3D) visualization techniques such as surface rendering or volume rendering[54] can be used to visualize more complex 3D motion of myocardium.

Compared with echocardiography, CT has shown a strong correlation (Pearson $r \geq 0.8$) in measuring global function of left ventricle both in terms of LVEF[55–57] and GLS[58,59]; Nasis et al.[55], Ko et al.[60] have shown the substantial agreement (kappa $k \geq 0.70$) for the visual detection of regional LV wall motion abnormality (WMA). Strong correlation/agreement has also been shown both in global and regional LV function assessment between cardiac CT and MRI[61,62]. Because of its outstanding advantages such as high spatial resolution (see Table 1.1), fast and reproducible image acquisition, and relatively low cost (when compared to MRI), CT has now become increasingly available as an alternative to assess myocardial function in clinics. However, the *quantitative* measurement of regional myocardial function is particularly challenging in CT since it does not have an inherent texture (e.g., tags in MRI or speckles in echocardiography) to track over the cardiac cycle for local function.

So far, the non-invasive image modalities to evaluate myocardial function including echocardiography, MR and CT have been introduced. Their resolution, advantages and limitations are listed in **Table 1.1**. This dissertation focuses on CT. In the next section, the existing techniques to quantify coronary stenosis and myocardial function from CT will be briefly reviewed.

Table 1.1. Non-invasive image modalities to evaluate myocardial function.

	Echocardiography	Cardiac MR	Cardiac CT
spatial resolution	0.8×0.8×1.5mm	1.8×1.8×8mm[63]	0.5×0.5×0.625mm
temporal resolution	10-25msec	25-50msec	85-175msec[64]
advantages	• High temporal solution • Low cost • Wide availability • Performed by cardiologists • Reimbursement is attractive	• Gold standard of strain imaging • Highly accurate • Reproducible	• Reproducible • High spatial resolution • Single heartbeat acquisition • 4DCT acquires full 3D volumes
limitations	• Limited acquisition window • Operator dependent (non-reproducible) • Foreshortening • Quantitative measures are not reproducible	• Long scan time • Several breath holds • Complex image analysis • Contraindicated for patients with metal devices • Only use in research settings • Not available in cardiology departments	• Radiation exposure • No inherent image textures to track the myocardial motion • Not available in cardiology departments • Reimbursement is too inexpensive

1.4 Quantification Techniques

Accurate assessment of the coronary stenosis as well as the myocardial dysfunction from CT imaging is important to minimize the misinterpretation of the disease and to tailor the treatment planning. Qualitative classification by visualization is routinely used in clinics to classify the severity of the coronary stenosis and of the myocardial dysfunction. For example, clinicians visually classify stenosis into mild, moderate, or severe (see section 1.3.1) and classify

myocardial dysfunction into normal, hypokinetic, akinetic, or dyskinetic (see section 1.2). However, the results are subject to interobserver variability due to different experience and behavior of the readers[65]. Instead, quantification of these abnormalities from reproducible image analyses results in more sensitive and objective investigation, especially for the borderline cases (such as the case with borderline LVEF around 50%). Quantification is also the prerequisite of some computer-aided assessments such as computational fluid dynamics[66]. This section will give a brief overview of existing quantification techniques for (1) coronary stenosis and (2) myocardial function.

1.4.1 Coronary Stenosis Quantification

Most commonly, an estimate of vessel luminal diameter is used to quantify the anatomical significance of stenoses. The accurate vessel lumen segmentation is important for the measurement. Most cardiac CT workstations (e.g., Medis® QAngio CT, MeVisLab) perform the luminal diameter measurement either manually (by drawing internally-calibrated ruler on the image) or semi-automatically (by automatically generated lumen contour followed with manual refinement of the contour)[67]. There also exists fully automatic vessel extraction and segmentation algorithms for CCTA, which avoid interobserver variability.

The most straightforward segmentation strategy is thresholding. Coronary vessels with contrast agent in the CCTA images have higher attenuation than the surrounding soft tissues. Dey et al.[68] proposed a thresholding algorithm based on the scan-specific thresholds of different tissues. Renard et al.[69] and Lavi et al.[70] combined region-growing with thresholding, setting a seed point in each segment of the vessel and growing with the threshold set based on the regional attenuation distribution. The morphological properties of the coronary vessel can be utilized in

addition to attenuation. Bouraoui et al.[71] and Lueogo-Oroz et al.[72] utilized the morphological operators to determine the expansion criteria of region growing. The segmentation task can also be done by solving the likelihood of a voxel being the lumen or the background. This likelihood problem of a binary labeling can be formulized by a binary Markov Random Field which is solved using graph cuts[73,74]. Furthermore, Schaap et al. proposed to use Gaussian kernel regression to remove the falsely labeled regions by graph cuts[73]. Another category of segmentation algorithms try to find the optimized contour function to delineate vessel lumen boundary. Wang et al.[75] proposed a model-guided level set algorithm to find the lumen contour function, plus using the convex priors to assures the tubular structure of coronary lumen. Similarly, Lugauer et al.[76] proposed a learning-based level set algorithm using probabilistic boosting trees. A complete review of classical coronary segmentation algorithms can be found in this reference[77]. With the recent success of deep learning-based segmentation[78], it is unclear if any of these current algorithms will be used in the future.

One challenge in these segmentation methods is the presence of calcium. Calcium shows high attenuation in the CCTA and affects the attenuation of surrounding voxels; having the greatest impact on the attenuation-based algorithm. It is also challenging when a small stenosis diameter is below the image resolution[79]. In **Chapter 2**, a new quantification algorithm[80] that significantly enhances the accuracy of the quantification of small stenoses developed by the author will be introduced.

Apart from the anatomical significance of coronary stenoses (measuring diameter narrowing), CCTA has also been used to estimate the FFR (FFR_{CT}) to quantify the functional significance. FFR_{CT} is based on the computational fluid dynamics (CFD)[81,82], simulating the

blood flow in a coronary tree model extracted from CCTA. It has been shown that accurate lumen diameter measurement is the most important factor to ensure the accuracy of FFR_{CT}[66].

1.4.2 Regional Myocardial Strain Quantification

As mentioned in section 1.3.2, the quantification of regional myocardial strain is challenging in CT due to the lack of inherent image texture that can be tracked through the cardiac cycle. One solution to track regional myocardium deformation is through image registration techniques[83,84]. Patches of myocardium at different time frames are registered based on the local pixel information. The motion vector (used to calculate strain) is determined by the motion of corresponding patches at sequential frames. For most existing applications the method is usually applied in 2D CT slices rather than 3D CT volumes, ignoring the velocity components perpendicular to the 2D planes. The performance of this method is also heavily dependent on the manual refinement of 2D contours of the endocardial and epicardial boundaries of the myocardium.

Biomechanical models[85,86] have been used to quantify 3D motion of myocardium. The biomechanical heart model takes the tissue mechanics of myocardium such as linear elasticity, myocardial incompressibility, and myocardial fiber orientation into account. The model is initially registered to the reference time frame and then the deforming forces are estimated for rest time frames.

Recently McVeigh et al.[87] has created a promising surface feature tracking technique called “Stretch Quantifier for Endocardial Engraved Zones” (SQUEEZ) to quantify the 3D regional shortening (RS_{CT}) of myocardium from 4DCT. A 3D model of the endocardium surface is created by LV blood-pool segmentation followed by the extraction of triangular meshes from

the surface to encode the surface features. Thereafter, a 3D non-rigid point registration algorithm[88] is performed to register the mesh at a "template" time frame to a deformed mesh at any other time frame. The RS_{CT} is calculated by the computing the local area changes of corresponding meshes at two time frames. The technical details of RS_{CT} will be elaborated in **Chapter 3**. The accuracy of this technique has been validated in an anthropomorphic LV phantom[89] and with tagged cardiac MRI in canines[90] and with cine MRI in humans[91]. In **Chapter 3**, we will investigate the clinical utility of RS_{CT} to detect LV regional wall motion abnormalities from 4DCT.

1.5 Deep Learning in CT

Recently, deep learning techniques have been widely used in medical imaging research. One main area of the research in this thesis is the application of deep learning techniques in cardiac CT image analysis.

Deep learning (DL) is a subfield of machine learning (ML) that includes a class of algorithms called neural networks. A neural network recognizes underlying relationships in data. It maps the network input to the output by a series of stacked layers performing alternating linear and nonlinear transformations. Deep neural networks are "deep" in terms of its large number of stacked layers, and the development of deep learning techniques has the potential to change CT image analysis and reconstruction substantially.

The most common deep neural network architecture used in medical image analysis is the convolutional neural network (CNN). CNN is a type of DL model for the data that has a grid pattern (e.g., images) and is designed to automatically and adaptively learn the image features from low- to high-level patterns. An overview of CNN techniques and their application in

medical imaging is given by Yamashita et. al. [92]. Another type of neural network used in medical images is the recurrent neural network (RNN). The unique feature of a RNN is that it can store and pass knowledge learned from the previous instance in a sequence to the learning process of the current instance in that sequence. Therefore, RNN successfully decodes the dynamic behavior of the sequence data and is useful to work for image data that involves sequential time series such as echocardiography, cine-MRI and 4DCT. One of the challenges of deep learning in medical imaging, especially cardiac CT, is the lack of labeled data. For example, if we expect to train a DL model to remove the noise from the image, we usually do not have the noise-free (the reference) images from the same patients of the noisy image. The solution is to use unsupervised learning that does not require the labeled data for training. Generative adversarial network (GAN) is the most popular unsupervised DL algorithm. It consists of one network acting as a generator (e.g.., to generate a high-dose noise-free CT image from a low-dose noisy CT image) and the other network acting as a discriminator assessing whether the generated image is realistic. GAN is typically useful for image enhancement (e.g., noise reduction[93], high-resolution images from low-resolution images[94]) or generation (e.g., inter-modality conversion).

DL has changed the way we do CT image reconstruction. Researchers have applied the CNN to automatically output the reconstructed CT image from the raw sinogram as the input[95,96]. CT denoising is also an important field where CNN becomes very useful[97–99]. The more practical use of DL is to remove the "false positive" in the reconstructed image which are those artifacts such as metal artifacts[100–102], limited-angle artifacts[103,104], truncation artifacts[105] and cone-beam CT artifacts[106]. One challenge of DL reconstruction is to minimize the "false negative" which is the missing of features that are tiny but substantially important in clinical diagnosis (e.g., a very severe coronary stenosis with small diameter). The other challenge is that DL as a data-driven

method is highly dependent on the data distribution of the training dataset and is vulnerable to the outliers and adversarial attack (e.g., image noise)[107]. Recent research work on combining DL and iterative reconstruction ensuring data fidelity[108–110] shows promise to overcome these challenges. A thorough review of deep learning for CT image reconstruction can be found in this reference[111].

Deep learning also shines in the evaluation of cardiovascular disease from CT images. The current development of DL in CAD evaluation and myocardial function analysis will be reviewed in the following sections.

1.5.1 Deep Learning in CAD

A survey of machine learning & deep learning for assessment of coronary artery disease in cardiac CT has been published in *Frontiers in Cardiovascular Medicine*[78]. The authors have surveyed the DL methods for localization of coronary artery calcification (CAC), automatic CAC scoring and localization of non-calcified plaque. They also reviewed the DL methods to quantify the anatomical significance (by lumen segmentation and lumen diameter measurement) and functional significance (by DL-based FFR_{CT}) of the stenosis.

Recently, a machine learning-aided software to perform automated analysis of CCTA called Cleerly LABS (Cleerly, New York, New York) has been cleared by FDA[112]. It uses a series of validated CNNs for image quality assessment, coronary segmentation and labeling, lumen wall evaluation, vessel contour determination and plaque characterization. A recent multi-center international study named CLARIFY (CT Evaluation by Artificial Intelligence for Atherosclerosis, Stenosis and Vascular Morphology, n = 232) has been conducted to compare the results of Cleerly LABS with the ground truth of consensus by three L3 readers[113]. It showed that

the ML-based software has accuracy, sensitivity, specificity to detect >70% stenosis as 99.7%, 90.9%, 99.8% respectively and to detect >50% stenosis as 94.8%, 80.0%, 97.0%, respectively. The mean difference in percent maximal stenosis measured by the ML and by readers is -0.8% with 95% confidence interval as -15.3% to 13.8%. It also showed the high degree of agreement between the ML and the readers with kappa coefficient equal to 0.812 per patient and 0.723 per vessel. Discordance was primarily seen for minimal and mild (<25%) diameter stenoses. Further study to compare ML results from CT with the invasive approaches (e.g., intra-vascular ultrasound or optical coherence tomography) is ongoing.

1.5.2 Deep Learning in Myocardial Function Analysis

DL is useful to perform cardiac image segmentation. Cardiac image segmentation is a critical first step in a variety of applications. Specifically in myocardial function analysis, we need to perform the segmentation of the LV chamber, based on which quantitative measures can be obtained. Doing this segmentation in CT images manually is time-consuming and leads to interobserver variability. There have been a number of published DL techniques for heart chamber segmentation in CT. These techniques provide automatic, fast and reproducible chamber segmentations, and they can be categorized based on the type of DL model inputs. First, the CT images can be divided into many small patches of interest [114,115], which are used as inputs for the DL model to label pixels in the patch that belong to cardiac chambers. Second, three orthogonal projections (axial, coronal and sagittal)[116,117] have been used as model inputs and the predicted segmentations in three projections are fused together to make an intact 3D segmentation. Third, a 2D "U-Net"[118] takes one 2D CT slice each time to do the segmentation in a slice-by-slice fashion. Baskaran et al.[119] successfully applied a 2D U-Net to segment four

chamber images in CT in a slice-by-slice fashion with high accuracy (Dice > 0.91). Based on our experience, a 2D approach may miss the segmentation in some slices (especially the apical slices) and the resultant segmentation may not have a smooth boundary for the intersecting planes between chambers such as the mitral valve plane. Fourth, a 3D U-Net may avoid problems of 2D U-Net by taking the entire 3D CT volume as the input and thus have more consistent segmentation results across slices. Unfortunately, 3D approaches significantly increase the memory demands. As a result, input image volumes are typically cropped or downsampled and networks have less features. Some of the current efforts[120,121] using 3D U-Nets combined a localization network for a coarse pre-detection of heart and then applied 3D U-Net to the detected region for the fine segmentation. Recently, a new DL algorithm called "transformers" using self-attention[122] mechanism has been shown to improve the medical image segmentation by modeling long-range dependencies[123,124]. A thorough review of different DL segmentation algorithms can be found in Chen et al[125]. In **Chapter 4**, the dissertation author will propose a 3D U-Net approach that performs the multi-chamber segmentation and cardiac imaging plane prediction simultaneously[126,127].

After the DL segmentation, one can apply those analytical techniques introduced in section 1.4.2 to quantify the regional myocardial function. Researchers also invented end-to-end DL algorithms that can quantify the function directly from the image. The algorithms usually start with a localization network to extract the region of interest of the heart from the image to minimize data size. Ferdian et al.[128] inputs the cropped frames into CNN+RNN (CNN to extract features from each frame, RNN to decode the temporal information) to predict a set of myocardial landmark points for strain calculation in cardiac MRI. Both Zhang et al.[129] and Salte et al.[130] use a DL optimal flow predictor to obtain the motion vector field (MVF) for strain

calculation in cardiac MRI and echocardiography. Morales et al.[131] uses two CNN in parallel for strain in MRI, one to predict the motion vector field and the other to predict the segmentation of the LV used to reposit the strain map according to the 17-segment model[28].

There has not been DL algorithms for 3D myocardial function analysis in cardiac CT due to two unsolved challenges. First, unlike 2D analysis in MRI and echocardiography, 3D function analysis is a much harder task for DL networks to learn. Second, 3D function analysis requires 4DCT data that is too large to fit on current graphic processing units (GPUs). In **Chapter 5**, the dissertation author will tackle these challenges and propose the first DL framework to detect 3D regional LV wall motion abnormality from 4DCT data[132,133].

1.6 Thesis Outline

This thesis is broken into 4 subsequent chapters:

Chapter 2 focuses on quantification of coronary stenoses. We introduce a new quantification algorithm to overcome the measurement challenges in estimating stenosis severity with vessel diameter below the CT image resolution. In this chapter, we first derive a mathematical relationship between the vessel diameter and the vessel intraluminal maximum CT number. We then show this relationship is dependent on the point-spread-function of the CT image. Utilizing this relationship, we propose a new quantification algorithm (called "CT-number-Calibrated Diameter") which maps measured intraluminal maximum CT number to the estimated vessel diameter. We evaluate the quantification accuracy of our algorithm in an anthropomorphic stenosis phantom consisting of coronary stenoses with smallest diameter below the image resolution.

Chapter 3 focuses on regional myocardial function evaluation. We investigate whether myocardial regional shortening (RS_{CT}) computed from 4DCT can serve as an objective decision classifier to detect the presence of local LV wall motion abnormality (WMA). The RS_{CT} is measured via a previously validated surface feature tracking technique. We also define an optimal thresholding of the RS_{CT} classifier and compare its performance with the visual detection performed by cardiovascular imaging experts.

Chapters 4 and 5 focus on how to use deep learning techniques to solve existing challenges in myocardial function analysis from 4DCT. **Chapter 4** focuses on automating the image processing tasks required for function analysis. The author proposes a DL approach to perform multiple chamber segmentations (left ventricle and left atrium) and cardiac imaging plane re-slicing automatically and simultaneously in a shared DL framework. This framework is modified from a 3D U-Net and a special training strategy is designed. The framework is evaluated using a 5-fold cross-validation cohort and a large independent testing cohort. Concretely, we compare the DL predictions with the manual annotations in terms of numerical metrics such as Dice coefficient and LVEF correlation (for segmentations), as well as location and angular orientation errors (for planes). We also provide DL-predicted planes to two imaging experts to score the diagnostic adequacy of these planes.

Chapter 5 introduces the *first* deep learning technique to detect regional LV wall motion abnormality from 4DCT using dynamic volume rendering. We generate dynamic volume renderings of the LV across the entire cardiac cycle (i.e., a video of the function of a volume-rendered LV blood-pool) from six different regional views of the LV. We then design a DL classification framework using a pre-trained CNN and a RNN sequentially to predict the presence or absence of WMA in the regional LV view in each video. Both the per-regional (per-

video) and per-patient detection accuracy of this framework is evaluated using a 5-fold cross-validation cohort and an independent testing cohort.

Chapter 2: Precise Measurement of Coronary Stenosis Diameter with CCTA Using CT Number Calibration

2.1 Introduction

Since the introduction of 64-detector row CT scanners, coronary CT angiography (CCTA) has emerged as a promising non-invasive method for direct visualization of coronary artery disease (CAD)[134,135] and demonstrated an excellent ability to rule out CAD due to its high negative predictive value[136]. However, even with new CCTA technologies accurate quantification of lesion diameter remains challenging because the vessel diameter of severe lesions (>70% stenosis, or < 2mm)[137] often approaches the limit of the scanner resolution. The uncertainty of lesion diameter reduces the specificity of CCTA diagnoses of significant coronary disease[138]. Furthermore, new non-invasive techniques for estimating disease severity such as FFR_{CT}[139] (FFR defined as fractional flow reserve) require highly accurate vessel geometry in order to obtain accurate coronary blood flow simulations[140]. In this study, we introduce a new technique to improve the accuracy of vessel diameter measurements with CCTA called CT-number-Calibrated Diameter (D_C).

We define CT number of a voxel (described in Hounsfield Unit, HU) as the normalized linear attenuation coefficient and "intraluminal maximum voxel value" (abbreviation as IMVV) as the maximum voxel CT number found inside the vessel lumen. Our CT-number-Calibrated Diameter technique is motivated by a simulation study done by Contijoch et al.[141] in which they show that the IMVV does not depend on vessel size for large vessels but decreases rapidly with decreasing vessel diameter for small vessels and small diameter stenoses. This reduction has a straightforward explanation using the point spread function of the imaging system[142,143], and in this study we derive the mathematical function of this reduction. They also demonstrated that

the full width half maximum (FWHM) estimate of the vessel, D_{FWHM}, which is commonly used in vessel segmentation, approximates the true vessel diameter for large vessels, but can significantly overestimate vessel diameter for small vessels.

Based on the two characteristics of small vessel stated above, we have designed a CT-number-Calibrated diameter technique to estimate vessel diameter. The algorithm uses a different process in each of two vessel size domains: (1) for large vessels with IMVV that is independent of the vessel size, the FWHM estimate of vessel diameter is used, and (2) for small vessels with IMVV that is dependent on the vessel size, the algorithm maps the IMVV to vessel diameter directly using a calibration curve measured for each imaging and reconstruction protocol.

2.2 Materials and Methods

2.2.1 Hole phantom

A hole phantom was 3D-printed using a Form 2 stereolithography system with clear photopolymer resin (Formlabs Inc, Somerville, MA) with 24 cylindrical holes in a cylindrical disk of diameter 8.5-cm and height 2.5-cm. The diameter of the cylindrical holes was programmed to span 4.0 mm through 2.2 mm with 0.2-mm intervals, and 2.2 mm through 0.8 mm with 0.1-mm intervals (**Figure 2.1, programmed diameter**). This array of holes captured the range of diameters found in human coronary vessels. We used a benchtop high-resolution imaging system consisting of a cone-beam CT test bench (using a Paxscan 4343CB flat-panel detector and Rad-94 x-ray tube (Varex, Salt Lake City)) and a penalized-likelihood reconstruction algorithm[144] to confirm the correct printed diameter (**Figure 2.1, printed**

diameter, may different from programmed diameter due to the intrinsic offset of 3D printer) of all holes in 3D printed phantoms used in this study.

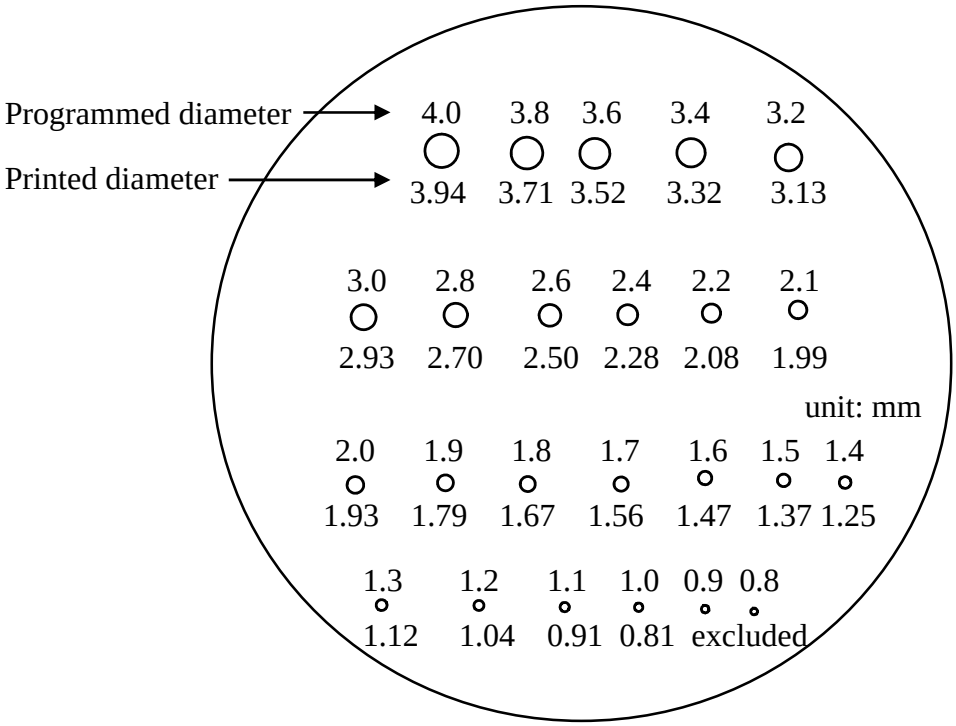

Figure 2.1. The 3D printed hole phantom. The phantom is a cylinder of photopolymer resin with 24 cylindrical holes whose programmed diameters range from 0.8mm to 4.0mm. The correct printed diameter was measured to be slightly smaller than programmed. Holes programmed to be 0.9 and 0.8mm were excluded because their printed size was below the range of sizes where high-resolution imaging system could accurately measure. The HU of the resin was ~100 as the background of CT images, and the holes were filled with 10% iodixanol mixed with water giving a Hounsfield Unit value of approximately 1000 in the 3~4mm holes for 100kVp images.

2.2.2 Patient derived vessel stenosis phantom

Eight high quality 3D meshes of human coronary anatomy were created by automated segmentation of CCTA images with manual correction. Initial automated coronary segmentations were generated using a deep learning technique; these automated segmentations were then visually assessed and edited as necessary. Surface reconstruction was then performed to generate surface meshes from these segmentations. We isolated 18 lesions from the coronary

tree meshes using Blender. The ground truth sizes for the printed coronary vessel stenosis were measured from high-resolution cone-beam CT images mentioned in section 2.2.1. We excluded one lesion from the dataset since it contained a minimum diameter less than 0.8mm. A vessel stenosis phantom was 3D printed with resin to be a 2.5cm high disk with 18 tubular channels that represent the vessel lumen having the exact geometry of the 18 lesions (**Figure 2.2).** About Six lesions for each degree of severity (severe, moderate, and mild) were included as shown in **Figure 2.2E**.

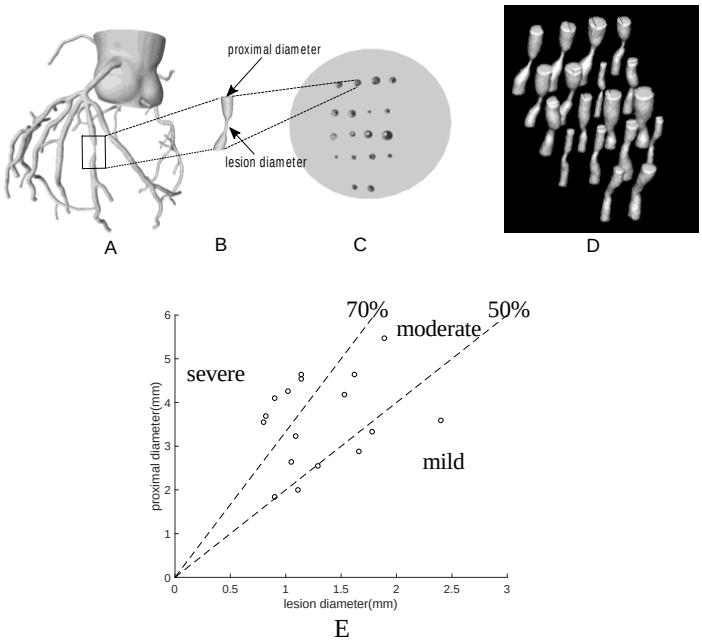

Figure 2.2. A vessel stenosis phantom. (A) 3D mesh of a human coronary tree derived from patient CT data. (B) isolation of one lesion from the coronary tree; the "proximal diameter" and "lesion diameter" are labeled. (C) A 3D-printed vessel stenosis phantom as a disk with 18 tubular channels having the exact geometry of the 18 lesions. The light grey represents the resin in the disk and the holes represent the vessel lumina. (D) CT 3D rendered image of the vessel stenosis phantom. (E) Distribution of severity and size of the 17 lesions shown as the relationship between "proximal diameter" and "lesion diameter" as shown in Fig 2B; there are 6 severe, 6 moderate and 5 mild lesions. The smallest lesion diameter is 0.8mm and the largest diameter is 2.4mm.

2.2.3 CT imaging protocols

The channels in both the 3D printed hole phantom and the vessel stenosis phantom were filled with 10% iodixanol mixed with water to approximate the CT number of a coronary artery. Each phantom was inserted into a sealed plastic bag with additional contrast solution. Two phantoms were placed end to end inside a tissue equivalent Extension Ring (QRM GmBh, Extension Ring L). Two phantoms placed end to end were scanned together on a GE Revolution CT with clinical coronary protocols: common scanner settings included: axial scan, gantry rotation time 280ms, exposure time 162ms, FOV of 20cm, with a 512x512 matrix resulting in an x-y pixel size of 0.391 x 0.391mm, 256 contiguous slices with a slice thickness of 0.625mm. All reconstructions were performed with ASiR-V=50% to reproduce what is used clinically for CCTA at our institution. Seven different CT acquisitions were obtained with the same common settings stated above but different tube energies, tube currents, focal spot sizes and reconstruction kernels (see **Table 2.1)**. To create a high signal-to-noise-ratio (SNR) image for examining the nature of the CT number calibration, 5 equivalent acquisitions were obtained for each set of parameters and the 5 images were averaged to obtain the final image (standard deviation = ~10HU, measured in the resin as the background of the image). For examining the ability of the CT number calibration technique to obtain accurate diameters in the morphological stenosis phantom, single images without averaging were also used (standard deviation ~ 25HU). If not specifically noted, the images mentioned in the study are the averaged images with higher SNR.

2.2.3.1 CT imaging during phantom motion

A motorized platform using a Thorlabs NRT100 stepper motor (Thorlabs, Newton NJ) moved the entire phantom along the horizontal "left-right" axis of the scanner, with a constant velocity of 15mm/s simulating slow coronary vessel motion during diastasis[141,145]. CT data was acquired with 120kV, 350mA, 280ms rotation, small spot size, and standard reconstruction kernel, with ASiR-V = 50%; a single acquisition was used for analysis, no averaging was done. We then implemented a post processing motion-correction algorithm (Snapshot Freeze; GE Healthcare)[146–148] on the motion corrupted images to yield a set of corrected images. Analysis of the IMVV was performed on the corrected and uncorrected images.

Table 2.1. Seven sets of CT parameters used in the CT examinations. Focal spot size = 1.0 x 0.7mm for Small, and 1.6 x 1.2mm for Large, and 2.0 x 2.1mm for Extra Large.

Set No.	Tube energy (kV)	Tube current (mA)	focal spot size (mm)	reconstruction kernel	CTDIvol (mGy)	Marker in the plot
1	100	640	Large(L)	Standard(std)	4.69	□
2	100	640	Large(L)	Bone	4.69	+
3	100	645	Extra Large (XL)	Bone	4.60	*
4	100	420	Small(S)	Bone	3.11	×
5	120	350	Small(S)	Standard(std)	4.12	◇
6	100	420	Small(S)	Standard(std)	3.11	△
7	80	580	Small(S)	Standard(std)	2.11	◁

2.2.4 Creation of calibration curves from the 3D printed hole phantom

2.2.4.1 Measurement of vessel intraluminal maximum voxel value - IMVV

The vessel intraluminal maximum voxel value of each cylindrical hole was measured as the highest CT number of a single voxel within a 4mm × 4mm regional-of-interest (ROI) symmetrically positioned around the center of the hole in a DICOM image processing application (OsiriX).

2.2.4.2 Full Width at Half Maximum Determination, D_{FWHM}

To measure the FWHM diameter of each cylindrical hole, the FWHM region of the hole was identified as the boundary within which all voxel values were greater than 50% of the maximum voxel value in the ROI. The diameter was calculated as the average of the major and minor axis of an ellipse fit to the FWHM boundary contour and yielded the FWHM estimate of the vessel, D_{FWHM}. The IMVV and the D_{FWHM} were calculated for each cylindrical hole in hole phantom at 10 slices separated by 1.25 mm (every other slice in the 3D stack), and mean values were reported to plot calibration curves.

2.2.4.3 Theoretical derivation of CT number calibration curve

The IMVV for each circular hole in the phantom representing circular vessel with true radius *R* (diameter *D = 2R*) is equal to the peak value when a circular vessel with radius *R* is convolved with the two-dimensional (2D) isotropic Gaussian point spread function (PSF). The PSF can be expressed as a normalized Gaussian function in polar coordinates:

$$\mathrm{PSF} = \mathrm{g}(r) = \frac{1}{2\pi\sigma^2} \exp\left(-\frac{r^2}{2\sigma^2}\right) \qquad \text{(Equation 2.1)}$$

where r is the distance of a point to the center of Gaussian, σ is the standard deviation determined by the spatial resolution of the imaging system and $\frac{1}{2\pi\sigma^2}$ is the normalizing constant. The peak value of the convolution of a disk of radius R with the PSF is equal to the volume under the 2D PSF curve within radius R; thus, equal to the polar integral of **Equation 2.1** from r=0 to r=R:

$$\mathrm{IMVV(R)} = Io \int_0^{2\pi} \int_0^R \frac{1}{2\pi\sigma^2} \exp\left(-\frac{r^2}{2\sigma^2}\right) \cdot \mathrm{r} \cdot \mathrm{drd\theta}$$

$$\mathrm{IMVV(R)}/Io = 1 - \exp\left(-\frac{R^2}{2\sigma^2}\right) \qquad \text{(Equation 2.2)}$$

Note that I_o and σ are constants representing the maximum voxel value of a large vessel in the proximal section and the standard deviation of PSF respectively. Comparing **Equation 2.1** and **2.2**, we conclude that the theoretical normalized CT number calibration curve is IMVV(R)/I_o = $1 - k\times$PSF, where k is $2\pi\sigma^2$.

2.2.4.4 Empirical calibration curves

For each set of CT parameters in **Table 2.1**, we generated the empirical CT number calibration curve IMVV(R) (**Figure 2.4, 2.5 and 2.6**) by measuring the corresponding IMVV for each hole size in the hole phantom. We compared the theoretical and empirical curves for the same CT acquisition (**Figure 2.5)** to demonstrate that any CT number calibration curve can be characterized by the standard deviation σ of the 2D Gaussian PSF. The relation between σ and the vessel diameter that has a 50% drop of the constant IMVV of a large vessel in the proximal section, D_{50}, is as follows:

$$0.5 = 1 - \exp\left(-\frac{(D_{50}/2)^2}{2\sigma^2}\right)$$

$$D_{50} = \sqrt{-\ln(0.5) \cdot 8\sigma^2}$$

$$D_{50} = 2.355\,\sigma \qquad \text{(Equation 2.3)}$$

Therefore, for each system and reconstruction we can find the characteristic σ and corresponding PSF by measuring D_{50} in the empirical CT number calibration curve. A more precise method to find σ would be to perform a least square fit of **Equation 2.2** to the empirical curves, but the simplicity of D_{50} gives the user a very simple and robust method that can be performed on graph paper at the scanner.

2.2.5 Segmentation of lesions in the vessel stenosis phantom

The true diameter was measured as a function of position along each vessel perpendicular to a curve connecting segmented center points along the vessel in high-resolution cone-beam CT images. The center points of the vessel were automatically generated in MATLAB by a 3-D medial surface thinning algorithm[149] followed by manual pruning (**Figure 2.3A**). For each vessel lesion that has the length of ~14mm, approximately 35 center points were generated, resulting in the distance between two center points of 0.4mm on average (this was close to the image pixel size). The vessel "direction" at each center point was computed from a smooth line fitted through the point and neighboring center points. **Figure 2.3B** shows that for each center point, we found five proximal and five distal adjacent center points, resulting in an 11-center-point sliding window. A quadratic polynomial exhibiting the centerline's limited curvature[150] was fitted on this window using a least square method. The distance between two center points was thus calculated as the path length of the fitted line between the two.

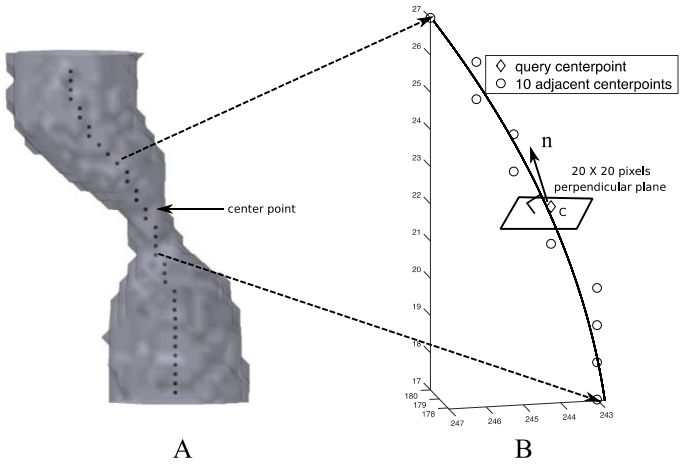

Figure 2.3. Computation of center points and the cross-sectional planes of the vessel. (A) Computation of center points of the vessel by 3-D medial surface thinning algorithm. (B) Computation of cross-sectional plane of the vessel.

Each query center point *c* and its fitted line yielded a normal vector $\vec{n}$. A plane (20×20 pixels) perpendicular to $\vec{n}$ was constructed, with point *c* as its center. This plane was viewed as the cross-sectional plane of the vessel. An upsampling processing by linear interpolation was then applied to the plane to increase the resolution to 200×200, smoothing the voxel value change in the plane.

2.2.6 Estimation of the vessel diameter using the CT-number-Calibrated diameter technique, D_C

In section 2.2.5, we constructed all the cross-sectional planes along the vessel. The IMVV was then measured as the maximum CT number in the cross-sections. The corresponding contrast (= IMVV - background, background≈100HU) was normalized to the averaged contrast in the proximal large vessel region to compensate for different overall signal intensities between acquisitions. In the phantoms these differences were principally caused by different x-ray

contrast for different x-ray tube energy. Based on the normalized contrast, our technique uses one of the two different approaches to measuring the diameter described in detail below.

2.2.6.1 Vessel diameter estimation in larger vessels: FWHM estimate of vessel

For vessels whose IMVV was independent of the vessel size (i.e., vessels with larger diameters), we utilized the FWHM estimate of vessel, D_{FWHM} stated in section 2.2.4.2. Thus, for larger vessels, D_C is equal to D_{FWHM}. This decision was made based on the results shown both in Contijoch et. al. with simulations[141] and **Figure 2.8** with phantom data. For example, the calibration curve with the square sign (1st set of CT parameters) in **Figure 2.8** showed a 3.08mm vessel was measured to be 3.0mm with negligible error.

2.2.6.2 Vessel diameter estimation in smaller vessels: CT number Calibration method

For smaller vessels, the IMVV is influenced by vessel size. We utilized the CT number calibration curve for each set of CT parameters to map the normalized contrast to the vessel diameter for that acquisition. For example, if we use the calibration curve in **Figure 2.4** (1st set of CT parameters), when the contrast is measured as 400HU (IMVV=500HU, ~40% of proximal large vessel amplitude), we understand that it is in the partial volume region and thus can estimate D_C as 1.1mm. It is important to note that the calibration of IMVV vs diameter was provided using an independent phantom which comprises vessel segments of known constant diameter – this should not be confused with a "training" step in a machine learning algorithm.

2.2.7 Comparison of D_{gt}, D_{FWHM} and D_C

We compared the ground truth diameter D_{gt}, FWHM estimate of the vessel D_{FWHM} and CT-number-Calibrated diameter D_C of the same lesion in the stenosis phantom to assess the accuracy of D_C. The D_{gt} was calculated by benchtop high-resolution imaging system. The D_{FWHM} of the lesion was measured by FWHM estimate of vessel. The D_C was calculated by applying our technique stated in section 2.2.6 to the entire lesion. Both D_{FWHM} and D_C were measured in the CT image with the same acquisition setting.

We assessed the accuracy of D_C along the entire lesion by plotting the three estimates of diameter (D_{gt}, D_{FWHM}, D_C) together as a function of distance along the vessel. A Pearson correlation coefficient *r* was computed to quantify the accuracy of the D_C estimate.

2.3 Results

2.3.1 Example CT number calibration curve derived from the hole phantom

The background value of the polymer resin was found to be 100HU±10HU. **Figure 2.4**, as an example of the empirical CT number calibration curve, shows the contrast between the vessel IMVV and the background in Hounsfield Units (ΔHU) plotted against vessel diameter. The IMVV does not depend on vessel size for large vessel diameters but decreases with decreasing vessel diameter for small vessels. In **Figure 2.4**, we define the "cutoff diameter" which divides the calibration curve into two regions: the constant amplitude region above the cutoff diameter and the partial volume region below the cutoff diameter. The cutoff diameter is the diameter value at the intersection of a straight line that fits the reduction of IMVV with decreasing diameter (line fit to points that have an amplitude < 80% of the constant amplitude) with the level of the constant amplitude region; this is shown as a bold black dot.

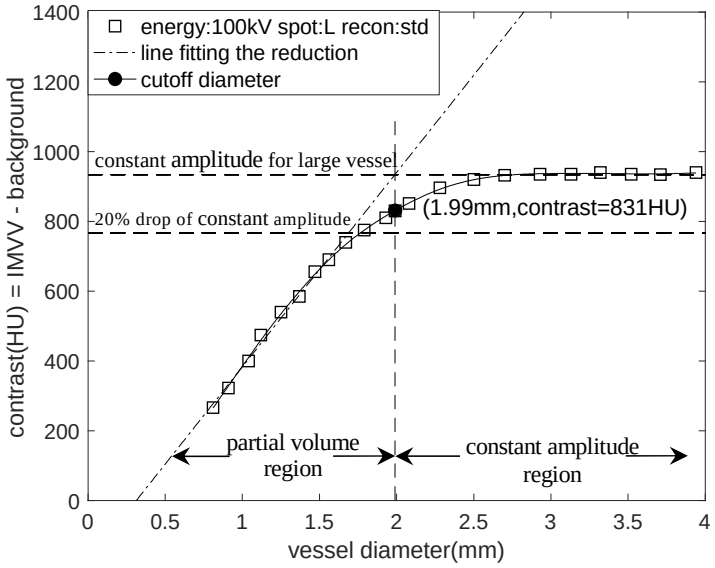

Figure 2.4. An example of the empirical CT number calibration curve obtained from the CT data of the hole phantom. The CT acquisition parameter is the 1st set in Table 2.1.

2.3.2 Comparison of theoretical and empirical CT number calibration curve

For the 5th CT acquisition setting in **Table 2.1**, we measured the corresponding PSF from the image of a Titanium bead with 0.25mm diameter averaged from 8 acquisitions to increase the signal-to-noise ratio. We found the standard deviation of this PSF, $\sigma = 0.45$mm by fitting **Equation 2.1** to the PSF (**Figure 2.5A)**. By plotting **Equation 2.2** with $\sigma = 0.45$mm, we generated the theoretical CT number calibration curve and compared it with the normalized empirical CT number calibration curve of the same acquisition setting (**Figure 2.5B)**. The two curves overlap closely, indicating that we can characterize the calibration curve with a suitable σ and thus find the underlying PSF.

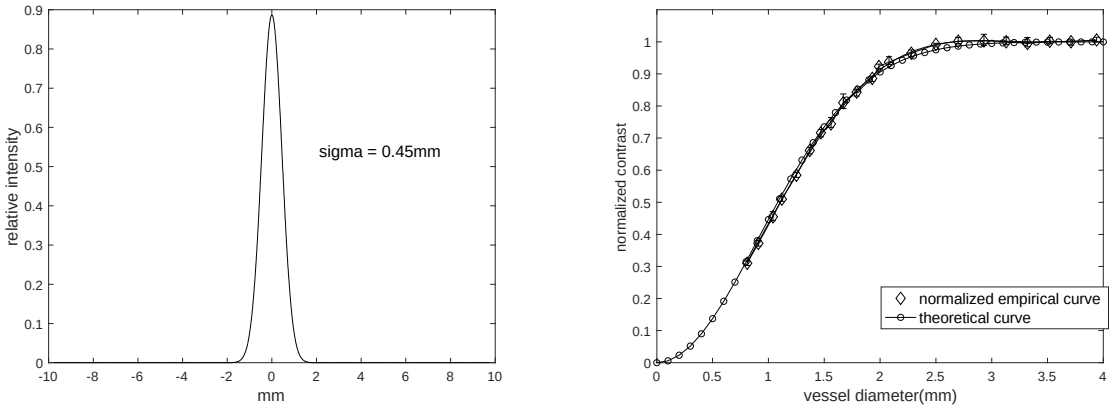

Figure 2.5. Comparison of theoretical and empirical CT number calibration curve. (A) is the normalized PSF of the 5th CT acquisition (120kVp, small focal spot, standard reconstruction). The standard deviation σ is found as 0.45mm. Note: while we only plot it in one dimension, this is actually a two-dimensional isotropic PSF. (B) shows the comparison of the measured values with predicted values from Equation 2.2 with σ = 0.45mm. The error bars from 5 equivalent and repeated scans are shown in the empirical curve to show the robustness.

2.3.3 CT number calibration curve is CT acquisition parameter dependent

Figure 2.6 is a collection of all CT number calibration curves for different image acquisitions and reconstruction parameters. All curves follow the same basic pattern.

Figure 2.6A shows three contrast vs. diameter curves for three different x-ray tube current energies (kVp) with fixed spot size (small) and reconstruction kernel (standard). As expected, the CT number in the constant amplitude region becomes greater with lower kVp. The slope of the ΔHU vs. diameter relationship increases with decreasing tube current energy. The measured cutoff diameter for each curve is approximately equal (~2.0mm). **Figure 2.6B** shows the normalization of the ΔHU values from Figure 6A to the constant amplitude region yields essentially three equivalent calibrations characterized by σ = 0.45mm, indicating that x-ray energy, as expected, has no effect on the normalized calibrations.

Figure 2.6C shows three contrast vs. diameter curves for three different x-ray focal spot sizes with fixed x-ray tube energy (100kVp) and reconstruction kernel (Bone). As expected, for the constant reconstruction kernel a smaller spot size produces a smaller cutoff diameter; after the normalization, the difference between small size and large size still exists in **Figure 2.6D**.

Figure 2.6E shows two contrast vs. diameter curves for two different reconstruction kernels with fixed x-ray tube energy (100kVp) and focal spot size (Large). As expected for constant spot size the "Bone" kernel which passes greater high frequency data through the reconstruction has a significantly smaller cutoff diameter (~1.4mm) than the standard reconstruction kernel (~2mm). The normalized curves in **Figure 2.6F** can be characterized by $\sigma = 0.36$mm and $\sigma = 0.48$mm for "Bone" and "Standard" kernel respectively.

The important message we can derive from the plots in Figure 2.6 is that the CT number calibration curve is CT-acquisition parameter dependent. X-ray energy, x-ray focal spot size and reconstruction kernels all can determine the constant amplitude of large vessels as well as the slope of reduction in calibration curves; however, the effect of x-ray energy no longer exists after the normalization.

Figure 2.6. CT number calibration curve is CT-acquisition-parameter-dependent. All characterized σ were calculated by Equation 2.3 ($D_{50} = 2.355\,\sigma$), where D_{50} is the vessel diameter that has a 50% drop of constant amplitude in the curve. (A) shows the influence of x-ray tube current energies on the raw calibration curves. (B) After normalization to the constant amplitude in large vessels, the three curves essentially become equivalent with a characteristic width of $\sigma = 0.45\text{mm}$. (C) and (D) show the difference between curves for different focal spot sizes exist both before and after the normalization. The calibration of small, large and extra-large focal spot size can be characterized with $\sigma = 0.33$, 0.36, 0.37mm respectively. (E) and (F) show the effect of reconstruction kernels both before and after the normalization. The high-resolution Bone kernel has $\sigma = 0.36\text{mm}$, a cutoff diameter as 1.43mm and cutoff contrast as 88% of the constant amplitude; while the low-resolution standard kernel has $\sigma = 0.48\text{mm}$, a cutoff diameter as 1.99mm and cutoff contrast of 89% of the constant amplitude.

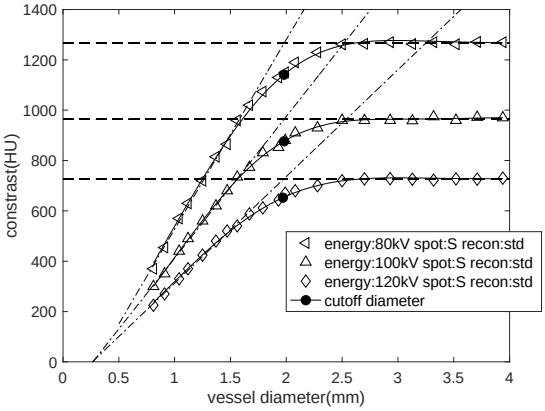
constrast(HU)
vessel diameter(mm)
energy:80kV spot:S recon:std
energy:100kV spot:S recon:std
energy:120kV spot:S recon:std
cutoff diameter

A

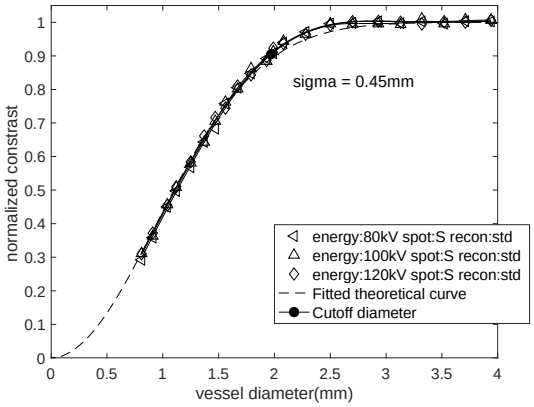
normalized constrast
vessel diameter(mm)
sigma = 0.45mm
energy:80kV spot:S recon:std
energy:100kV spot:S recon:std
energy:120kV spot:S recon:std
Fitted theoretical curve
Cutoff diameter

B

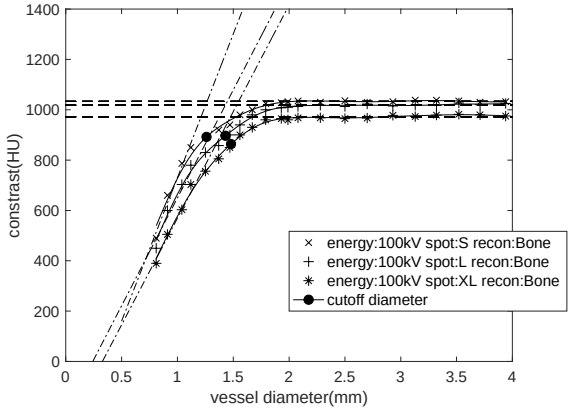
constrast(HU)
vessel diameter(mm)
energy:100kV spot:S recon:Bone
energy:100kV spot:L recon:Bone
energy:100kV spot:XL recon:Bone
cutoff diameter

C

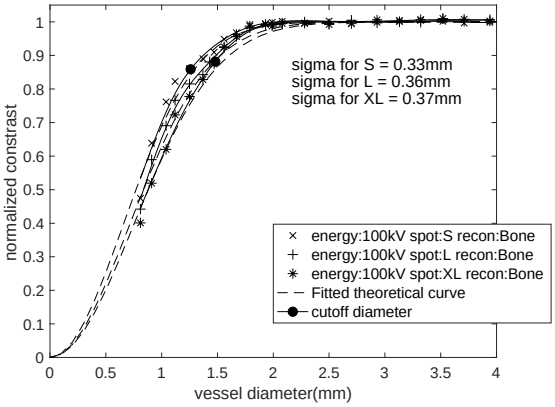
normalized constrast
vessel diameter(mm)
sigma for S = 0.33mm
sigma for L = 0.36mm
sigma for XL = 0.37mm
energy:100kV spot:S recon:Bone
energy:100kV spot:L recon:Bone
energy:100kV spot:XL recon:Bone
Fitted theoretical curve
cutoff diameter

D

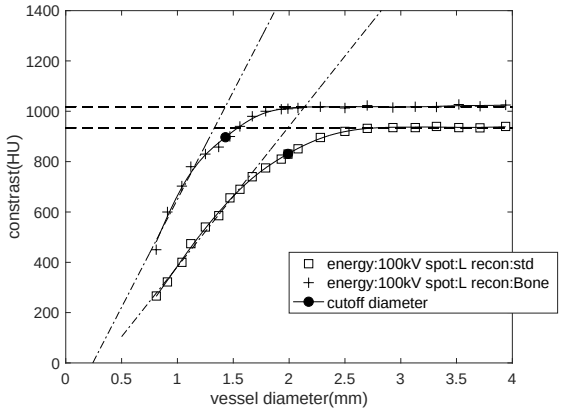
constrast(HU)
vessel diameter(mm)
energy:100kV spot:L recon:std
energy:100kV spot:L recon:Bone
cutoff diameter

E

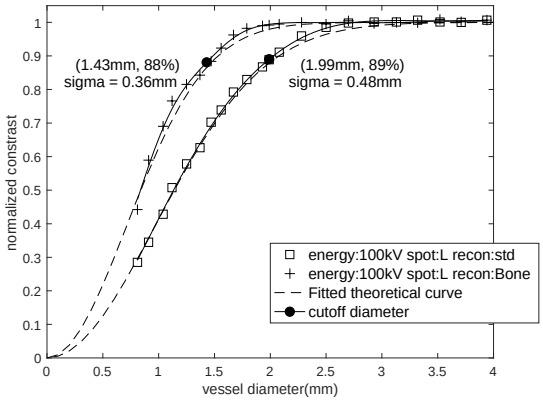
normalized constrast
vessel diameter(mm)
(1.43mm, 88%)
sigma = 0.36mm
(1.99mm, 89%)
sigma = 0.48mm
energy:100kV spot:L recon:std
energy:100kV spot:L recon:Bone
Fitted theoretical curve
cutoff diameter

F

2.3.4 Motion artifacts and motion correction in CT number calibration curve

Figure 2.7 illustrates the loss of vessel IMVV and thus contrast with small vessel motion during acquisition (15mm/s in the "left-right" direction, which gives a total displacement of ~2.7mm over the half-scan acquisition). The small motion causes a significant reduction in voxel values for the smaller vessels as shown previously[141] and can lead to an overestimation of the degree of stenosis because of the increased loss of voxel values. For example, the reduction of IMVV makes a 2mm vessel (corresponding to a mild ~30% stenosis of a 3mm proximal vessel) appear to have the IMVV of a 1.5mm stationary vessel (corresponding to a significant 50% stenosis of a 3mm vessel). It is clear from this data that the voxel values of smaller vessels (< 2.5mm) are more sensitive to motion, which is expected. **Figure 2.7** also demonstrates the observed vessel voxel values in moving vessels returns to the value measured in stationary vessels when a post processing motion-correction algorithm (Snapshot Freeze) is applied to correct the motion corrupted image. This implies that the original calibration curve measured in stationary vessels is valid in motion-corrected vessels for this particular motion correction method.

2.3.5 FWHM calibration curve from hole phantom

Figure 2.8 demonstrates that the reconstruction kernel determines the shape of the FWHM calibration curve since the kernel changes the spatial resolution. The FWHM estimate of the vessel, D_{FWHM} has a linear relationship (D_{FWHM} = true size×0.989-0.025) with the true vessel diameter for those vessels that are larger than the cutoff diameter defined above. Based on the fitted linear relationship, we can state that the FWHM estimate of the vessel can measure the vessel diameter larger than cutoff diameter correctly with negligible error. For vessels smaller

than the cutoff diameter, the D_{FWHM} overestimates the size of the vessel, and the curve approaches an asymptotic value.

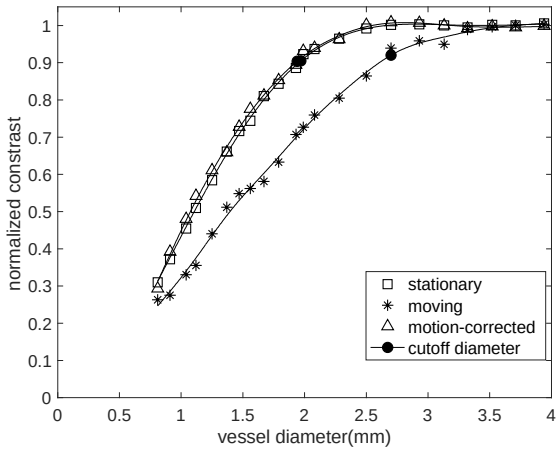

Figure 2.7. Normalized CT number calibration curve of stationary, moving and motion-corrected phantom CT images. CT data was acquired with 5th set of CT parameters from Table 2.1 (120kV, 350mA, 280ms rotation, small spot size, and standard reconstruction kernel). The velocity of vessel was set to be constant (15mm/s). Using Snapshot Freeze (SSF), the observed vessel voxel values in moving vessels essentially returns to the value measured in stationary vessels.

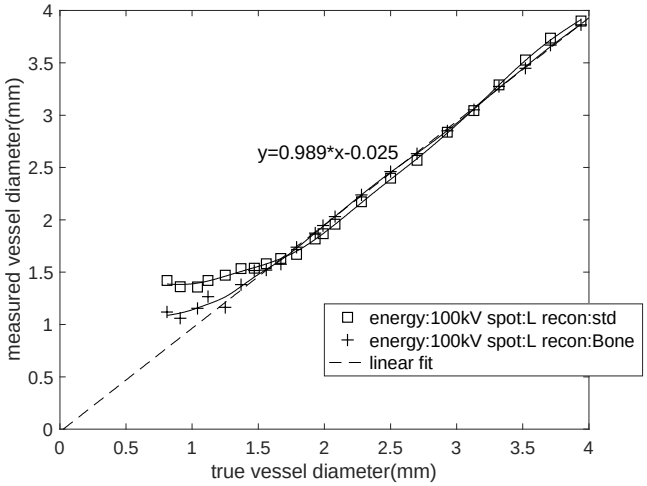

Figure 2.8. FWHM calibration curve. The measured diameter, D_{FWHM} has a linear relationship (dashed line represents a linear fit, function: D_{FWHM}=0.989×true diameter-0.025, r^2>0.999) with the true diameter for vessels larger than the cutoff diameter. When vessel diameter is smaller than cutoff diameter, the D_{FWHM} will gradually approach an asymptotic value, causing an overestimation of lesion size. The shape of the FWHM calibration curve is significantly dependent on the choice of reconstruction kernel and thus spatial resolution.

2.3.6 Estimation of vessel diameter in the vessel stenosis phantom

Figure 2.9 uses the measurement result of one stenosis as an example. The ground truth diameter is measured as proximal 4.10mm, lesion 0.90mm, 78.0% severe stenosis. The acquisition parameter is the 1st set in Table 2.1: 100kVp, 640mA, Large focal spot size, standard reconstruction. It is clear from the result: (1) D_{FWHM} (proximal 4.14 mm, lesion 1.40mm, 66.2% moderate stenosis) yields an overestimation of the smaller caliber diameter in the lesion and thus underestimation of the percentage stenosis. (2) The CT-number-Calibrated diameter D_C (proximal 4.14mm, lesion 0.88mm, 78.7% severe stenosis) accurately estimates the ground truth diameter over the entire range of the vessel segment. We also applied our technique onto 3 sets of single images without averaging of the same stenosis (see section 2.2.3) as shown in **Figure 2.9D.** These results indicate that the high accuracy measurement shown in the averaged image can also be reproduced in single images with higher noise.

In **Figure 2.10** we gathered the measurement results of the smallest diameter in each of 17 lesion models in the stenosis phantom scanned by the 1st set of CT parameters (100kV, 640mA, large focal spot size, standard reconstruction kernel) and computed a Pearson correlation coefficient between D_C and D_{gt} for this set (r=0.998). The D_{FWHM} lies on or nearby the FWHM calibration curve, and the estimates are clearly inaccurate when compared with D_{gt}. This graph also shows a very strong linear correlation between the D_C and the ground truth diameter D_{gt}: $D_C=0.951\times D_{gt}+0.023$, r=0.998. The 95% confidence bounds for the slope and y-intercept are (0.921, 0.981) and (-0.017,0.064) correspondingly. We also computed the average percentage error of the smallest diameter measured by D_C and D_{gt} ($\frac{|Dc-Dgt|}{Dgt}\times 100\%$) over the 17 lesions as 5.06%.

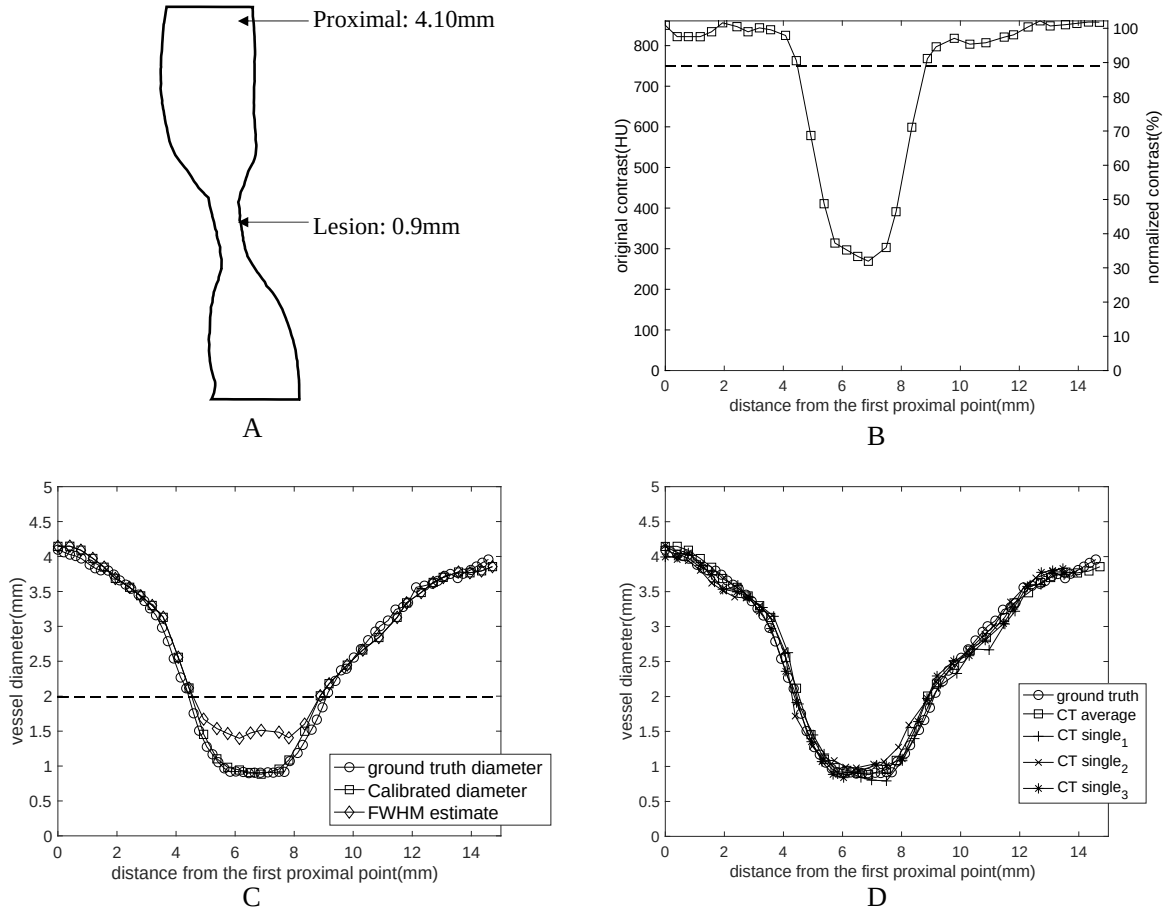

Figure 2.9. Estimation of vessel diameter as a function of position through a particular stenosis (ground truth diameters: proximal 4.10mm, lesion 0.90mm, 78.0% stenosis). The stenosis was imaged with standard clinical imaging parameters: 100kVp, large x-ray focal spot, standard reconstruction kernel. (A) shows the 2D rendering of the structure of the exemplar stenosis. (B) shows both the original contrast ΔHU values and the normalized contrast as a function of position along the vessel. (C) The estimated diameter as a function of position along the vessel. Three diameters are plotted: the ground truth diameter D_{gt}, the diameter estimated with FWHM D_{FWHM}, and the CT-number-Calibrated diameter D_C. The dashed lines in both B and C figures represent the cutoff diameter (1.99mm) and cutoff contrast (89% of maximum) for the standard kernel. As shown in the graph, the CT-number-Calibrated diameter estimates are very close to the ground truth for all range of sizes but FWHM diameter underestimates the percentage stenosis. (D) shows the measurement results when Calibrated diameter technique was applied onto 3 sets of single images without averaging (CT_{single}) of the same stenosis. CT_{single} represents the CT images of one acquisition with higher noise (standard deviation= ~25HU) and $CT_{average}$ represents the averaged CT images with lower noise (standard deviation= ~10HU). It is clear to see that the high measurement accuracy shown in $CT_{average}$ can also be reproduced in CT_{single}.

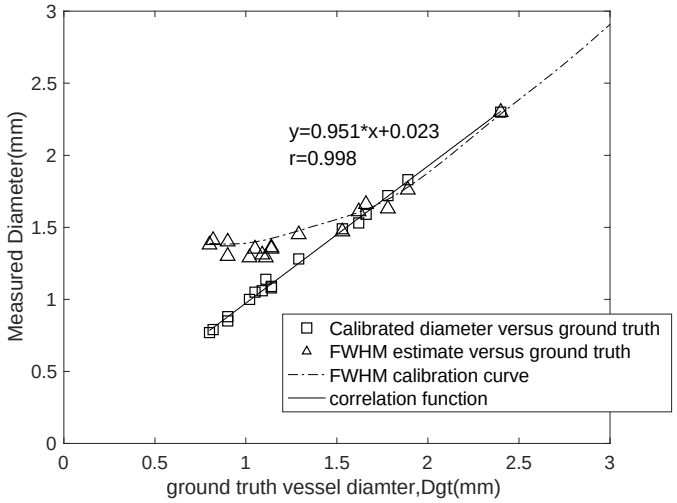

Figure 2.10. Comparison of the CT-number-Calibrated diameter estimates, D_C (open squares) and FWHM estimates, D_{FWHM} (open triangles) with each ground truth diameter, D_{gt} for the smallest diameter in each lesion in the stenosis phantom. The D_{FWHM} lies very close to the FWHM calibration curve for 100kV, 640mA, standard kernel, large focal spot, as expected. There is a very strong linear correlation between D_C and ground truth diameter (D_C=0.951*D_{gt}+0.023, r=0.998) with a slope very close to 1.0 and intercept very close to 0.

2.4 Discussion

2.4.1 Main Findings

In this study, we introduce a new technique to accurately measure the vessel diameter, called CT-number-Calibrated Diameter. It takes advantage of both the FWHM segmentation for vessel segments of "larger" diameter (> cutoff diameter) and the vessel IMVV for vessel segments with "smaller" diameter (<cutoff diameter). Results shown in **Figure 2.9 and 2.10** demonstrate the accuracy of this technique on a particular clinical scanner (GE Revolution CT) with the reconstruction parameters used for clinical CCTA in a range of diameters expected in CCTA images.

2.4.1.1 The Definition of cutoff diameter

We define the "cutoff diameter" as the diameter value at the intersection of a straight line fit to points that have an amplitude < 80% of constant amplitude region with the constant amplitude of large vessels. Note that this 80% was chosen empirically for all CT number calibration curves of different imaging protocols because the straight-line fit was simple and accurate for the points below this amplitude threshold. A possible alternative is to use 4σ as the cutoff diameter once σ is known by measuring D_{50}. If we plug diameter = 4σ in **Equation 2.2**, the cutoff will be ~86% of the constant amplitude of large vessels, which is also a reasonable threshold separating two regions.

2.4.1.2 Calibration curves are CT acquisition parameter dependent

In all cases vessel IMVV vs. diameter was found to have a simple functional form: a constant region above a cutoff diameter, and a decreasing IMVV vs. decreasing diameter below a cutoff diameter. The reason for the reduction is the partial volume effect[151]. Different CT acquisition parameter settings can affect the value of the constant region and the slope of reduction. After the normalization of different curves, the constant region is always equal to 1 and only the slope of reduction varies, which is characterizing the spatial resolution of the system with all of the particular scanning parameters, reconstruction smoothing, and detection task included.

From the mathematical derivation, we state that every calibration curve can be characterized by just one parameter, the σ of the 2D PSF. We also define a "cutoff" diameter to divide the curve into two parts in which different measurement methods are used. It is easy to

deduce that a calibration curve of higher resolution imaging system has a smaller cutoff diameter and can be characterized by smaller σ.

We include three parameters in this study: x-ray tube energy, focal spot size and reconstruction kernel. While different raw IMVV vs diameter curves were obtained at different beam energies, the normalized calibration curves essentially overlap for the three energies tested (80, 100, 120 kVp) shown in **Figure 2.6B**. As shown in **Figure 2.6C and 2.6D**, larger focal spot size causes greater blurring, and the cutoff diameter is larger for larger focal spot size; however, the slope of reduction is smaller for larger focal spot size. Interestingly, the extra-large focal spot size in **Figure 2.6C** shows a lower constant amplitude for large vessels compared with the small and large focal spot sizes. This is likely due to the interaction of the point spread function from different focal spots with the shape of the vessels giving higher "peaks" in the vessels imaged with the small and large focal spot sizes. The reconstruction kernels with higher spatial resolution have smaller cutoff diameters and smaller characteristic σ as shown in **Figure 2.6F**.

It is clear that calibration curves are CT-parameter-dependent. This implies that individual calibration curves for the set of possible CCTA imaging parameters should be obtained for each imaging system. While somewhat cumbersome, the calibration curves should only need to be obtained once for each set of parameters on each system. Importantly, we show the mathematical relation between calibration curves and 2D isotropic PSF, which suggests that if we empirically measure one, we can analytically derive the other.

2.4.1.3 CT-number-Calibrated diameter in moving objects

The motion sensitivity measurements performed in this study using the anthropomorphic phantom recapitulate the same result shown by Contijoch et. al. with simulations[141]. The small

"drift" motion causes a significant reduction in voxel values for the smaller vessels and can lead to an overestimation of the degree of stenosis because the motion causes an increased loss of voxel values. The stenosis in larger vessels, however, might be underestimated due to motion[152] resulting in a blurring of the edges of the vessel and conservation of the voxel values in the central voxels of the vessels.

In this study we used Snapshot Freeze (SSF), a newly developed motion-correction algorithm, which has been shown to improve the image quality of moving objects by Fuchs[153] and Li[154]. It is clear in **Figure 2.7** that the voxel value in the moving vessel is increased by SSF to the value measured in the same vessel when the vessel is stationary; after motion correction we can therefore apply the CT-number-calibrated diameter technique.

2.4.2 Accuracy of vessel diameter measurement is important for FFR_{CT} of stenoses

Recently, FFR_{CT} has emerged as a non-invasive method to assess lesion significance in CCTA. FFR_{CT} uses computational fluid dynamics to evaluate coronary blood flow[139] and FFR_{CT} used with CT among stable patients with suspected or known CAD lead to improved diagnostic accuracy and discrimination vs CT alone[155]. Sankaran et. al. [140] demonstrated that the effect of uncertainty in lumen diameter exceeds that of the other model variables in determining the accuracy of FFR_{CT}. Hence, the CT-number-calibrated diameter, which accurately measures the vessel diameters in a range of values important for CCTA will have a positive impact on the accuracy of FFR_{CT}.

2.4.3 Limitations

This study only measured and validated the CT number calibration curves on a single imaging system (GE Revolution CT) and a finite number of protocols used for CCTA in our institution. Further work is needed to generalize the technique to other systems and other reconstruction algorithms. Also, there are a number of papers that address the question of diameter estimation using various techniques[150],[156]; while we did not compare CT-number-Calibrated Diameters against these methods, the absolute precision and accuracy of the technique is fully reported here and stands on its own.

The phantom which comprised 17 coronary artery stenoses did not simulate the effect of coronary artery calcium in any of the lesions. A new phantom will need to be designed to include a realistic representation of calcified coronary arteries, which is a common condition. The background CT number in the phantom used is around 100HU, which is similar to soft tissue, but unlike fat attenuation normally found around epicardial coronary arteries; however, we believe the results reported here would scale to different uniform background values. Further study would be needed to fully characterize the effect of non-uniform background such as the co-existence of fat and muscle around arteries.

The CT number calibration measurement requires the normalization of IMVV to the proximal amplitude in the constant zone; it is assumed that the contrast agent concentration in the blood is constant along the vessel. We assumed that the images were obtained at a phase of the injection that produced a relatively low gradient in contrast from the proximal vessel to the center of the lesion[157]. A modified algorithm could use an expected amplitude that is linear interpolation of the proximal and distal vessels; however, a drop in the flow distal to the lesion may also affect this value. Normalization to the proximal amplitude seemed to be the simplest

choice and is easily measured by an observer. The CT number calibration also assumes the disk shape of vessel and we designed our vessel stenosis phantom to have vessels with all convex cross sections. However, we understand that patient stenoses could have the non-convex shapes, and **Equation 2.2** approximates these other more complex shapes. Classifying these more complex shapes with a simple "percent stenosis" becomes challenging as the flow modeling also becomes more complex.

The CT number calibration measurement relies on the CT number of a single voxel in the coronary artery, which is a weakness. However, by definition, it is difficult to derive a technique that uses an "average" CT number inside the vessel lumen, because for significant stenoses the target vessel has a diameter that is at the limits of the resolution of the system. Hence, the simplest and most reproducible measurement was intraluminal maximum voxel value (IMVV); this measurement has a correlation with neighboring voxels that are driven by the blur of the point spread function, and has a very simple analytical behavior as shown in **Equation 2.2**. This work builds on the original simulations of Contijoch et. al.[141] by adding actual measurements using modern coronary imaging protocols; however, moving the technique into humans will likely require validation studies involving independent measurements of the coronary diameter such as OCT, intravascular US, or QCA from biplane fluoroscopy. Unfortunately, all of these other techniques suffer from their own limitations.

2.4.4 Conclusion

CT-number-Calibrated Diameter is an effective method to enhance the accuracy of the estimate of small vessel diameters and degree of coronary stenosis in CCTA.

2.5 Acknowledgement

Chapter 2, in full, is a reprint of the material as it appears in “Precise Measurement of Coronary Stenosis Diameter with CCTA using CT number calibration”, Zhennong Chen, Francisco Contijoch, Andrew Schluchter, Leo Grady, Michiel Schaap, Web Stayman, Jed Pack, Elliot McVeigh, 2019. The dissertation author was a primary author of this paper.

Chapter 3: Thresholding of Regional Shortening Measured from 4D Cardiac CT Angiograms Accurately Detects the Presence of LV Wall Motion Abnormalities

3.1 Introduction

As stated in section 1.2, the presence of left ventricular (LV) wall motion abnormalities (WMA) has been demonstrated to be an independent predictor of adverse cardiovascular events in patients with cardiovascular diseases such as myocardial infarction(MI)[24,158], dyssynchrony[159,160] and congenital heart disease[161,162]. Further, *regional* WMA have greater prognostic value after acute MI than global metrics such as LV ejection fraction (EF)[26,27]. An overview of different imaging modalities to analyze LV wall motion can be found in section 1.3.2. Briefly, most clinical cardiac wall motion analysis is performed using echocardiography, which is operator dependent, can be limited by poor acoustic windows and has been shown to be poorly reproducible[46]. Cardiac magnetic resonance (CMR) is considered the reference standard, but it is expensive and may be contraindicated. Multidetector cardiac computed tomography (CT) has been repeatedly shown in large clinical trials to be an effective non-invasive imaging modality to evaluate suspected coronary arteries[35,36,80]. Recently, the single-heartbeat CT scan enables the assessment of cardiac wall motion by acquiring a series of functional images spanning the full cardiac cycle in just one heartbeat[163,164]. It has also been shown that regional WMA detection via CT agrees with echocardiography[56] as well as CMR[62].

Recently, a new surface feature tracking technique, called "Stretch Quantifier for Endocardial Engraved Zones" (SQUEEZ)[87], has been developed to quantify the 3D myocardial regional shortening (RS_{CT}) from 4DCT acquired with routine clinical protocols. This technique derives the deformation and displacement of endocardial surface point patches via nonrigid 3D point set registration[88] and thus obtains the RS_{CT} of the endocardium. Section 3.2.3 will

introduce the technical details of SQUEEZ. The accuracy of RS_{CT} has been validated in the anthropomorphic LV phantom[89] with known ground truth and has been compared with the circumferential shortening measured by tagged CMR in canines[90]. Recently, RS_{CT} has been used to derive the baseline RS_{CT} values in the normal human LV[164], to quantify regional LV function in patients before and after transcatheter mitral valve implantation[165], to identify regional RV systolic dysfunction in patients with Tetralogy of Fallot[166], and to predict the response of cardiac resynchronization therapy[167].

The overarching goals of this research are first to investigate the effectiveness of RS_{CT} as a decision classifier to detect the presence of LV WMA from 4DCT studies and second to derive an optimal threshold of RS_{CT} that achieves accurate and reproducible detection performance. preliminary study[168] has been presented at the annual scientific meeting of Society of Cardiovascular Computed Tomography in 2021.

3.2 Materials and Methods

3.2.1 CT data collection

This study was approved by the institutional review board with waiver of informed consent. 505 ECG-gated contrast enhanced cardiac CT studies that had: (1) the full R-wave to R-wave (RR) coverage and (2) had an imaging report including the explicit demonstration of cardiac function as normal or abnormal (either globally or regionally) between Apr 2018 and Dec 2020 were retrospectively collected within a single institution. Note that the imaging reports were used *only* to pre-screen the studies in order to maintain the class balance between patients with normal function versus with abnormal function in the study cohort. 163 studies were then excluded due to the exclusion criteria, and the purpose of class balancing (see **Figure 3.1** for

details). Due to the extensive labor required to manually score the per-segment wall motion in a large cohort, we further reduced our study population by randomly selecting 100 studies from the remaining 342 studies while ensuring these 100 studies were from unique patients.

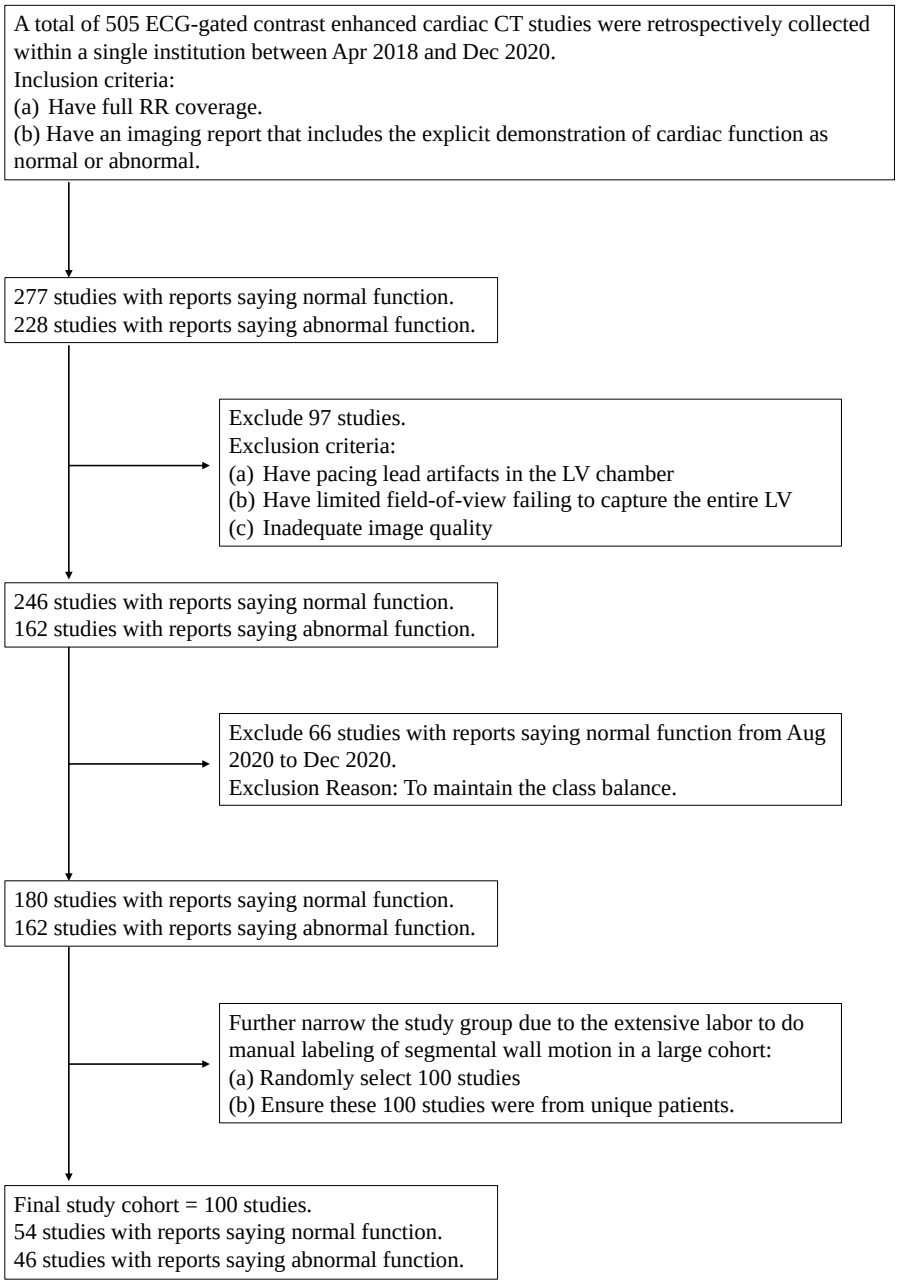

Figure 3.1. Inclusion and Exclusion Criteria.

All CT studies were acquired by a single, wide detector CT scanner with 256 detector rows (Revolution scanner, GE Healthcare, Chicago IL) allowing for a single heartbeat axial 16cm acquisition across the cardiac cycle. All studies have functional images reconstructed every 10% RR internal using the vendor default cardiac function image reconstruction method. Images were reconstructed on a 512×512 pixel matrix in the axial plane over a field of view of 24 +-2 cm with 0.625 mm slice thickness.

3.2.2 Segmental Wall Motion Abnormality Visual Labels

The wall motion classification in each segment was made via visual labeling by three imaging experts after retrospective blinded review of the cases (not via the imaging reports). For this review every study was reformatted into a set of cardiac imaging planes including three long-axis views and a short-axis stack (9 short-axis planes evenly spaced from the mitral valve plane to the LV apex). After these 12 planes were re-formatted, cine movies of these planes were made to show the cardiac function across the cardiac cycle. Three cardiovascular imaging experts (Expert 1: author A.K, >15 years of experience; Expert 2: author S.K, >14 years; and Expert 3: author H.N, >5 years) independently scored the wall motion for each segment (segment 1 through 16 in the AHA 17-segment model[28], see **Figure 1.1**) by visual inspection of wall motion. The scores were: 0 for normal motion, 1 for hypokinetic, 2 for akinetic and 3 for dyskinetic. Scores 1-3 were further grouped as abnormal wall motion and score 0 was normal motion. The evaluations from three experts were combined into a single visual label of WMA for each segment based on majority voting (e.g., if two “abnormal” and one “normal”, the final label is “abnormal”).

In this chapter 3 we used the term "segment" to refer to a single LV myocardial segment in one CT study (e.g., 10 CT studies will have 160 segments); we used the phrase "AHA segment" to denote a particular AHA segment (e.g., the detection accuracy found in the basal anterior AHA segment).

3.2.3 Quantitative Image Analysis – Pipeline of RS_{CT} Measurement

3.2.3.1 Image Processing

Several image processing steps were done. First, the voxel-wise LV blood-pool segmentation was done in ITK-SNAP (Philadelphia, PA, USA)[169] using the active contour regional growing module. Two planes delineating the mitral valve and the left ventricular outflow tract (LVOT) were defined as previously described[165]. The full LV endocardium was defined from the mitral valve plane to the endocardial apical tip. Second, the CT image volume was rotated to align the LV long axis with the *z* axis of the image. Third, the image was resampled to $2mm^3$ isotropic voxel resolution according to the published RS_{CT} analyses[90,164–166]. The details in image processing can be found in this reference[165].

3.2.3.2 Image Analysis

After image processing, a temporal sequence of the binary LV volumes across the entire cardiac cycle was sent to SQUEEZ pipeline[87] for automatic quantitative analysis. Concretely, triangular meshes of the endocardial surface were extracted by *isosurface* in MATLAB (MathWorks Inc., Natick, MA). Then, a 3D non-rigid point set registration[88] with tuned parameters[89] was performed to register every endocardial mesh at template time frame (here, defined as end-diastole, ED) to the meshes created for other time frames. Technical details of

"RS_{CT}" can be found in this reference[87]. Regional shortening (RS_{CT}) at a systolic time frame *t* was calculated at each triangular mesh on the endocardial mesh by the **Equation 3.1**:

$$RS_{CT} = \sqrt{\frac{Area_t}{Area_{ED}}} - 1 \qquad \text{(Equation 3.1)}$$

where $Area_t$ is the area of an endocardial mesh at time frame *t* and $Area_{ED}$ is the area of the same mesh at ED. RS_{CT} for an endocardial surface voxel was calculated as the average RS_{CT} value of a patch of meshes directly connected with this voxel.

We computed a segmental RS_{CT} as the average RS_{CT} for all the voxels that belong to each segment. We defined a segmental "peak RS_{CT}" as the maximum absolute value of segmental RS_{CT} across all time frames. Note that the peak RS_{CT} is not the RS_{CT} at the end-systole but refers to the segmental maximum strain in the cardiac contraction.

3.2.4 Data Split

We randomly and evenly split the dataset (n=100) into a training cohort (n=50) and a validation cohort (n=50). The training cohort was used to answer two questions: (1) can the peak RS_{CT} used as a quantitative decision classifier to detect segmental WMA? (2) what is the optimal threshold of peak RS_{CT} that can maximize the summation of sensitivity and specificity? The validation cohort was used to answer one question: (1) can the optimal threshold achieve the same high detection performance in an independent new cohort?

3.2.5 RS_{CT} Optimal Threshold

50 CT studies, each with 16 segments, led to 800 segments in the training cohort. A segment was defined as abnormal or normal by the selected threshold value of the peak RS_{CT}:

$$segmental\ motion = \begin{cases} abnormal\ , if\ its\ peak\ RS_{CT}\ \geq\ threshold \\ normal\ , if\ its\ peak\ RS_{CT}\ <\ threshold \end{cases} \quad \text{(Equation 3.2)}$$

since RS_{CT} always had a negative value, RS_{CT} larger than a threshold indicated a smaller strain.

In the main study, these 800 segments were used to construct a ROC curve showing the corresponding sensitivity and specificity of peak RS_{CT} as a decision classifier at different classification thresholds when compared to expert visual evaluation. The area-under-curve (AUC) was calculated. From the ROC curve, the optimal threshold of peak $RS_{CT,}$ noted as RS_{CT}*, was defined as the threshold value that maximized the summation of sensitivity and specificity. Here RS_{CT}* is a single threshold that we propose to apply to all 16 AHA segments. In the validation cohort, we applied the RS_{CT}* threshold to the 800 segments in 50 CT studies not used for training and evaluated its detection performance.

Given prior studies on MRI[170] and SPECT[171] that have shown heterogeneity of myocardial wall motion between different AHA segments, we performed an exploratory analysis to define an individual optimal threshold for each of the 16 AHA segments. We use the notation $RS_{CT,AHA}$* to represent these AHA-segment-specific optimal thresholds that maximized the sum of sensitivity and specificity of detecting WMA in that AHA segment. To maximize the amount of data for each AHA segment, we used the entire dataset (N = 100) for each segment.

3.2.6 Data Adequacy

One important question to answer is whether the number of CT studies as well as the class ratio in the training cohort is adequate to derive RS_{CT}* values that generalize to the patient population. Insufficient studies or a large class imbalance in the training data will lead to a highly biased threshold. On the other hand, the marginal impact of collecting additional studies on the threshold and performance of RS_{CT} is unknown.

The adequacy of our training cohort (50 CT studies, 800 segments) was evaluated by the variability of the optimal threshold picked using random subsampling of the dataset. Intuitively, if one has very few studies (e.g., n =5), a random subsampling (e.g., using 4 randomly picked studies to obtain a threshold) will lead to very different RS_{CT}*. However, as the dataset increases, the variability will decrease, implying that the current dataset adequately represents the patient population. We evaluated the variability of RS_{CT}* by simulating the random sampling of 80% of the training dataset for dataset sizes of: n = 10, 20, 30, 40 and 50 studies (160, 320, 480, 640, and 800 segments, respectively).

The generalizability of the RS_{CT}* obtained by the training cohort can also be shown by the similar performance in the independent validation cohort (50 independent studies, 800 segments).

3.2.7 Interobserver Agreement

We calculated the interobserver agreement of classifying a segmental wall motion into normal or abnormal between three experts using Fleiss's Kappa[172] (the Kappa used when there are more than two raters). We also calculated the interobserver agreement of further classifying abnormal segments into hypokinetic (score 1), akinetic (score 2) and dyskinetic (score 3).

3.2.8 Statistical Evaluation

The AUC was reported to evaluate performance of RS_{CT} as a decision classifier. Two-tailed categorical z-test was used to compare data proportions in the training and validation cohorts. Statistical significance was set at $P \leq 0.05$. The accuracy, sensitivity, specificity, true positive rate and Cohen's Kappa value of the RS_{CT}* to detect segmental WMA when compared

with the expert visual labels were reported for both cohorts. We also evaluated the performance of RS_{CT}* on each of 16 AHA segments.

We also defined AHA-segment-specific optimal thresholds $RS_{CT,AHA}$*. To investigate whether using $RS_{CT,AHA}$* improves the detection performance, we calculated the net re-classification improvement (NRI)[173] by using $RS_{CT,AHA}$* instead of RS_{CT}* on the validation cohort. A segment labeled as abnormal by experts was considered an "event", and a segment labeled as normal by experts was considered a "nonevent" such that the NRI could be calculated as:

$$NRI = \frac{N_{event,correctly-reclassify} - N_{event,incorrectly-reclassify}}{total\ number\ of\ events} + \frac{N_{nonevent,correctly-reclassify} - N_{nonevent,incorrectly-reclassify}}{total\ number\ of\ nonevents} \quad (Equation\ 3.3)$$

The NRI was calculated for each AHA segment and across the entire validation cohort.

3.3 Results

3.3.1 Data Info

The entire dataset had 100 CT studies. The mean age was 59 $\pm$14 and the male percentage was 61%. The LV blood-pool had a median intensity of 530 HU (IQR: 435 to 663). The median LV EF by CT was 62.4% (IQR: 45.4 to 69.4). 22 studies with EF $\leq$ 40%, 11 with EF between 41 to 49% and 67 studies with EF above 50%. From these 100 studies a set of 1600 segments were extracted with 432 (27%) segments labeled as "abnormal" by experts. 54 studies were globally normal (meaning all segments were labeled as normal), 12 studies were globally

abnormal (meaning all segments were labeled as abnormal), and the remaining 34 studies were regionally abnormal (meaning some of 16 segments were abnormal).

The information of the training cohort and validation cohort can be found in **Table 3.1**. The number of abnormal segments that belongs to each of 16 AHA segments is in **Table 3.3**. Two-tailed categorical z-test showed that there were no significant differences (all $P > 0.05$) in data proportions between two cohorts in terms of the percentage of sex and abnormal segments.

Table 3.1: Patient Cohort Information. N means the number of CT studies; n means the number of segments.

		Entire Dataset	Training Cohort	Validation Cohort
Cohort Size		N = 100	N = 50	N = 50
Age		59 ± 14	59 ± 15	59 ± 13
Male %		61%	58%	64%
LVEF	median	62.4%	62.1%	63.8%
	<=40%	N = 22	N = 12	N = 10
	41-49%	N = 11	N = 4	N = 7
	>=50%	N = 67	N = 34	N = 33
abnormal segments		n = 432 (out of 1600, 27%)	n = 219 (out of 800, 27%)	n = 213 (out of 800, 27%)
globally normal studies		N = 54	N = 28	N = 26
globally abnormal studies		N = 12	N = 7	N = 5
regionally abnormal studies		N = 34	N = 15	N = 19

3.3.2 Performance of RS_{CT} for detection of wall motion abnormality

3.3.2.1 Histograms of peak RS_{CT} in the training and validation cohorts

Figure 3.2 shows the histogram of peak RS_{CT} for both cohorts. We observed that all RS_{CT} intervals had one class dominating at least 80% of the data within the 0.05 bin width, except the interval from -0.20 to -0.15 where the two classes are nearly evenly distributed

(normal: abnormal = 37:27 in training and 44:33 in validation). No significant structure within this bin was seen when the bin width was reduced as shown by the insert figure.

3.3.2.2 ROC curves for RS_{CT}, Definition of optimal RS_{CT} Threshold

Figure 3.3 is the ROC curve of the training cohort that shows the corresponding sensitivity and specificity at different classification thresholds of RS_{CT}. AUC = 0.991 suggests RS_{CT} is an outstanding classifier.

From the curve, we defined the optimal threshold RS_{CT}^* = -0.20 which maximized the summation of sensitivity and specificity. This RS_{CT}^* led to sensitivity = 0.95, specificity = 0.95, true positive rate = 0.87 and accuracy = 0.95 (see **Table 3.2**). The Cohen's kappa value = 0.87 (95% CI = [0.89,0.85]) also indicates strong agreement with expert labeling.

We demonstrated high performance of RS_{CT}^* on each of 16 AHA segments (see **Table 3.3**), with 1 AHA segment (basal anteroseptal) having accuracy below 0.90 (=0.84), 5 AHA segments having accuracy between 0.90 to 0.95 and the remaining 10 segments having accuracy above 0.95.

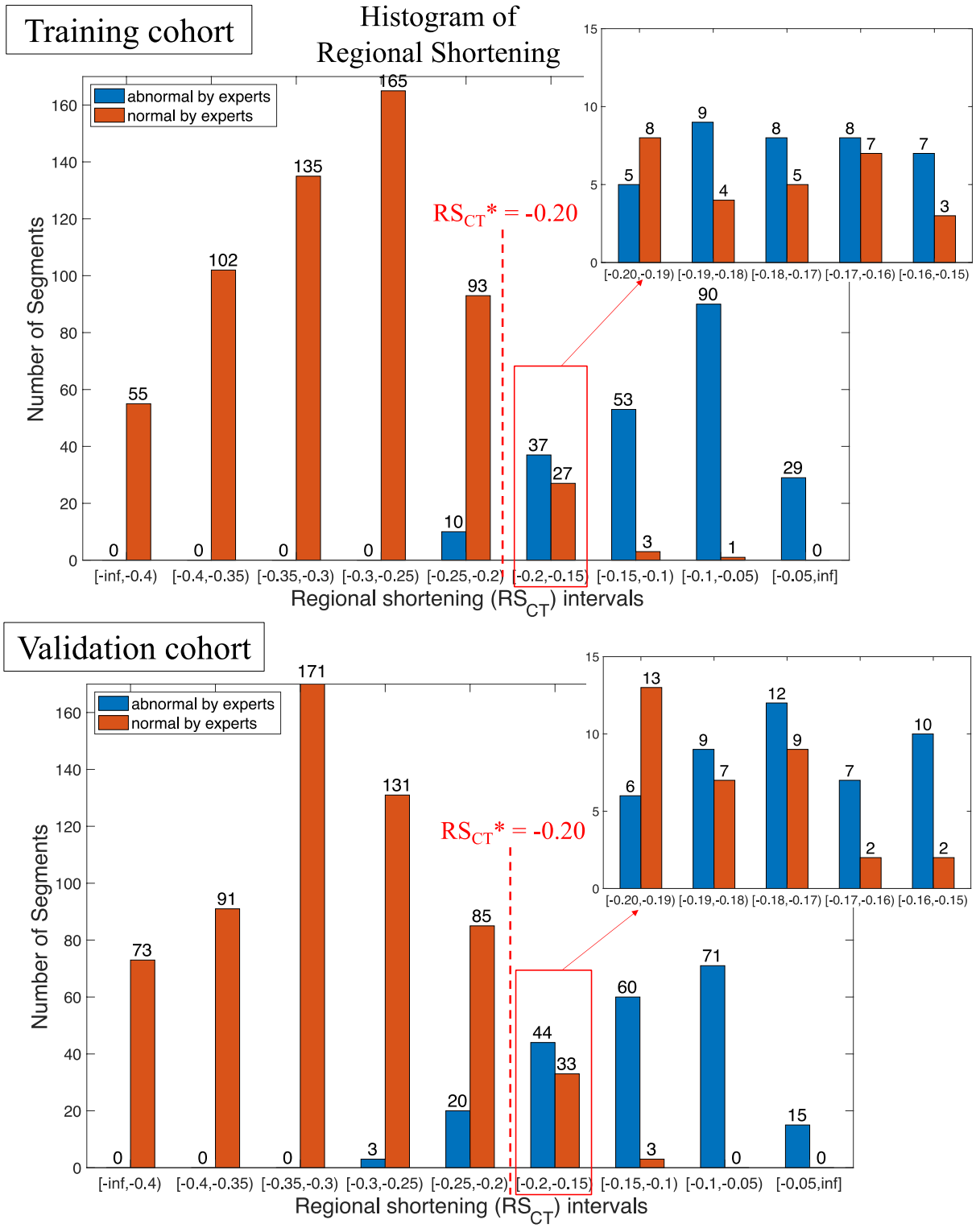

Figure 3.2. Histogram of the number of segments for peak RS_{CT} intervals for (a) training and (b) validation cohort. A zoomed-in histogram was made for RS_{CT} interval with the highest overlap in class (-0.20 to -0.15). The optimal threshold RS_{CT}*= − 0.20 is also shown.

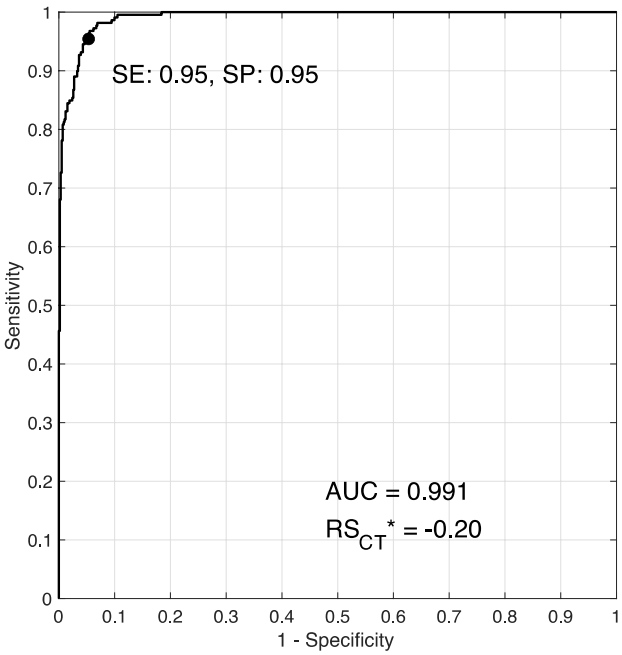

Figure 3.3. ROC curve of RS_{CT} as a decision classifier in the training cohort. The threshold ranges from -0.6 at the most left to 0 at the most right. AUC = 0.991. The optimal threshold RS_{CT}* (black dot) was -0.20 leading to sensitivity = 0.95 and specificity = 0.95. SE = sensitivity. SP = specificity.

Table 3.2. Classification performance of RS_{CT}* in the training and validation cohorts. SE = sensitivity, SP = specificity, TPR = true positive rate, AC = accuracy, Kappa = Cohen's Kappa value.

		Training		Validation	
		Expert Visual Label		Expert Visual Label	
		Abnormal	Normal	Abnormal	Normal
RS_{CT}	Abnormal	209	31	190	36
	Normal	10	550	23	551
		SE	0.954	SE	0.892
		SP	0.947	SP	0.939
		TPR	0.871	TPR	0.841
		AC	0.949	AC	0.926
		Kappa	0.874	Kappa	0.815

3.3.2.3 RS_{CT} performance on validation data*

The same RS_{CT}* was applied to all 800 segments in the validation cohort and demonstrated high performance as well (sensitivity = 0.89, specificity = 0.94, true positive rate = 0.84, and accuracy = 0.93). The Cohen's kappa value = 0.82 (95% CI = [0.80, 0.84]) indicated

strong agreement with expert labeling. For the performance of RS_{CT}* on each of 16 AHA segments, 3 AHA segments (basal anteroseptal, basal inferoseptal, apical septal) had accuracy between 0.86 to 0.90, 9 AHA segments had accuracy between 0.90 to 0.95 and the remaining 4 AHA segments had accuracy above 0.95.

3.3.3 Exploratory Analysis of AHA-segment-specific optimal $RS_{CT,AHA}$*

In the preceding analyses, we defined a single optimal threshold RS_{CT}* for all AHA segments. In further exploratory analysis, we sought to test the improvement when different thresholds ($RS_{CT,AHA}$*) were used for each specific AHA segment. **Figure 3.4** illustrates that $RS_{CT,AHA}$* ranged from -0.16 to -0.23 across different AHA segments and lower values occurred in the basal anteroseptal (= -0.16), basal inferoseptal (= -0.18) and basal inferior (= -0.17) AHA segments. The AUC was ≥0.97 for all AHA segments.

Table 3.4 shows the improvement in sensitivity and specificity as well as the net re-classification improvement (NRI, according to Equation 3) for each AHA segment in the validation cohort obtained by using $RS_{CT,AHA}$*. NRI ≥0 for all AHA segments and is higher in AHA segments with relatively lower performance using RS_{CT}. For example, in the basal anteroseptal segment, $RS_{CT,AHA}$* correctly reclassified 6 expert-labeled normal segments, improving specificity from 0.81 to 1.00 (NRI = 0.132). Similarly, in the apical septal segment, $RS_{CT,AHA}$* correctly reclassified 4 expert-labeled abnormal segments, improving sensitivity from 0.75 to 1.00 (NRI = 0.191). Overall, using $RS_{CT,AHA}$* improved the total sensitivity in the validation cohort from 0.89 to 0.94 and NRI = 0.049 (last row of **Table 3.4**).

Table 3.3 Classification performance of RS_{CT}* for each AHA segment. A = Anterior, AS = Anteroseptal, IS = Inferoseptal, I = inferior, IL = Inferolateral, AL = Anterolateral.

RS_{CT}*	-0.20	Training					Validation				
		No. of abnormal	No. of normal	SE	SP	AC	No. of normal	No. of abnormal	SE	SP	AC
Basal	A	8	42	1.00	0.95	0.96	12	38	1.00	0.92	0.94
	AS	16	34	1.00	0.77	0.84	18	32	1.00	0.81	0.88
	IS	16	34	0.94	0.94	0.94	18	32	0.89	0.84	0.86
	I	11	39	1.00	0.95	0.96	8	42	0.88	0.91	0.90
	IL	12	38	1.00	0.97	0.98	9	41	0.78	1.00	1.00
	AL	10	40	1.00	0.95	0.96	9	41	1.00	0.90	0.92
Mid	A	11	39	1.00	1.00	1.00	14	36	0.86	0.97	0.94
	AS	17	33	0.94	1.00	0.98	16	34	0.94	0.91	0.92
	IS	15	35	1.00	0.94	0.96	14	36	0.86	0.94	0.92
	I	14	36	0.86	0.97	0.94	12	38	0.83	1.00	0.96
	IL	14	36	0.93	0.94	0.94	11	39	0.91	0.95	0.94
	AL	14	36	0.93	0.92	0.92	12	38	1.00	0.97	0.98
Apical	A	13	37	0.92	0.97	0.96	15	35	0.87	1.00	0.96
	S	16	34	0.94	0.97	0.96	16	34	0.75	0.94	0.88
	I	18	32	0.94	1.00	0.98	14	36	0.86	0.94	0.92
	L	14	36	0.93	0.89	0.90	15	35	0.87	0.97	0.94

3.3.4 Data Adequacy

Adequacy of our training cohort was evaluated via the variability of the optimal threshold RS_{CT}* picked when randomly sampling 80% of the dataset. **Figure 3.5** shows that the variability, represented by the width of the 95% CI (= CI upper boundary – CI lower boundary), decreased from 0.032 to 0.015 when of the cohort increased from 10 studies (160 segments) to 50 studies (800 segments). The mean values of the threshold were always approximately -0.20.

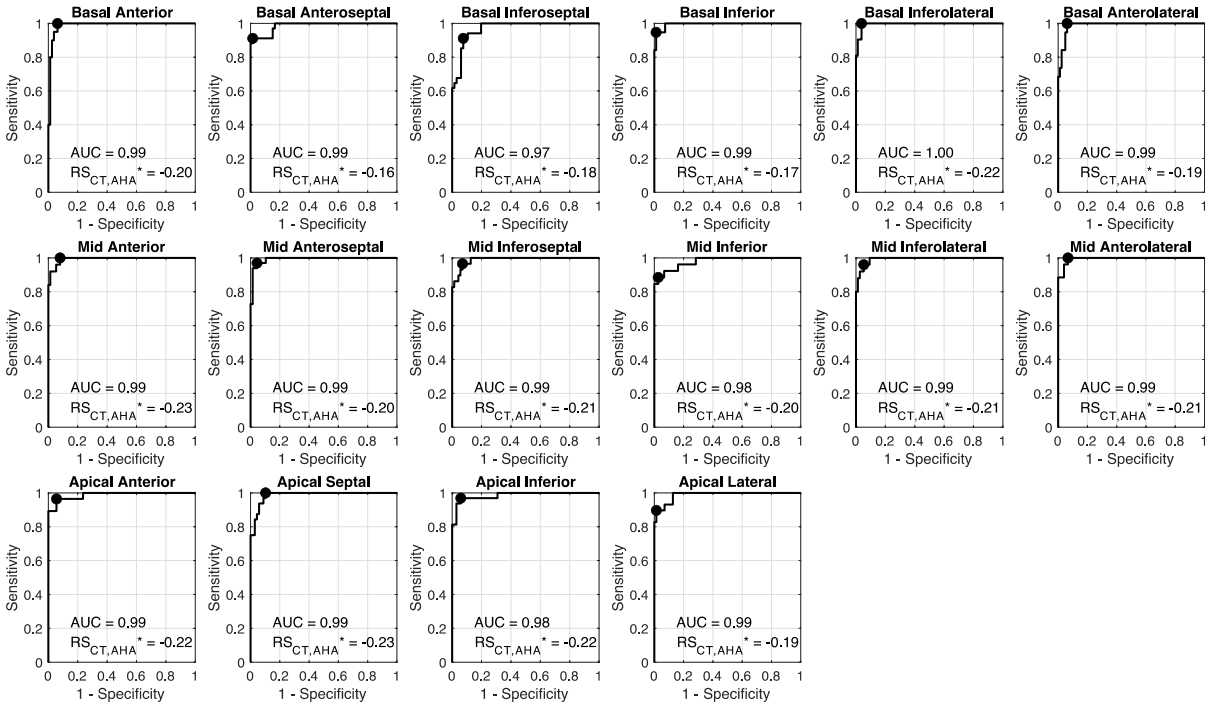

Figure 3.4. ROC curves of regional shortening $RS_{CT,AHA}$* for each of 16 AHA segment. The entire dataset (n=100) was used here. Black dots represent the individual optimal threshold $RS_{CT,AHA}$* for different AHA segments.

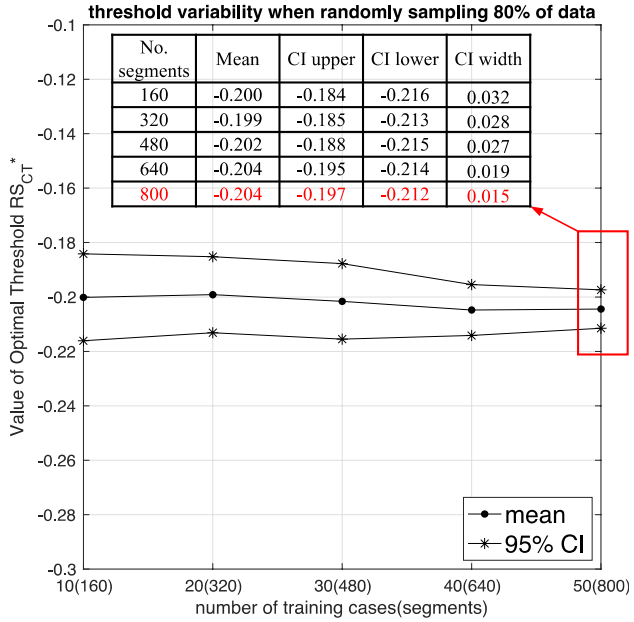

Figure 3.5. Data adequacy. Line with circular dots represent the change of mean value of optimal thresholds and the line with asterisks represent upper and lower boundary of 95% confidence interval (CI).

3.3.5 Interobserver Agreement

Our three readers had an interobserver agreement of classifying a segmental wall motion into normal vs. abnormal, measured via Fleiss's Kappa, of 0.746, which indicates strong agreement. When including the degree of dysfunction function (scores 1, 2 and 3 for a segment), the Kappa dropped to 0.291, which reflects "fair" agreement in sub-classify an abnormal segment into hypokinetic, akinetic and dyskinetic.

Table 3.4. Re-Classification in validation cohort by using $RS_{CT,AHA}$* instead of RS_{CT}*. The 8th, 9th, 10th and 11th columns correspond to $N_{event,correctly-reclassify}$, $N_{event,incorrectly-reclassify}$, $N_{nonevent,correctly-reclassify}$ and $N_{nonevent,incorrectly-reclassify}$ in the Equation 3.3 respectively. SE = sensitivity, SP = specificity. A = Anterior, AS = Anteroseptal, IS = Inferoseptal, I = inferior, IL = Inferolateral, AL = Anterolateral.

		use RS_{CT}* = -0.20		use $RS_{CT,AHA}$*							
							Event: expert label abnormal		Non-event: expert label normal		
		SE	SP	$RS_{CT,AHA}$*	SE	SP	correct relabel	incorrect relabel	correct relabel	incorrect relabel	NRI
Basal	A	1.00	0.92	-0.19	1.00	0.92	0	0	0	0	0.000
	AS	1.00	0.81	-0.16	0.94	1.00	0	1	6	0	0.132
	IS	0.89	0.84	-0.18	0.89	0.91	0	0	2	0	0.063
	I	0.88	0.91	-0.17	0.88	0.98	0	0	3	0	0.071
	IL	0.78	1.00	-0.22	1.00	0.98	2	0	0	1	0.198
	AL	1.00	0.90	-0.19	1.00	0.93	0	0	1	0	0.024
Mid	A	0.86	0.97	-0.23	1.00	0.92	2	0	0	2	0.087
	AS	0.94	0.91	-0.20	0.94	0.91	0	0	0	0	0.000
	IS	0.86	0.94	-0.20	0.86	0.94	0	0	0	0	0.000
	I	0.83	1.00	-0.20	0.83	1.00	0	0	0	0	0.000
	IL	0.91	0.95	-0.21	0.91	0.95	0	0	0	0	0.000
	AL	1.00	0.97	-0.21	1.00	0.97	0	0	0	0	0.000
Apical	A	0.87	1.00	-0.22	0.93	0.94	1	0	0	2	0.010
	S	0.75	0.94	-0.23	1.00	0.88	4	0	0	2	0.191
	I	0.86	0.94	-0.22	0.93	0.89	1	0	0	2	0.016
	L	0.87	0.97	-0.19	0.87	1.00	0	0	1	0	0.029
total		0.89	0.94		0.94	0.94	10	1	13	9	0.049

3.4 Discussions

3.4.1 Main Findings

The primary result from this work is that regional shortening RS_{CT} derived via 4DCT surface feature tracking[87] can be used as an outstanding quantitative decision classifier to detect segmental LV WMA from routine 4DCT scans (AUC = 0.991). An optimal classification threshold RS_{CT}* =-0.20 (applied to all 16 AHA segments) led to high detection accuracy (= 0.95) and strong agreement (kappa = 0.87) with expert visual detection. Using an independent validation cohort, we validated the threshold by high detection accuracy = 0.93 and strong agreement with experts (kappa = 0.82).

3.4.1.1 AHA-segment-specific optimal threshold

We obtained a secondary result from an exploratory analysis using all 100 studies to evaluate the improvement in performance via the use of AHA-segment-specific RS_{CT} thresholds. There are two key results. First, the small range of $RS_{CT,AHA}$* values (from -0.16 to -0.23) suggests that the uniform RS_{CT}* = -0.20 chosen in our main study is broadly appropriate. The variance in $RS_{CT,AHA}$* may be explained by (1) different mechanical properties of the LV septal wall and free wall, (2) variance in the performance of the point registration algorithm in basal segments since the meshes are missing trabecular tracking features in the left ventricular outflow tract (LVOT) and (3) limited sample size.

Second, this exploratory analysis shows the promise of AHA-segment-specific threshold to further improve the detection performance. **Table 3.4** shows that re-classification using $RS_{CT,AHA}$* (instead of a single RS_{CT}*) improved the detection performance for some AHA segments (e.g., basal anteroseptal, apical septal, NRI>0) and for the entire validation cohort (NRI

= 0.049). However, due to the small numbers the clinical significance of this NRI remains unclear. It is possible that these findings represent an overfitting of the values observed in our population. Thus, a larger study in which each AHA segment has sufficient normal and abnormal cases is needed to fully evaluate the need for segment-specific thresholding.

3.4.2 Data adequacy

We showed that the mean value of the optimal threshold using random sampling always remained around -0.20. By increasing the number of studies in the training cohort, we could stabilize the optimal threshold by decreasing width of the 95% CI. However, the overall performance did not change significantly.

3.4.3 Limitations

The first limitation is that we defined a threshold to separate normal wall motion from all three categories of hypokinetic wall motion since we combined expert scores 1-3 (hypokinetic, akinetic and dyskinetic) into one "abnormal" class. This was done because (1) the small number of akinetic and dyskinetic segments would lead to severe class imbalance, (2) the interobserver agreement in classifying an abnormal motion as hypokinetic, akinetic or dyskinetic was poor (Kappa = 0.29). This poor interobserver agreement result highlights the need for an objective, non-biased classifier to be developed for this task. Future work is planned to evaluate appropriate thresholds to classify LV wall motion into all four classes.

Second, disagreement between RS_{CT} and expert evaluation may be partially due to the way the images are evaluated. RS_{CT} quantitatively evaluated the 3D shortening only on the endocardial surface, while the experts viewed 2D cardiac imaging planes and could evaluate both

epi- and endocardial surface motions. Therefore, differences (1) between 3D motion and 2D motion and (2) between endocardial surface and full myocardial evaluation may partially explain the small rate of disagreement between RS_{CT} and expert visual labels.

3.4.4 Clinical Significance

Our study has shown that RS_{CT} measured from cardiac 4DCT studies not only provides quantitative evaluation of the LV segmental wall motion, but also can serve as an objective method to detect LV WMA. Both segmental RS_{CT} values and the classification of wall motion based on RS_{CT} threshold (RS_{CT}*) used as an objective classification tool. To further validate and optimize RS_{CT} threshold values, future studies that include larger patient cohorts from multiple centers are required.

3.4.5 Conclusion

Regional myocardial shortening from CT (RS_{CT}) is a highly accurate classifier to detect segmental LV wall motion abnormalities from 4DCT studies. An optimal classification threshold of $RS_{CT} > -0.20$ was defined to obtain high detection performance in all 16 AHA segments both in a training and validation cohort. Using AHA-segment-specific optimal thresholds may further improve detection performance but requires further evaluation.

3.5 Acknowledgement

Chapter 3, in full, has been submitted for publication of the material as it may appear in "Thresholding of Regional Shortening Measured from 4D Cardiac CT Angiograms Accurately Detects the Presence of LV Wall Motion Abnormalities", Zhennong Chen, Francisco Contijoch,

Francisco Contijoch, Andrew M. Kahn, Seth Kligerman, Hari Narayan, Ashish Manohar, Elliot McVeigh, 2022. The dissertation author was a primary author of this paper.

Chapter 4: Automated Cardiac Volume Assessment and Cardiac Long- and Short-Axis Imaging Plane Prediction from ECG-gated CT Volumes Enabled By Deep Learning

4.1 Introduction

As reviewed in Chapter 1, accurate and reproducible assessment of LV morphology and function is crucial as LV volumes, ejection fraction (EF), global and regional myocardial strain are critical parameters used in the diagnosis[11], clinical management, prognostication, and follow-up of numerous cardiovascular and systemic diseases[12,13]. In addition, regional LV wall motion abnormalities for 17 AHA LV segments are assessed using standardized views and are important for the evaluation of cardiac pathology, including coronary artery disease (CAD)[164,166]. Beyond the LV, the assessment of the left atrium (LA) provides additional insight into cardiovascular disease and function, and is particularly important in evaluating patients with atrial fibrillation, valvular disease, and diastolic heart failure[174].

Cardiac CT is a safe and cost-effective non-invasive imaging modality for the evaluation of suspected CAD[175] and acute chest pain[176]. Cardiac CT is an important prognostic tool in CAD and can be used to follow-up patients with atherosclerosis who are at increased risk of worsening stenosis severity and number of coronary vessels involved[177]. While qualitative morpho-functional assessment is possible by reviewing phases of the cardiac cycle in a cine loop, *quantitative* assessment requires accurate segmentation, often requiring manual annotation of the images, which is time-consuming and highly dependent on user's training and experience. Further, as images are acquired volumetrically, visualization of wall motion abnormalities requires re-slicing standard cardiac imaging planes such as multiple long-axis (LAX) planes and one short-axis (SAX) stack[178]. Currently, this requires specialized viewing software[179] and manual processing which may lead to inter-reader variability, limiting clinical use.

Several deep learning (DL) algorithms have been developed for cardiac image segmentation[125,180] but an approach that can perform segmentation *and* re-slice standard cardiac imaging planes simultaneously has not been described. For segmentation, section 1.5.2 has included an overview of different DL-based segmentation techniques. These techniques can be classified based on their inputs. First, CT image is divided into small patches[114,115], which are used as inputs for the DL model to label pixels in the patch that belong to cardiac chambers. Second, three orthogonal projections (axial, coronal and sagittal)[116,117] have been used as model inputs and the predicted segmentations in three projections are fused together to make an intact 3D segmentation. Third, 2D "U-Net"[118] takes each CT slice as the input to provide the pixel-wise segmentation in a slice-by-slice fashion. Baskaran et al.[119] successfully applied a 2D U-Net to segment four chamber images in cardiac CT with high accuracy (Dice > 0.91). Fourth, Some of the current efforts[120,121] in the 3D U-Net takes the entire CT volume as the input. These 3D U-Net approaches combined a localization network for a coarse pre-detection of heart and then applied 3D U-Net to the detected region for the segmentation. For plane re-slicing, Vigneault et al[181] modified a conventional U-Net to predict scaling and rotation of 2D MRI images. Predicting short and long-axis imaging planes of CT requires significant global context, so probably the entire CT volume should be learnt by the DL model.

We propose a variant of a 3D U-Net that performs pixel-wise segmentation and simultaneously predicts vectors which define the short and long-axis imaging planes. We hypothesized that down-sampled 3D volumes will maintain sufficient network complexity and image information for accurate blood-pool segmentation and plane slicing. Further, our approach leverages similarities between the tasks and provides a fast, automatic and reproducible method to both assess left-sided heart chamber volumes and function and generate standard cardiac

imaging planes from volumetric cardiac CT images. This would increase clinical utility and reproducibility by avoiding the need for manual interaction. In this study, we test the ability of this DL framework to perform automated multi-chamber segmentation and long- and short-axis plane re-slicing of cardiac CT image volumes.

4.2 Materials and Methods

4.2.1 Training Population

Studies for training were identified from an existing cohort of patients with available expert segmentations. Under institutional review board approval, 100 ECG-gated contrast enhanced, cardiac CT studies between June 2012 and June 2018 were retrospectively identified as meeting the inclusion criteria defined below.

Strict inclusion criteria were utilized to maximize training quality: each study had (*a*) reconstructed images across the entire cardiac cycle at 10% intervals and (*b*) sufficient quality for blood-pool segmentation as determined by image analysis expert (author D.M.V.) and slice planning as determined by a cardiovascular imaging expert (author M.R.). Manual segmentations of LV and LA blood-pool were generated using a standardized processing pipeline (described below). For each patient, two frames (end-diastole (ED) and end-systole (ES)) served as training samples for the DL model.

Training images were collected at 2 institutions (67 UCSD, 33 NIH) with 3 CT systems. Two were long z-axis scanners with 256 detector rows (GE Revolution, n=41 studies) and 320 detector rows (Toshiba AquilionONE, n=47) allowing for a single heartbeat axial 16cm acquisition throughout the cardiac cycle. Retrospective gating using a conventional low-pitch (0.18 ± 0.02, range 0.16 - 0.22) helical acquisition over several heart beats was used with the

third scanner (Siemens SOMATOM Force, n=12). The training studies were performed for clinical cardiac indications: preoperative assessment of patients undergoing transcatheter aortic valve replacement (TAVR, n=39), suspected coronary artery disease (CAD, n=38), and pre-operative assessment of pulmonary vein ablation (PVA, n=23).

4.2.2 Manual Segmentation and Volumetric assessment

Pixel-wise manual segmentations of the LV and LA blood volumes, LV_m and LA_m respectively were confirmed by an image analysis expert (author D.M.V.) with 7 years of experience in cardiac image segmentation using ITK-SNAP (Philadelphia, PA USA)[169]. From each segmentation, blood chamber volumes were obtained, and the function of each chamber was measured via ejection fraction ($LVEF_m$ and $LAEF_m$, respectively).

4.2.3 Manual Imaging Planes and Plane Vectors

Manual cardiac imaging planes were defined from the volumetric scans according to standardized guidelines[182] by a fellowship-trained cardiovascular imaging expert (author M.R.). A SAX plane at the level of the mitral valve (MV_m), a two-chamber plane ($2CH_m$), a three-chamber plane ($3CH_m$) and a four-chamber plane ($4CH_m$) were identified for each patient. The short-axis stack (SAX_m) of images was defined to span from the MV_m to the LV apex using 8mm slice spacing. Each plane was described by three vectors: $\vec{x}_m$ and $\vec{y}_m$ (defining the plane's orientation) and $\vec{t}_m$ (defining the plane's center). These vectors are illustrated in **Figure 4.1A**.

4.2.4 Model Architecture

The DL model is an adaptation of the standard U-Net architecture[118] with two modifications: 1) 3D convolution, maxpooling and upsampling layers were utilized to accommodate 3D CT image volumes as the input and 2) a fully-connected layer was added after the last max-pooling layer in the down-sampling path to regress the plane vectors (**Figure 4.1B**). 3D CT images at ED and ES were resampled to 1.5 mm isotropic voxels for all patients. The DL model labels each voxel as one of three classes (LV, LA or background). The three vectors ($\vec{t}_{\mathrm{DL}}$, $\vec{x}_{\mathrm{DL}}$ and $\vec{y}_{\mathrm{DL}}$) were predicted using three individual fully-connected layers. The total loss of the model was defined to be:

$$Total\ Loss\ = w_{seg}L_{seg}\ + w_tL_t\ + w_xL_x\ + w_yL_y$$

with w_i (i = *seg, t, x, y*) the weight assigned to each loss: L_{seg} the categorical cross-entropy loss of the segmentation, L_t the mean square error of the predicted translation vector $\vec{t}_{\mathrm{DL}}$, L_x the cosine proximity error for $\vec{x}_{\mathrm{DL}}$, and L_y the cosine proximity error for $\vec{y}_{\mathrm{DL}}$.

4.2.5 Model Training

Training was performed in stages. The first stage ("Model-S") was trained to perform LV and LA segmentations ($\mathrm{LV_{DL}}$ and $\mathrm{LA_{DL}}$, respectively) by assigning $w_{seg} = 1$, $w_t = w_x = w_y = 0$. "Model-S" served as the initialization for the training of subsequent cardiac plane models. For each plane, two models were trained: one predicted the translation vector $\vec{t}_{\mathrm{DL}}$ ("Model-T": $w_{seg} = w_t = 1$, $w_x = w_y = 0$) while another predicted directional vectors $\vec{x}_{\mathrm{DL}}$ and $\vec{y}_{\mathrm{DL}}$ ("Model-D": $w_{seg} = w_x = w_y = 1$, $w_t = 0$). Each plane (2CH, 3CH, 4CH, and MV) was trained individually which led to 4 translation-vector models and 4 direction-vector models, and independent prediction of planes. Models were trained on ED and ES image volumes. Training and validation were performed

using 5-fold cross-validation with random shuffling for robust unbiased evaluation. As a result, each model was trained on 80 studies (160 volumes) and evaluated on 20 validation studies (40 volumes). We report model performance across all folds.

4.2.6 Model Evaluation and Statistics

Chamber Segmentation and Assessment of Function

DL segmentation accuracy was evaluated using the Dice coefficient (a volumetric metric) and Hausdorff distance (a surface-based metric). Dice coefficient is defined as $2(|V_{manual} \cap V_{DL}|) / (|V_{manual} + V_{DL})$ and measures the overlap between manual and DL segmentation. The Hausdorff distance measures the local maximum distance between two surfaces S_{manual} and S_{DL}. Differences in segmentation accuracy between CT vendors and between different clinical indications were evaluated using one-way analysis of variance (ANOVA) for Dice scores.

Accuracy of the segmentation-derived functional assessment was evaluated by comparing EF_{DL} to manually derived EF_m.

Figure 4.1. DL model training approach and model architecture. (A): 3D CT volumes were first resampled to uniform spatial resolution (1.5mm isotopically) and uniform dimension (160x160x96) and then served as an input to all models. **Step 1**: Model-S was trained to predicted LV_{DL} (red) and LA_{DL} (green). **Step 2**: Model-T and Model-D were initialized by Model-S and then trained to predict imaging plane vectors $\vec{t}_{DL,}$ $\vec{x}_{DL}$ and $\vec{y}_{DL}$. A graphic illustration of these three vectors in relationship to the image volume is shown. The blue cube represents the CT volume with a re-sliced plane in black. The blue dot is the center of volume and black dot is the center of plane. $\vec{t}$ is the displacement between the blue and black dot and $\vec{x}$ and $\vec{y}$ are directional vectors of the two-dimensional plane in the volume's coordinate system. **(B)** U-Net architecture with added branch consisting of 4 fully-connected layers after the last max-pooling layer in the down-sampling path was used. Conv3D = 3D convolution layer.

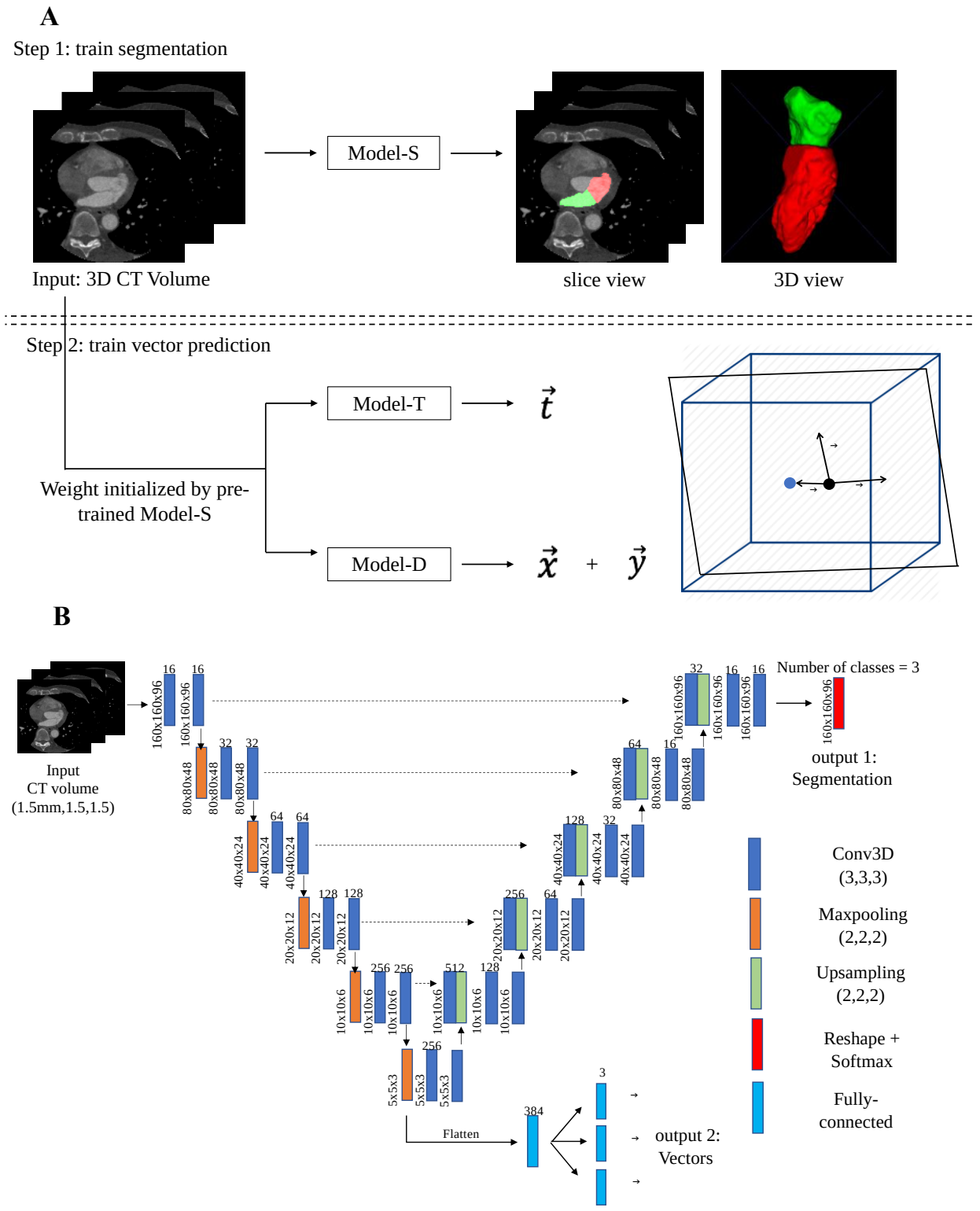
A
Step 1: train segmentation
Model-S
Input: 3D CT Volume
slice view
3D view
Step 2: train vector prediction
Model-T
Weight initialized by pre-trained Model-S
Model-D
B
Input
CT volume
(1.5mm,1.5,1.5)
Number of classes = 3
output 1:
Segmentation
output 2:
Vectors
Flatten
Conv3D
(3,3,3)
Maxpooling
(2,2,2)
Upsampling
(2,2,2)
Reshape +
Softmax
Fully-
connected

Quantitative Evaluation of DL-predicted Imaging Plane Vectors

$2CH_{DL}$, $3CH_{DL}$, $4CH_{DL}$, and MV_{DL} planes were derived from three predicted vectors output by "Model-T" and "Model-D". SAX_{DL} was defined to be parallel to MV_{DL} and span the LV as defined by the DL segmentation. For each plane, the differences between DL prediction $Plane_{DL}$ and the manual plane $Plane_m$ was assessed via the displacement error Δd between center of $Plane_{DL}$ and that of $Plane_m$ and angulation error $\Delta\theta$ of $Plane_{DL}$:

$$\Delta d = \sqrt{\sum_{i=1}^{3} (\vec{t}_{m,i} - \vec{t}_{DL,i})^2} \qquad (Equation\ 4.1)$$

$$\Delta\theta = cos^{-1}\left(\frac{\vec{n}_m \cdot \vec{n}_{DL}}{\|\vec{n}_m\| \times \|\vec{n}_{DL}\|}\right) \qquad (Equation\ 4.2)$$

where normal vectors $\vec{n}$ were calculated as the cross product of $\vec{x}$ and $\vec{y}$ and $\|\vec{n}\|$ is the vector length.

Inter and Intra-reader Differences in Imaging Plane Vectors

10 studies were randomly selected to assess inter- and intra-reader differences in manual delineation of cardiac planes. Reader 1 was the cardiac imaging expert mentioned above (author M.R.) who generated the plane annotations for DL training and Reader 2 was a fellowship-trained cardiothoracic radiologist with 12 years of experience (author S.K.). Inter-reader differences were assessed by comparison of this 10-study subset of $Plane_{m1}$ defined by Reader 1 to $Plane_{m2}$ defined by Reader 2. Intra-reader differences were assessed via repeat delineation by Reader 1 six months after initial plane definition.

The DL algorithm was trained on annotations made by Reader 1. Therefore, two tests were used to evaluate DL predicted planes. First, the difference between the DL and Reader 1 on

the study subset described above was compared to intra-reader differences. Second, the difference between DL planes and those defined by Reader 2 was compared to inter-reader differences.

Visual Assessment of Plane Quality

For unbiased assessment of the DL performance, Reader 2 assessed, in a randomized, blinded fashion, both the manual planes used for training ($Plane_{m,}$ defined by Reader 1) and resulting DL-predicted planes ($Plane_{DL}$). The example of images provided to the expert reader for visual assessment can be found in **Figure 4.2**. Each plane was scored as one of four classes: perfect, excellent, good and inadequate with the first three classes considered as diagnostically adequate. The first three classes were considered as diagnostically adequate. Perfect was defined when planes were ideal and did not require any adjustment; excellent was defined when planes were nearly optimal without loss of diagnostic quality but might need slight adjustment in location or angulator; good was defined when planes had mild loss of diagnostic quality and might need moderate adjustment. LAX planes were labeled inadequate if the correct anatomy was not visualized or if planes did not cut through the appropriate myocardial walls. SAX planes were labeled inadequate if planes had incorrect angulation or incomplete ventricular coverage.

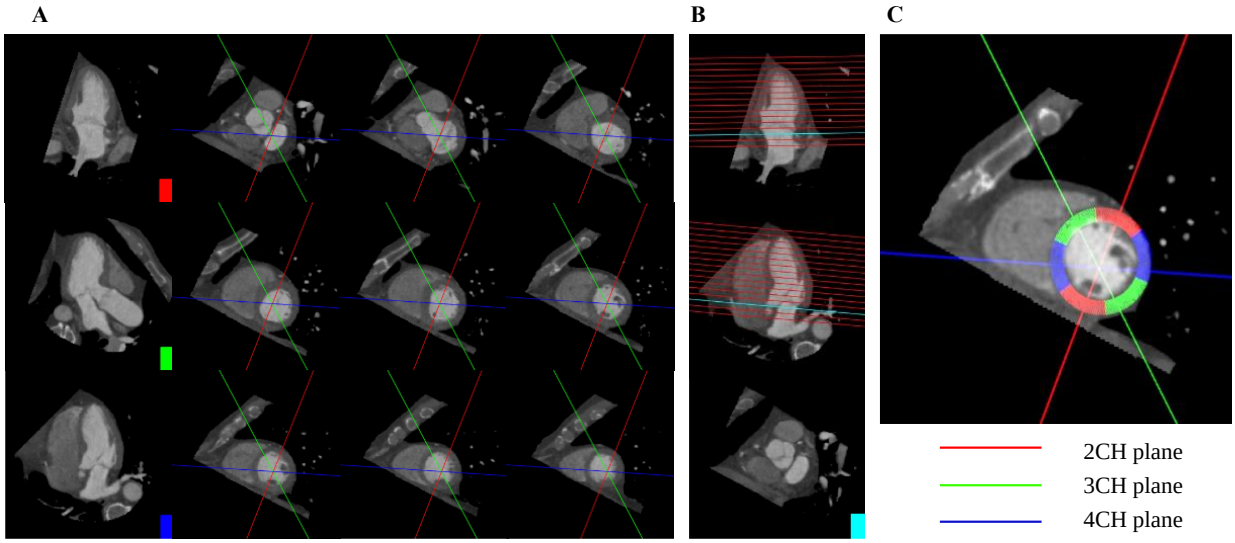

Figure 4.2. Example of images provided to the expert reader for visual assessment. (A) The three LAX planes (red: 2CH, green: 3CH, and blue: 4CH) were displayed in the first column and were plotted as solid lines on the manually defined SAX stack with the corresponding colors. **(B)** The SAX stack derived from MV plane (cyan) were displayed as a stack of solid lines in manually defined two- and four-chamber planes. Note that the LAX planes in figure A and SAX planes in figure B were either $Plane_m$ or $Plane_{DL}$, and their positions were shown as lines in the manually defined SAX/LAX planes to aid the cardiologist for better visualization. **(C)** Annotation of AHA segment visualization. 6 AHA segments were identified at the mid-ventricle SAX plane, and lines representing three LAX planes were overlaid to identify whether the planes satisfied the following criteria: 2CH plane must bisect the mid inferior (bottom red arc) and mid anterior (top red arc) walls; the 3CH plane must bisect the mid-inferolateral (bottom green arc) and mid anteroseptal (top green arc) walls; the 4CH must bisect the mid-inferoseptal (left blue arc) and mid-anterolateral (right blue arc) walls. CH = chamber.

Quantitative assessment of slice position: AHA wall assessment

The AHA 17-segment model was used to assess whether manual and DL-predicted long-axis planes intersected the corresponding AHA segment at the mid-ventricular slice (**Figure 4.2C**).

Run-time for DL-based Approach

We performed all DL trainings by using Keras (https://keras.io/) with TensorFlow (https://www.tensorflow.org/) on an 8-core Ubuntu (version: 18.04.3) workstation with 32 GB RAM equipped with a GeForce GTX 1080 Ti (NVIDIA Corporation, Santa Clara CA).

The times needed to train the models and to predict the DL chamber segmentations at ED and ES as well as vectors for four planes (three LAX and one MV plane) were recorded for each study.

4.2.7 Testing Population

We tested our approach on 144 consecutive ECG-gated cardiac cine CT studies acquired at our institution between January and December 2019 under the same IRB approval. Studies were independent from training data. All studies had complete cardiac cycle reconstructions, radiology reports which assessed cardiac function, and a field-of-view which captured the entire LA and LV chambers. Studies were not included if the patients had congenital heart disease, images were taken for lead extraction planning, or they had metal implants in the LA or LV (e.g., mitral valve or leads in the LV chamber). Studies with coronary stents were not excluded. The testing studies were performed for the following clinical cardiac indications: suspected CAD (n = 74), pre-operative assessment of PVA (n = 48), TAVR (n = 10), and others (n = 12). For each case, the diagnostic utility of DL-predicted frames was scored independently by Reader 2 and Reader 3 (author L.H., a fellowship-trained cardiovascular radiologist) using the same criteria defined above. In addition, each reader made a visual prediction of LV ejection fraction (to the nearest 5%) which was compared to the automated segmentation value.

To highlight the utility in evaluation of segmental LV wall motion abnormality (WMA), we show four studies with radiologically confirmed diagnosis of coronary artery disease: 1) right coronary artery stenosis with inferior wall WMA, 2) left anterior descending stenosis with anterior, anteroseptal wall and apical cap WMA, 3) left circumflex stenosis with mild WMA in the inferolateral wall, and 4) three vessel stenosis with globally reduced cardiac function. All stenoses and corresponding WMA were identified on clinical radiologic assessment. To assess the utility of $Plane_{DL}$ in longitudinal CT imaging, we show the $Plane_{DL}$ generated for two CT studies obtained 71 days apart in the same patient (before and after chemotherapy) as part of cardio-oncology evaluation.

4.2.8 Statistical Evaluation

Unless otherwise indicated above, data are reported as median (with interquartile range) given non-normality on Shapiro-Wilk testing. Pearson correlation and two-tailed paired Student's t-test were performed to test agreement between the DL- and manually-derived EF. Two-tailed categorical z-test was used to evaluate differences in the proportion of successful intersecting between $Plane_{DL}$ and $Plane_{m}$. Spearman correlation was used to assess visual and DL-derived EF in the validation cohort. Statistical significance was set at a $p \leq 0.05$. All analyses were performed in Python version 3.6 with scipy (version 1.1.0).

4.3 Results

Of the 100 patients used for training, 60 (60%) were male (age: 67±16) and 40 (40%) were female (age 69±18). The blood-pool in the training data had a median intensity of 495 HU (IQR: 401,607, range: 277-885 HU) for the LV and 541 HU (IQR: 429,664, range: 257-1014 HU) for the LA.

Of the 144 patients used for testing, 89 (61.8%) were male (age: 59±16) and 55 (38.2%) were female (age: 63±15). The blood-pool in the testing data had a median intensity of 525 HU (IQR: 433,616, range: 320-1022 HU) for the LV and 544 HU (IQR: 451,632, range: 295-1207 HU) for the LA.

4.3.1 Chamber Segmentation and Assessment of Function

DL-predicted segmentations had median Dice coefficients of 0.907 (IQR: 0.884,0.932) and 0.931 (IQR: 0.913,0.954) (**Figure 4.3A**), and median Hausdorff distances of 6.2mm (IQR: 3.7,8.2) and 7.3mm (IQR: 5.6,9.6) for the LV and LA, respectively (**Figure 4.3D**). There were no statistically significant differences ($p>0.05$) in Dice across vendors, but Dice in the LA did vary with respect to clinical indications ($p=0.001$) on ANOVA testing (**Figure 4.3B and 4.3C)**.

There was close agreement in LV EF (Pearson correlation $r=0.95$, $p=0.49$) as well as between LA EF ($r=0.92$, $p=0.29$) (**Figure 4.3E and 4.3F**).

4.3.2 Quantitative Evaluation of DL-predicted Imaging Plane Vectors

The median displacement error Δd between Plane_{m} and Plane_{DL} was 7.0mm (IQR: 5.0,9.5) across all planes, 6.3mm (IQR: 4.3,8.5) for 2CH, 6.2mm (IQR: 4.3,8,8) for 3CH, 7.2mm (IQR: 5.5,9.6) for 4CH and 7.6mm (IQR: 5.3,11.0) for MV. The median orientation error $\Delta\theta$ between planes was 8.0° (IQR: 5.0, 11.7) across all planes, 9.5° (IQR: 6.0,13.9) for 2CH, 8.3° (IQR: 4.8,13.0) for 3CH, 7.2° (IQR: 4.6,11.2) for 4CH and 7.5° (IQR: 4.8,9.4) for MV.

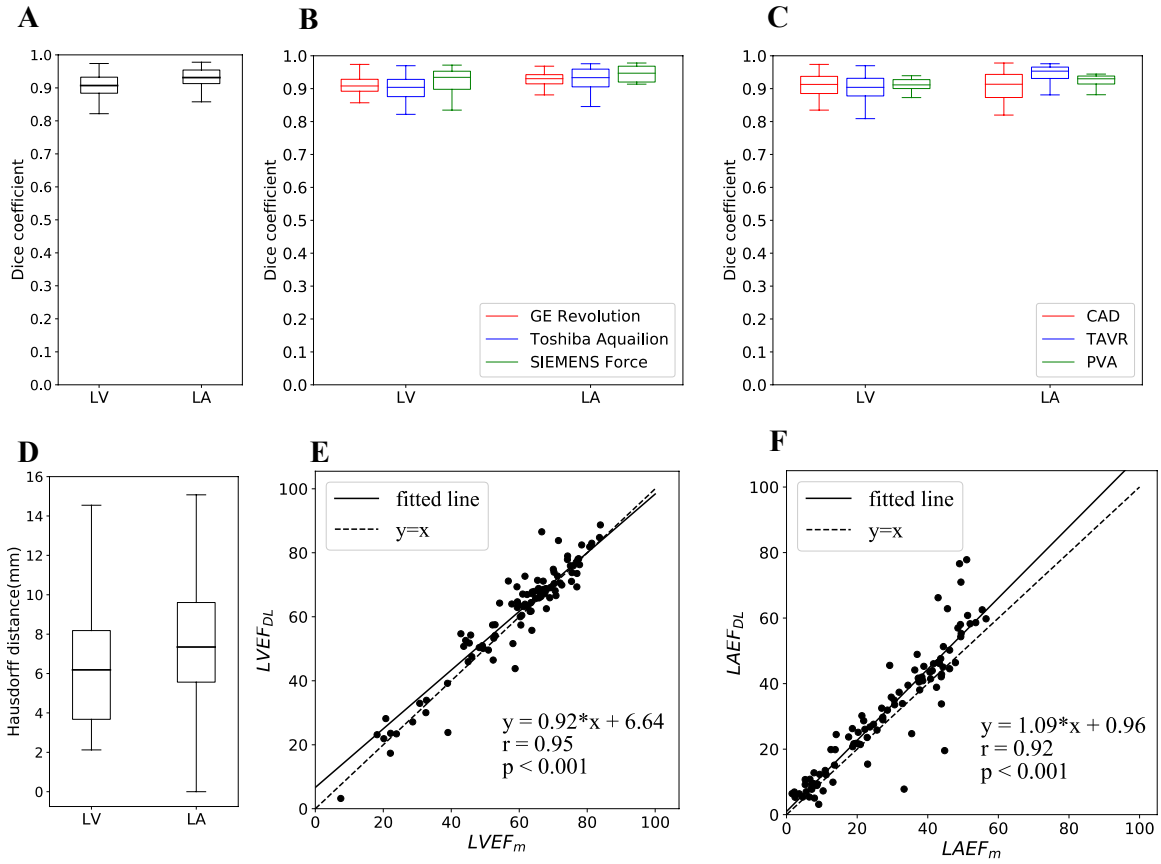

Figure 4.3. Close agreement between DL and manual chamber segmentation and function assessment. (A) Dice coefficient for two chambers of interest, the LV and LA was high. **(B)** Dice coefficient for three CT scanners. **(C)** Dice coefficient for three types of clinical indications (**D**) Hausdorff distance for LV and LA. **(E)** Correlation of LV EF derived using manual and deep-learning segmentation was close to identity (dashed) line with a fit (solid) of LV EF_{DL} = 0.92EF_m + 6.64 and Pearson correlation r = 0.95 with p <0.001. **(F)** LA EF correlation was close to identity (dashed) line with fit (solid) of LA EF_{DL} = 1.09EF_m + 0.96, and Pearson correlation r = 0.92 with p <0.001.

4.3.3 Intra and Inter-reader Differences in Imaging Plane Vectors

DL-reader orientation differences $\Delta\theta$ were not significantly different (p>0.05) compared with the corresponding inter- and intra-reader difference (**Figure 4.4, Table 4.1)**. In terms of displacement differences Δd, the 3CH and 4CH DL-reader1 difference was significantly smaller (p<0.05) than the intra-reader difference (**Figure 4.4A**).

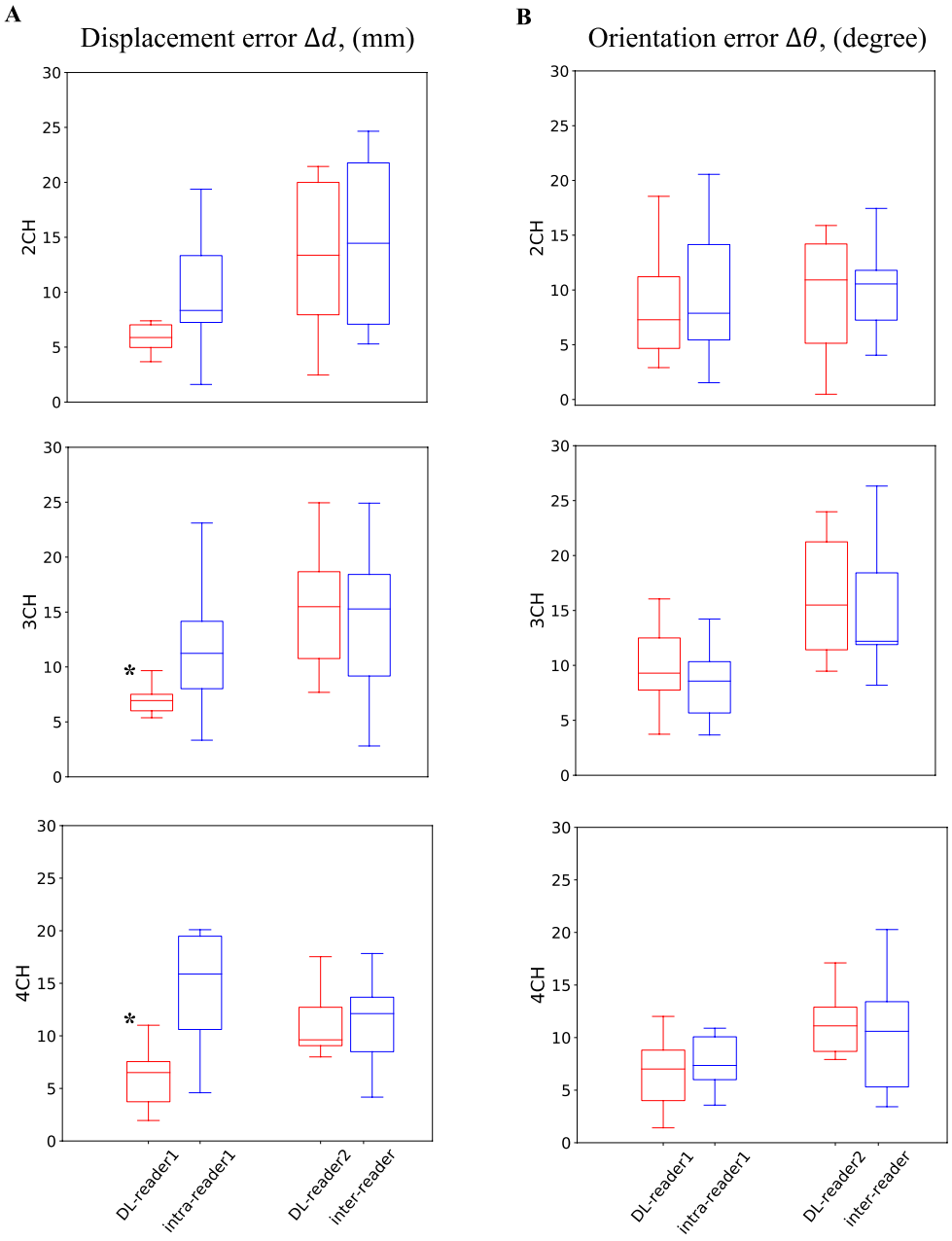

Figure 4.4. Comparison of LAX plane location and angulation differences between readers and DL. Plane displacement **(A)** and orientation **(B)** differences between DL and Reader 1 (first red boxplot) were compared to intra-Reader 1 differences (first blue boxplot) and differences between DL and Reader 2 (second red boxplot) were compared to inter-Reader differences (second blue boxplot) for each LAX plane. The asterisk (*) indicates significant differences.

Table 4.1. Comparison of LAX Plane Location and Angulation Differences between Readers and Deep Learning. Intra-reader1 differences represent variation in planes planned by the same reader six months apart. Given that the DL approach was trained on slice planning by reader 1, DL-reader 1 differences were compared to intra-reader1 differences. Inter-reader variation captures variation in slice planning by two different readers. DL-reader2 differences were compared to inter-reader values. Differences were reported as median (IQR). * indicates a significant difference ($p<0.05$). Unit for Δd is mm, unit for $\Delta\theta$ is degree.

		Intra-Reader 1 Difference	DL-Reader 1 Difference	p-value	Inter-Reader difference	DL-Reader 2 Difference	p-value
2CH	Δd	8.3 (7.3,13.3)	5.9 (5.0,7.0)	0.20	14.4 (7.1,21.8)	13.4 (7.9,20.0)	0.91
	$\Delta\theta$	7.8 (5.4,14.1)	7.3 (4.7,11.2)	0.57	10.6 (7.2,11.8)	10.9 (5.1,14.2)	0.75
3CH	Δd	11.2 (8.0, 14.2)	6.9 (6.0,7.5)*	0.04	15.3 (9.2,18.4)	15.5 (10.8,18.7)	0.76
	$\Delta\theta$	8.6 (5.7,10.3)	9.3 (7.7,12.5)	0.35	12.2 (11.9,18.4)	15.5 (11.4,21.2)	0.71
4CH	Δd	15.9 (10.6,19.5)	6.5 (3.7,7.5)*	0.003	12.1 (8.5,13.7)	9.6 (9.1,12.7)	0.84
	$\Delta\theta$	7.3 (6.0, 10.1)	7.0 (4.0,8.8)	0.35	10.6 (5.3,13.4)	11.1 (8.7,12.9)	0.82

4.3.4 Visual Assessment of Plane Quality

The deep-learning approach yielded diagnostically adequate imaging planes for a large percentage (≥94%) of cases across all slice plane locations (**Table 4.2**, representative patient shown in **Figure 4.5A)**.

4.3.5 Quantitative assessment of slice position via AHA wall assessment

The proportion of cases with correct AHA segment inclusion was not significantly different between $Plane_m$ and $Plane_{DL}$ for all AHA walls (two-sided z test, $p>0.05$) except anterior wall which had a lower likelihood of being visualized by the 2CH plane ($p=0.02$) (**Figure 4.5B, Table 4.3**).

Table 4.2. Diagnostic Adequacy of Manual and Deep-Learning Imaging Planes as Scored by Cardiothoracic Imaging Expert

	$Plane_m$	$Plane_{DL}$
2CH	100%	100%
3CH	100%	94%
4CH	100%	98%
SAX	100%	100%

Table 4.3. Assessment of AHA Wall Visualization for Manual and DL-based Cardiac Planes. Percentage of cases in which the LAX plane correctly intersects corresponding AHA wall was shown. Significant p-values are shown by asterisk.

		$Plane_m$	$Plane_{DL}$	p value
2CH	Inferior	100%	97%	0.08
	Anterior	99%	92%	0.02*
3CH	Inferolateral	84%	84%	1
	Anteroseptal	100%	97%	0.08
4CH	Inferoseptal	100%	97%	0.08
	Anterolateral	98%	97%	0.65

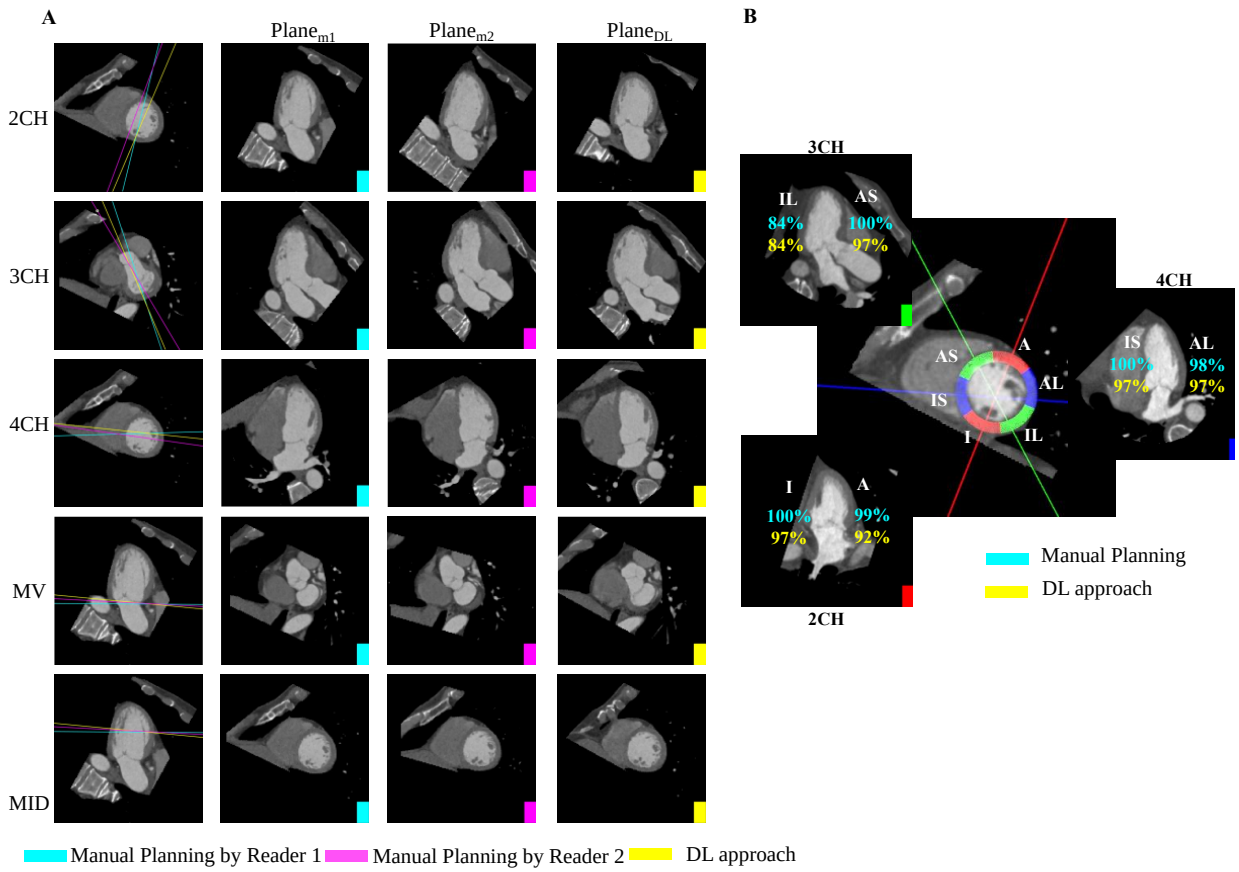

Figure 4.5. DL agrees with manual slice planning and correctly visualizes corresponding AHA segments. (A): Rows 1-3: For each long-axis imaging plane, Column 1 shows the slice location on the SAX slice (mid-ventricular slice for 2CH and 4CH and basal slice for 3CH). Columns 2-4 depict the corresponding images. Row 4-5: For the short-axis mitral valve and mid-ventricular plane, Column 1 shows the slice position of the plane on the 2CH long-axis. Columns 2 – 4 depict the short-axis images: Plane$_{m1,}$ (plane resliced by Reader 1), Plane$_{m2,}$ (plane resliced by Reader 2) and Plane$_{DL}$ (DL-derived slice). **(B)**: 6 mid-ventricular AHA segments are shown as arcs on a mid-ventricular SAX slice. The percentage of cases in which a wall was correctly intersected by the associated LAX plane are shown for the 2CH (red solid line, lower left), 3CH (green solid line, top left), and 4CH (blue solid line, right) planes. There is close agreement between the manual planes (reported in cyan) and DL (yellow). A = Anterior, I = Inferior, AS = Anteroseptal, IS = Inferoseptal, AL = Anterolateral, IL = Inferolateral.

4.3.6 Run-time for DL-based Approach

Each model was trained for 50 epochs with each epoch using approximately 170 seconds in our workstation. The time needed to predict two segmentations (ED and ES) as well as four imaging planes (2CH$_{DL}$, 3CH$_{DL}$, 4CH$_{DL}$, and MV$_{DL}$) was 29.7±4.0 seconds.

4.3.7 Assessment of the utility of DL-predicted planes on test cases

DL yielded diagnostically adequate imaging planes for a large percentage (≥99% by Reader 2 and ≥94% by Reader 3) of cases across all slice plane locations (**Table 4.4)**.

There was close agreement between visual estimation of ejection fraction by readers and quantification via automated segmentation. Specifically, linear regression demonstrated strong correlation (Spearman ρ=0.93 and 0.95 for Reader 2 and 3, respectively). In addition, classification of EF<40%, 40-50%, and >50% with the DL approach agreed with visual prediction in 88.9% and 80.5% of cases for Reader 2 and 3, respectively (**Table 4.5**).

DL-predicted planes of four test CT studies with CAD provided visualization of both regional and global LV wall motion abnormalities recorded in the radiology report (**Figure 4.6A**, see supplemental video 1 in the paper[126]). The DL model generate similar planes two CT studies of the same patient acquired as part of a longitudinal study (**Figure 4.6B,** see supplemental video 2 in the paper[126]**)**.

Table 4.4. Diagnostic Adequacy of Deep-Learning Imaging Planes in the Testing Group as Scored by Imaging Experts

	Reader 2	Reader 3
2CH	99%	99%
3CH	100%	94%
4CH	100%	95%
SAX	100%	100%

Table 4.5. The Close Agreement of Classification of EF Between Visual Estimation by Expert Readers and Automated Quantification via DL LV Segmentation. The classification of EF into <40%, 40-50%, and >50% with the DL approach agreed with visual prediction in 88.9% and 80.5% of cases for Reader 2 and 3, respectively.

		Reader 2			Reader 3		
		<40%	40~50%	>50%	<40%	40~50%	>50%
DL predict	<40%	30	3	0	31	1	1
	40~50%	0	7	4	8	2	1
	>50%	0	9	91	2	15	83

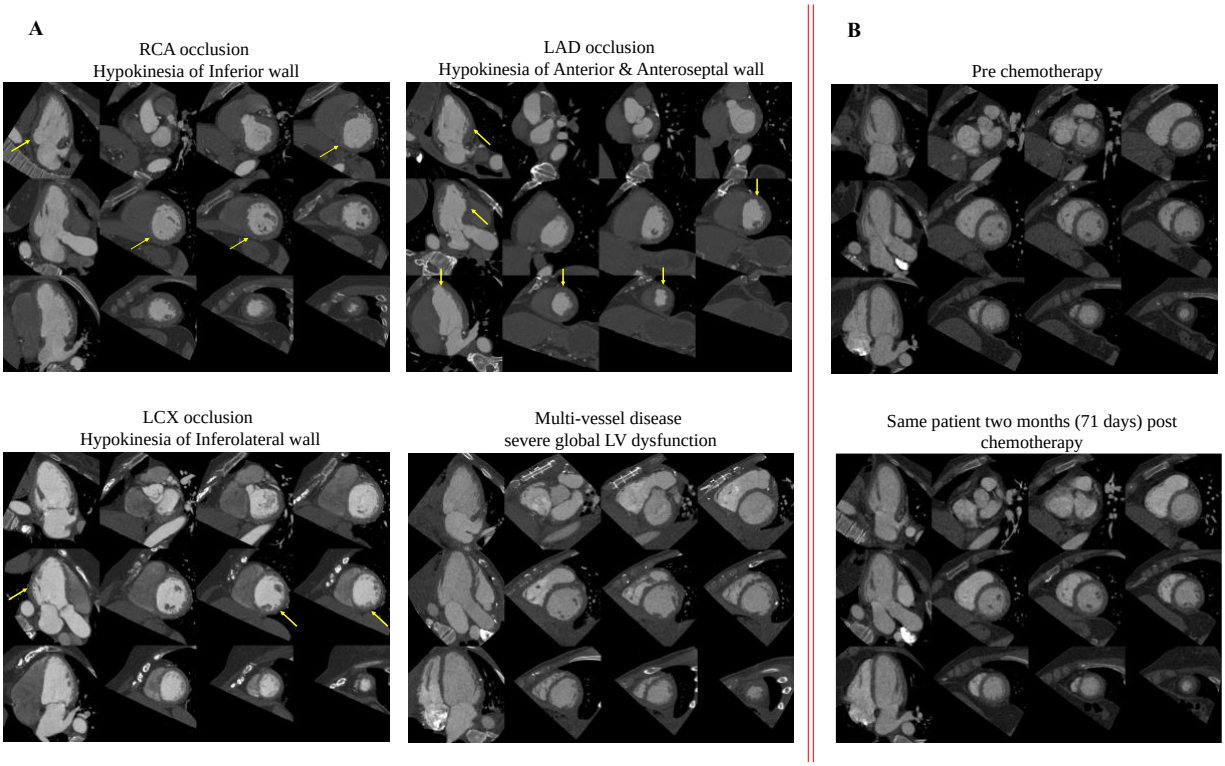

Figure 4.6. Utility of deep-learning slice planning in evaluation of regional wall motion abnormalities and longitudinal assessment of patients. (A) Four exemplar cases were selected based on radiologically observed with either global (bottom right) or regional (the rest three) LV wall motion abnormality due to CAD. Yellow arrows point out the walls with regional dysfunction where the readers can refer to in the supplemental video 1 in the paper[126]. (**B)** shows DL-predicted planes for the same patient imaged before chemotherapy and two months after the therapy which shows high reproducibility. The videos for these planes showing the cardiac function in one cardiac cycle are submitted as supplementary video 2 in the paper[126]. Window level = 500 HU, width = 900 HU.

4.4 Discussions

4.4.1 Main Findings

Cardiac chamber segmentation and cardiac imaging plane re-slicing are two important image processing steps required to do the functional analysis of cardiac CT. Currently, doing these steps manually is time consuming and leads to inter-observer variability. In this study, we developed and evaluated a DL network that automatically predicts cardiac chamber volumes as well as re-slices standardized cardiac imaging planes from volumetric CT data using a shared model architecture. The DL approach generated high quality segmentations (median Dice=0.907 and 0.931 for LV and LA, respectively) and had a strong correlation (Pearson r>0.9) with manually-derived EF. Furthermore, DL-predicted planes had low errors in spatial displacement and angulation and intersected the relevant midventricular myocardial segment in a high proportion of cases. Testing the DL network in a series of 144 consecutive cine CT cases demonstrated our approach generates diagnostically adequate imaging planes and automated segmentation leads to EF estimation that is in agreement with visual interpretation. We highlight the utility of our DL-predicted planes in the evaluation of LV wall motion abnormality and for reproducible longitudinal assessment in a sample of test cases with known pathological findings.

The main findings have been made into a graphical abstract (**Figure 4.7)** showing the high performance of both DL segmentation and plane prediction. For predicted planes, the final product of our DL framework is shown in **Figure 4.7** (a static view) as a 12-panel video of cardiac function in both LAX planes and a SAX stack. Example of the videos can be found in the supplemental materials in the paper[126].

4.4.2 Existing Approaches

In our approach, a 3D image volume (at 1.5mm isotropic voxel size) was utilized as the input for blood pool segmentation and image plane re-slicing. While a 3D approach significantly increases the memory utilization, the choice was intended to preserve volumetric context to enable accurate slicing of the long- and short-axis imaging planes. Other DL approaches for CT chamber segmentation have utilized portions of the volume as the image input; Dormer et al.[114] and Zreik et al.[115] input patches and performed patch-wise image classification while Mortazi et al.[116] and Wang et al.[117] used three orthogonal projections (axial, coronal and sagittal) as inputs. Despite the feature vector depth being limited due to memory constraints, our 3D approach led to segmentation accuracy comparable to recent work by Baskaran et al.[119] which applied a 2D U-Net to segment CT in a 2D slice-by-slice fashion and achieved Dice >0.91 for all four chambers.

The feasibility of predicting imaging planes was previously shown in 2D by Vigneault et al[183] in which a conventional U-Net was modified to predict a scaling and rotation of MRI images. Other efforts to use DL for plane prediction have focused on cardiac MRI. Le et al[184] and Blansit et al[185] recently presented DL-based cardiac MRI plane prescription by using DL to localize the anatomical landmarks that mimic how an expert performs slice planning on 2D MR. However, this is not required during CT acquisitions as they are volumetric.

4.4.3 Clinical Importance

Compared with manual annotation, our approach automatically and quickly analyzed the series of 3D CT image volumes (~30s for volumes at ED and ES). This represents a significant improvement as it usually takes a trained expert around 20 minutes to obtain volumes from two 3D image volumes at ED and ES[186] and it leads to interobserver variability. Furthermore, the

processing time of our approach can be readily improved through parallelization, as we currently predict imaging planes sequentially. While optimization of prediction time was not the focus of this study, the fast computation time increases the likelihood of clinical translation.

Robust and automated prediction of cardiac volumes and imaging planes could be used to measure multiple important clinical parameters. Apart from EF, the availability of LAX planes can enable assessment of additional measures such as contour-based global longitudinal and circumferential strain. Furthermore, labeling of other cardiac chambers or the myocardium in the training data would enable measurements such as RV volumes or myocardial masses.

Our fully automated approach may enable rapid and reproducible assessment of global function as well as regional wall motion abnormalities in patients, such as those with CAD and other cardiomyopathies who are frequently evaluated with cardiac CT. In addition, automatic slicing of standardized cardiac planes can be used for reproducible longitudinal assessment of patients undergoing serial cardiac exams and in clinical trials.

4.4.4 Limitations

Our approach has limitations. First, we observed lower performance for 3CH plane predictions relative to 2CH and 4CH planes. However, the success rate for the inferolateral wall was decreased in both $3CH_m$ and $3CH_{DL}$. This could be explained by the difficulty in planning 3CH views as there is a balance between correct visualization of the left ventricular outflow tract and the intersection of the inferolateral wall. This suggests that anatomical variability may be limiting the performance of the DL approach. Second, the time and effort needed to derive both cardiac planes and blood chamber segmentations limited our training size. However, the achieved accuracy suggests clinical utility is possible even with the limited training data that was

available. Lastly, the accuracy of the algorithm in patients with a wider range of phenotypes including implanted medical devices, significant changes in iodine contrast timing/intensity, and decreases in overall image quality was not studied but is planned for future work.

4.4.5 Conclusion

In conclusion, DL can automatically perform multi-chamber volumetric assessments and generate standardized cardiac imaging planes from CT images. This approach has the promise for regional cardiac visualization and reproducible assessment of cardiac function.

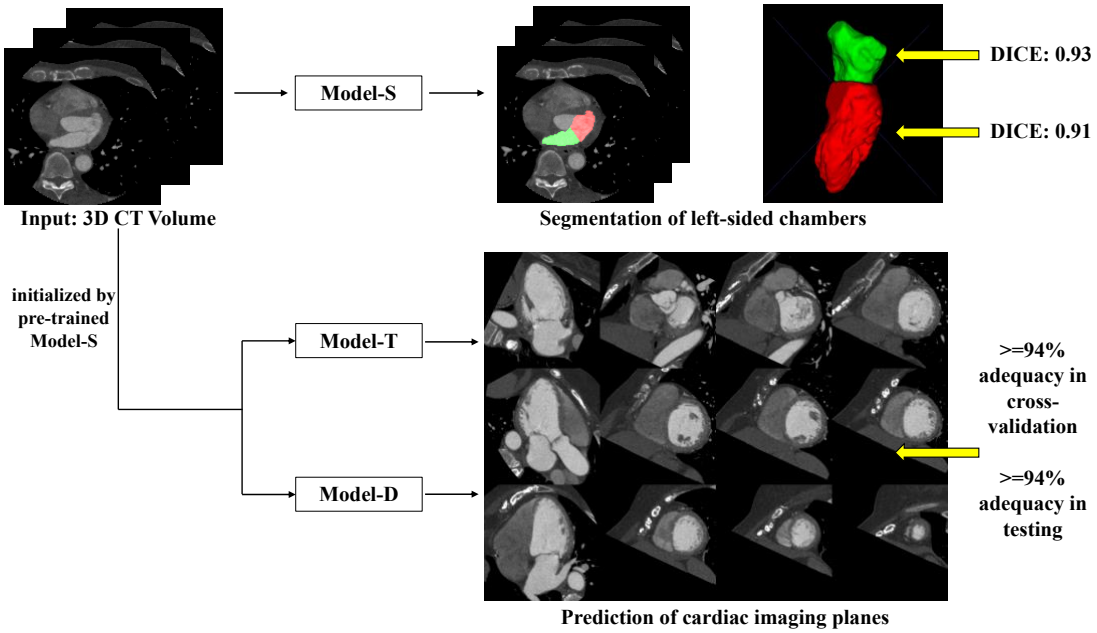

Figure 4.7. Graphical Abstract showing high performance of both segmentation and plane prediction by our DL framework.

4.5 GitHub Repository

The GitHub Repository of our DL pipeline can be found at https://github.com/ucsd-fcrl/AI_chamber_segmentation_plane_re-slicing.

4.6 Acknowledgement

Chapter 4, in full, is a reprint of the material as it appears in “Automated Cardiac Volume Assessment and Cardiac Long-and Short-Axis Imaging Plane Prediction from ECG-gated CT Volumes Enabled by Deep Learning”, Zhennong Chen, Marzia Rigolli, Davis Marc Vigneault, Seth Kligerman, Lewis Hahn, Anna Narezkina, Amanda Craine, Katherine Lowe, Francisco Contijoch, 2021. The dissertation author was a primary author of this paper.

Chapter 5: Detection of Left Ventricular Wall Motion Abnormalities from Volume Rendering of 4DCT Cardiac Angiograms Using Deep Learning

5.1 Introduction

The clinical importance of left ventricular (LV) regional wall motion abnormalities (WMA) has been stated in section 1.2 and 3.1. Cardiac 4DCT enables the assessment of LV wall motion by acquiring a series of functional images spanning the full cardiac cycle. Dynamic information of the 3D cardiac motion and regional WMA is encoded in 4DCT data. Visualization of regional WMA with CT usually requires reformatting the acquired 3D data along standard 2D short- and long-axis imaging planes. However, it requires experience in practice to resolve the precise region of 3D wall motion abnormalities from these 2D planes. Further, these 2D planes views may be confounded by through-plane motion and foreshortening artifacts[47]. We propose to directly view 3D regions of wall motion abnormalities through the use of volumetric visualization techniques such as Volume rendering (VR)[187], which can preserve high resolution anatomical information and visualize 3D[54,188] and 4D[189] data simultaneously over large regions of the LV in cardiovascular CT. In VR, the 3D CT volume is projected onto a 2D viewing plane and different colors and opacities are assigned to each voxel based on intensity. It has been shown that VR provides a highly representative and memory efficient way to depict 3D tissue structures and anatomic abnormalities[190,191]. In this study, we performed dynamic 4D volume rendering by sequentially combining the VR of each CT time frame into a video of LV function (we call this video a "Volume Rendering video"). We propose to use volume rendering videos of 4DCT data to depict 3D motion dynamics and visualize highly local wall motion dynamics to detect regional WMA.

Analytical approaches to quantify 3D motion from 4DCT using image registration and deformable LV models have been developed[86,87,192]. However, these approaches usually require complex and time-consuming steps such as user-guided image segmentation and point-to-point registration or feature tracking. Further, analysis of multiple frames at the native image resolution/size of 4DCT can lead to significant memory limitations[193]. Volume rendering (VR) videos provide a high-resolution representation of 4DCT data which clearly depicts cardiac motion at a significantly reduced memory footprint (~1 Gigabyte when using original 4DCT for motion analysis and only 100 kilobytes when using volume rendering video). Given the lack of methods currently available to analyze motion observed in VR videos, we sought to create an objective observer that could automate VR video interpretation. Doing so would facilitate clinical adoption as it would avoid the need for training individuals on VR video interpretation and the approach could be readily shared. Deep learning approaches have been successfully used to perform classification of patients using medical images[129,194]. Further, DL methods, once trained, are very inexpensive and can be easily deployed.

Therefore, in this study, we propose a novel framework which combines volume rendering videos of clinical cardiac CT cases with a DL classification to detect WMA. We outline a straightforward process to generate VR videos from 4DCT data and then utilized a combination of a convolutional neural network (CNN) and recurrent neural network (RNN) to assess regional WMA observable in the videos.

5.2 Materials and Methods

5.2.1 CT Data Collection

Under institutional review board approval, 343 ECG-gated contrast enhanced cardiac CT patient studies between Jan 2018 and Dec 2020 were retrospectively collected with waiver of informed consent. Inclusion criteria were: each study (a) had images reconstructed across the entire cardiac cycle, (b) had a field-of-view which captured the entire LV, (c) was free from significant pacing lead artifact in the LV and congenital heart disease, and (d) had a radiology report including assessment of cardiac function. Images were collected by a single, wide detector CT scanner with 256 detector rows (Revolution scanner, GE Healthcare, Chicago IL) allowing for a single heartbeat axial 16cm acquisition across the cardiac cycle. The CT studies were performed for range of clinical cardiac indications including suspected coronary artery disease (n = 153), pre-procedure assessment of pulmonary vein ablation (n = 126), preoperative assessment of transcatheter aortic valve replacement (n = 42), preoperative assessment of left ventricular assist device placement (n = 22).

5.2.2 Production of Volume Rendering Video of LV blood-pool

Figure 5.1 step 1-4 shows the pipeline of VR video production. The CT images were first rotated using visual landmarks such as the RV insertion and LV apex, so that every study had the same orientation (with the LV long axis along the z-axis of the images and the LV anterior wall at 12 o'clock in cross-sectional planes). Structures other than LV blood-pool (such as LV myocardium, ribs, the right ventricle, and great vessels) were automatically removed by a pre-trained DL segmentation U-Net[119] which has previously shown high accuracy in localizing the LV in CT images [119,126]. If present, pacing leads were removed manually.

The resultant grayscale images of the LV blood-pool (as shown in Fig. 23 step 2) were then used to produce Volume renderings (VR) via MATLAB (MathWorks, Natick MA). The LV endocardial surface shown in VR was defined by automatically setting the intensity window level (WL) equal to the mean voxel intensity in a small ROI placed at the centroid of the LV blood pool and setting the window width (WW) equal to 150HU (thus WL is study-specific, and WW is uniform for every study). We pre-set a list of rendering parameters applied across the entire dataset. Due to a uniform orientation in the dataset, a same set of camera-related parameters could be used. Concretely, "CameraPosition" was [6,0,1], "CameraUpVector" was [0,0,1], "CameraViewAngle" was 15º. A built-in colormap ("hot") and a linear alpha map (opacity vs. voxel intensity) were applied to the normalized CT image, assigning colors and opacities to each voxel according to its intensity. The background color was set to be black, and the lighting effect was turned on. Volume rendering of all frames spanning one cardiac cycle was then saved as a video ("VR video", **Figure 5.1**).

Each VR video shows the LV blood-pool from one specific projection view angle θ. Therefore, to evaluate all AHA segments, 6 VR videos were generated per study, with six different projection views $\theta_{60\times n,\ n\in[0,1,2,3,4,5]}$ corresponding to 60-degree rotations around the LV long axis. Practically, this rotation of views was done by the rotation of the camera around the z-axis of the image. We applied a rotation matrix R to the rendering parameter "CameraPosition" for each video:

$$R = \begin{bmatrix} cos(\theta) & -sin(\theta) & 0 \\ sin(\theta) & cos(\theta) & 0 \\ 0 & 0 & 1 \end{bmatrix}$$

$$\begin{bmatrix} px' \\ py' \\ pz' \end{bmatrix} = R \times \begin{bmatrix} px \\ py \\ pz \end{bmatrix} \qquad (Equation\ 5.1)$$

where [*px, py, pz*] is the pre-set "CameraPosition" equal to [6,0,1], and [*px', py', pz'*] is the derived "CameraPosition" for each rotated view. All other rendering parameters kept constant for every video.

With our design, each projection view had a particular mid-cavity AHA segment shown on the foreground (meaning this segment was the nearest to and in front of the ray source-point of rendering) as well as its corresponding basal and apical segments. Two adjacent mid-cavity AHA segments and their corresponding basal and apical segments were shown on the left and right boundary of the rendering in that view. In standard regional terminology, the six projection views (n = 0, 1, 2, 3, 4, 5 in $\theta_{60\times n}$) looked at the LV from the view with mid-cavity Anterolateral, Inferolateral, Inferior, Inferoseptal, Anteroseptal and Anterior segments on the foreground, respectively. In this paper, to simplify the text we call them six "regional LV views" from anterolateral to anterior. In total, a *large* dataset of 2058 VR videos (343 patients × 6 views) with unique projections were generated.

5.2.3 Classification of Wall Motion

Figure 5.1 steps a-d shows how the ground truth presence or absence of WMA at each location on the endocardium was determined. It is worth clarifying first that the ground truth is made on the original CT data not the volume rendered data. First, voxel-wise LV segmentations obtained using the U-Net were manually refined in ITK-SNAP (Philadelphia, PA, USA)[195]. Then, regional shortening (RS_{CT})[89,164,165] (see Chapter 3 for more research work on RS_{CT}) of the endocardium was measured using a previously-validated surface feature tracking[87] technique. The accuracy of RS_{CT} in detecting WMA has been compared to strain measured by tagged MRI[90]

(a validated non-invasive approach for detecting wall motion abnormalities in myocardial ischemia[53,158]). Regional shortening was calculated at each face on the endocardial mesh as:

$$RS_{CT} = \sqrt{\frac{Area_{ES}}{Area_{ED}}} - 1 \quad (Equation\ 5.2)$$

where $Area_{ES}$ is the area of a local surface mesh at end-systole (ES) and $Area_{ED}$ is the area of the same mesh at end-diastole (ED). ED and ES were determined based on the largest and smallest segmented LV blood-pool volumes, respectively. RS_{CT} for an endocardial surface voxel was calculated as the average RS_{CT} value of a patch of meshes directly connected with this voxel.

Per-voxel RS_{CT} values were projected to pixels in each VR video view as a quantitative map of endocardial function, which was then used to label the WMA presence/absence. The protocol of projection and labeling is followed by three steps:

Step 1. Binarize the per-voxel RS_{CT} map using a threshold RS_{CT} = -0.20, which was set empirically to separate normal and abnormal wall motion.

Step 2. Project the binarized per-voxel RS_{CT} map to the pixels in VR video. Use the MATLAB built-in function "labelvolshow" to render the *labeled* (binary) RS_{CT} map (see examples of rendered RS_{CT} map in Fig.23 step b). All rendering parameters keep the same as those for the VR video. As a result, the rendered RS_{CT} map displays the same endocardial surface as the VR video. The abnormal pixels (with color red in the map) are pixels with $RS_{CT} \geq$ -0.20 and the normal pixels (with color black in the map) are pixels with RS_{CT} < -0.20.

Step 3. Calculate the percentage of abnormal pixels = $\frac{n_{abnormal\ pixels}}{n_{abnormal\ pixels}+n_{normal\ pixels}} \times$ 100%, which shows the percentage of endocardial surface that has impaired RS_{CT}.

In our study A VR video was classified as abnormal (WMA present) if >35% of the endocardial surface shown in that video had impaired RS_{CT} ($RS_{CT} \geq -0.20$). >35% approximated that at least one of the three AHA segments in the video have abnormal wall motion.

To do per-study classification in this study, we defined that a CT study is abnormal if it has more than one VR videos labeled as abnormal ($N_{ab\_videos} \geq 2$).

Figure 5.1. Automatic Generation and Quantitative Labeling of Volume Rendering Video. This figure contains two parts: Rendering Generation. automatic generation of VR video (left column, white background, step 1-4 in red) and Data Labeling: quantitative labeling of the video (right column, light grey background, step a-d in blue). Rendering Generation: *Step 1 and 2*: Prepare the greyscale image of LV blood-pool with all other structures removed. *Step 3*: For each study, 6 volume renderings with 6 view angles rotated every 60 degrees around the long axis were generated. The mid-cavity AHA segment in the foreground was noted under each view. For example, the first image with "anterolateral" means it has mid-cavity anterolateral and its corresponding basal and apical segments in the foreground. *Step 4*: For each view angle, a volume rendering video was created to show the wall motion across one heartbeat. Five systolic frames in VR video were presented. ED = end-diastole, ES = end-systole. Data Labeling: *Step* a: LV segmentation. LV = green. *Step b*: Quantitative RS_{CT} was calculated for each voxel. *Step c*: The voxel-wise RS_{CT} map was binarized and projected onto the pixels in the VR video. See supplemental material 2 for more details. In rendered RS_{CT} map, the pixels with $RS_{CT} \geq -0.20$ (abnormal wall motion) were labeled as red and those with $RS_{CT} < -0.20$ (normal) were labeled as black. *Step d*: a video was labeled as abnormal if >35% endocardial surface has $RS_{CT} \geq -0.20$ (red pixels).

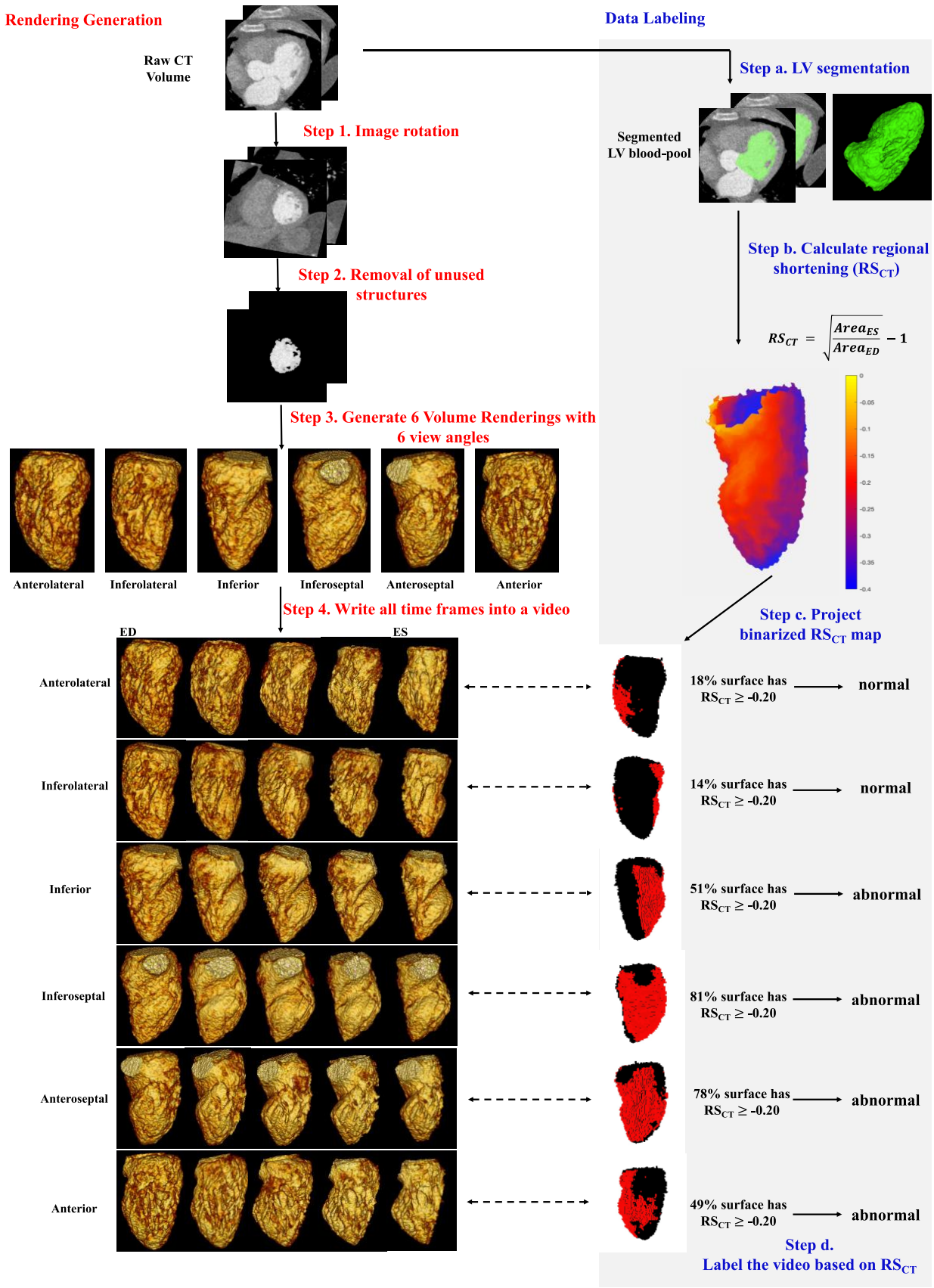
Rendering Generation
Raw CT Volume
Step 1. Image rotation
Step 2. Removal of unused structures
Step 3. Generate 6 Volume Renderings with 6 view angles
Anterolateral
Inferolateral
Inferior
Inferoseptal
Anteroseptal
Anterior
Step 4. Write all time frames into a video
ED
ES
Anterolateral
Inferolateral
Inferior
Inferoseptal
Anteroseptal
Anterior
Data Labeling
Step a. LV segmentation
Segmented LV blood-pool
Step b. Calculate regional shortening (RS_CT)
RS_CT = sqrt(Area_ES / Area_ED) − 1
Step c. Project binarized RS_CT map
18% surface has RS_CT ≥ -0.20 → normal
14% surface has RS_CT ≥ -0.20 → normal
51% surface has RS_CT ≥ -0.20 → abnormal
81% surface has RS_CT ≥ -0.20 → abnormal
78% surface has RS_CT ≥ -0.20 → abnormal
49% surface has RS_CT ≥ -0.20 → abnormal
Step d. Label the video based on RS_CT

5.2.4 DL Framework Design

The DL framework (see **Figure 5.2**) consists of three components, (*a*) a pre-trained 2D convolutional neural network (CNN) used to extract spatial features from each input frame of a VR video, (*b*) a recurrent neural network (RNN) designed to incorporate the temporal relationship between frames, and (*c*) a fully connected neural network designed to output the classification.

Given our focus on systolic function, four frames (ED, two systolic frames, and ES) were input to the DL architecture. This sampling was empirically found to maximize the performance. Given the CT gantry rotation time, this also minimizes view sharing present in image frame while providing a fuller picture of endocardial deformation. Each frame was resampled to 299×299 pixels to accommodate the input size of the pre-trained CNN.

Component (*a*) is a pre-trained CNN with the Inception architecture (Inception-v3)[196] and the weights obtained after training on the ImageNet[197] database. The reason to pick Inception-v3 architecture can be found in this reference[132]. This component was used to extract features and create a 2048-length feature vector for each input image. Feature vectors from the four frames were then concatenated into a 2D feature matrix with size = (4, 2048).

Component (*b*) is a long short-term memory[198] RNN with 2048 nodes, tanh activation and sigmoid recurrent activation. This RNN analyzed the (4, 2048) feature matrix from component (*a*) to synthesize temporal information (RNN does this by passing the knowledge learned from the previous instance in a sequence to the learning process of the current instance in that sequence then to the next instance). The final component (*c*), the fully connected layer, logistically regressed the binary prediction of the presence of WMA in the video.

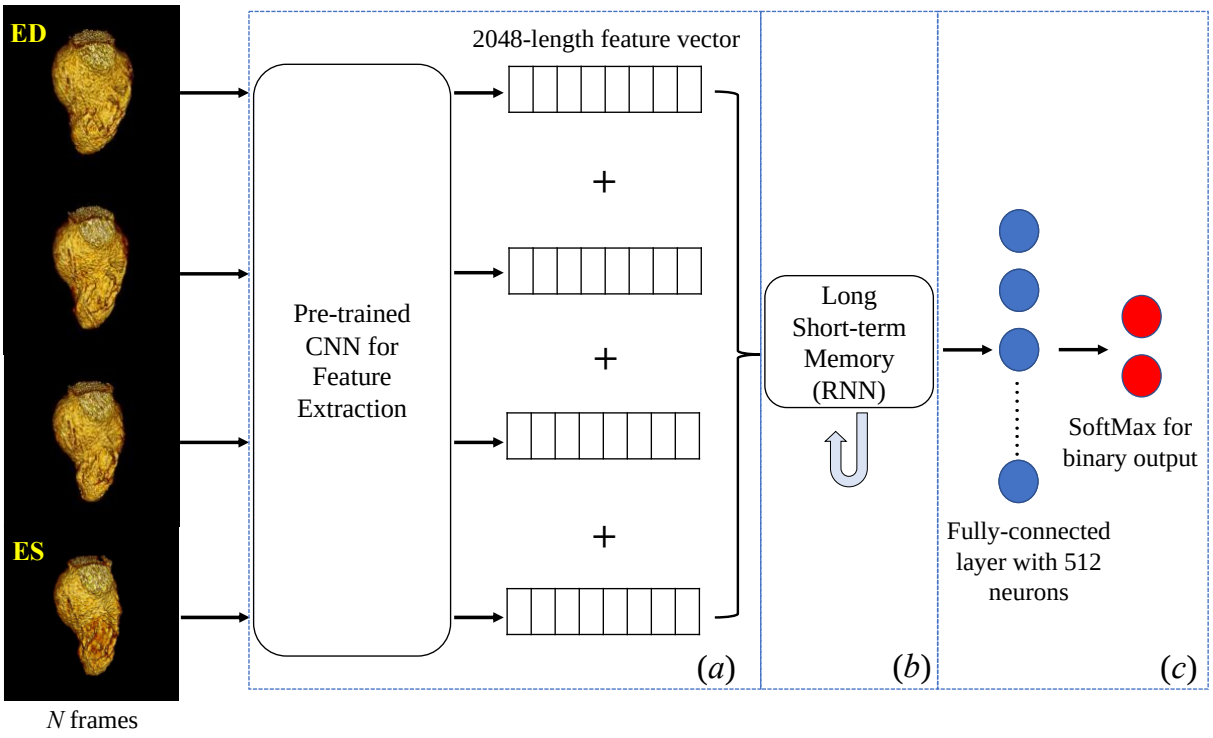

Figure 5.2. Deep Learning Framework. Four frames were input into a pre-trained inception-v3 individually to obtain a 2048-length feature vector for each frame. Four vectors were concatenated into a feature matrix which was then input to the next components in the framework. A Long Short-term Memory followed by fully connected layers was trained to predict a binary classification of the presence of WMA in the video. CNN = convolutional neural network. RNN = recurrent neural network.

5.2.5 Cross-validation and Testing

In our DL framework, component (*a*) was pre-trained and directly used for feature extraction whereas components (*b*) and (*c*) were trained end-to-end as one network for WMA classification. Parameters were initialized randomly. The loss function was categorical cross-entropy.

The dataset was split randomly into 60% and 40% subsets. 60% (205 studies, 1230 videos) were used for 5-fold cross-validation, meaning in each fold of validation we had 164 studies (984 videos) to train the model and the rest 41 studies (246 videos) to validate the model.

We report model performance across all folds. 40% (138 studies, 828 videos) were used only for testing.

5.2.6 Experiment Settings

We performed all DL experiments using TensorFlow on an 8-core Ubuntu workstation with 32 GB RAM and with a GeForce GTX 1080 Ti (NVIDIA Corporation, Santa Clara, CA, USA). The file size of each 4DCT study and VR video were recorded.

5.2.7 Model Performance and LVEF

The impact of systolic function, measured via LVEF on DL classification accuracy was evaluated in studies with LVEF <40%, LVEF between 40-60%, LVEF >60%. We hypothesized that the accuracy of the model would be different for different LVEF intervals since because the "obviously abnormal" LV with low EF, and the "obviously normal" LV with high EF would be easier to classify. The consequence of a local WMA in hearts with LVEF between 40-60% might be a more subtle pattern and harder to detect. These subtle cases are also difficult for human observers.

5.2.8 Comparison with Expert Visual Assessment

While not the primary goal of the study we investigated the consistency of the DL classifications with the results from two human observers using traditional views. 100 CT studies were randomly selected from the testing cohort for independent analysis of WMA by two cardiovascular imaging experts with different levels of experiences: expert 1 with >20 years of experience (author A.K.) and expert 2 with >5 years of experience (author H.K.N.) The experts

classified the wall motion in each AHA segment into 4 classes (normal, hypokinetic, akinetic and dyskinetic) by visualizing wall motion from standard 2D short- and long-axis imaging planes, in a blinded fashion. Because of the high variability in the inter-observer classifications of abnormal categories we: (1) combined the last three classes into a single "abnormal" class indicating WMA detection, and (2) we performed the comparison on a per-study basis. A CT study was classified as abnormal by the experts if it had more than one abnormal segment. The interobserver variability is reported in the result section 5.3.3. It should be noted that our model was only trained on ground truth based on quantitative RS_{CT} values; the expert readings were performed as a measure of consistency with clinical performance.

5.2.9 Statistical Evaluation

Two-tailed categorical z-test was used to compare data proportions (e.g., proportions of abnormal videos) in two independent cohorts: cross-validation cohort and testing cohort. Statistical significance was set at $P \leq 0.05$.

DL Model performance against the ground truth label was reported via confusion matrix and Cohen's kappa value. Both regional (per-video) and per-study comparison were performed. A CT study is defined as abnormal if it has more than one VR videos labeled as abnormal ($N_{ab\_videos} \geq 2$). As stated in section 5.2.2, every projection view of the VR video corresponded to a specific regional LV view. Therefore, we re-binned the per-video results into 6 LV views to test the accuracy of the DL model when looking at each region of the LV.

5.3 Results

Of the 1230 views (from 205 CT studies) used for 5-fold cross-validation, 732 (from 122 studies, 59.5%) were male (age: 63±15) and 498 (from 83 studies, 40.5%) were female (age: 62±15). The LV blood pool had a median intensity of 516 HU (IQR: 433 to 604). 40.0% (492/1230) of the videos were labeled as abnormal based on RS_{CT} analysis, and 45.4% (93/205) of studies had WMA in ≥2 videos. 104 studies had LVEF > 60%, 54 studies had LVEF < 40% and the rest 47 (47/205 = 22.9%) studies had LVEF between 40-60%.

Of the 828 views (from 138 CT studies) used for testing, 504 (from 84 studies, 60.9%) were male (age: 57±16) and 324 (from 54 studies, 39.1%) were female (age: 63±13). The LV blood pool had a median intensity of 520 HU (IQR: 442 to 629). 37.0% (306/828) of the videos were labeled as abnormal, and 45.0% (62/138) of studies had WMA in ≥2 videos. 72 studies had LVEF > 60%, 25 studies had LVEF < 40% and the rest 41 (41/138 = 28.7%) studies had LVEF between 40-60%.

There were no significant differences (all P values > 0.05) in data proportions between the cross-validation and testing cohorts in terms of the percentages of sex, abnormal videos, abnormal CT studies.

5.3.1 Model Performance – Per-video and Per-study Classification

Per-video and per-study DL classification performance for WMA were excellent in both cross-fold validation and testing. **Table 5.1** shows that the per-video classification for the cross-validation had high accuracy = 93.1%, sensitivity = 90.0% and specificity = 95.1%, Cohen's kappa κ = 0.86 with 95% CI as [0.83,0.89]. Per-study classification also had excellent

performance with accuracy = 93.7%, sensitivity = 93.5% and specificity = 93.8%, κ = 0.87[0.81,0.94].

Table 5.1 also shows that the per-video classification for the testing cohort had high accuracy = 90.9%, sensitivity = 90.2% and specificity = 91.4%, κ = 0.81[0.77,0.85]. With $N_{ab\_videos} \geq 2$, we obtained per-study classification accuracy = 93.5%, sensitivity = 91.9% and specificity = 94.7%, κ = 0.87[0.78,0.95].

Figure 5.3 shows the relationship between DL classification accuracy and LVEF in the cross-validation. **Table 5.2** shows that CT studies with LVEF between 40 and 60% in the cross-validation cohort were classified with per-video accuracy = 78.7%, sensitivity = 78.0% and specificity = 79.8%. In the testing cohort, per-video classification accuracy = 80.1%, sensitivity = 82.9% and specificity = 75.5% accuracy for this LVEF group remained relatively high but was lower ($P < 0.05$) than the accuracy for patients with LVEF < 40% and LVEF > 60% due to the more difficult nature of the classification task in this group with more "subtle" wall motion abnormalities.

5.3.2 Model Performance – Regional LV views

Table 5.3 shows that our DL model was accurate for detection of WMA in all 6 regional LV views both in cross-validation cohort (mean accuracy $=93.1\% \pm 0.03$) and testing cohort (mean accuracy$=90.9\% \pm 0.06$).

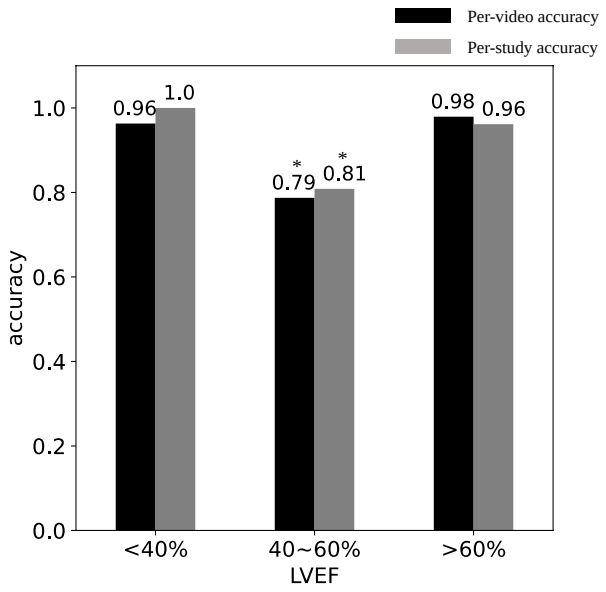

Figure 5.3. DL classification accuracy vs. LVEF. The per-video (black) and per-study (grey) accuracy are shown in studies with (LVEF<40%), (40≤LVEF ≤60%) and (LVEF>60%). * indicates the significant difference

5.3.3 Model Performance – Comparison with Expert Assessment

First, we report the interobserver variability of two experts. The Cohen's kappa for the agreement between observers on per-AHA-segment basis was 0.81[0.79,0.83] and on the per-CT-study basis was 0.88[0.83,0.93]. For those segments labeled as abnormal by both experts, the Kappa for the two experts to further classify an abnormal segment into hypokinetic, akinetic and dyskinetic dramatically dropped to 0.34.

Second, we show in the **Table 5.4** that per-study comparison between DL prediction and expert visual assessment on 100 CT studies in the testing cohort led to Cohen's Kappa κ = 0.81[0.70,0.93] for expert 1 and κ = 0.73[0.59,0.87] for expert 2.

5.3.4 Data-size Reduction

The average size of the CT study across one cardiac cycle was 1.52±0.67 Gigabytes. One VR video was 341±70 Kilobytes, resulting in 2.00±0.40 Megabytes for 6 videos per study. VR videos led to a data size that is ~800 times smaller than the conventional 4DCT study.

Table 5.1. DL Classification Performance in Cross-validation and Testing. 205 CT studies and 1230 Volume Rendered (VR) videos were used for 5-fold cross-validation. 138 CT studies and 828 VR videos were in the testing. The four confusion matrices correspond to per-video classification (light gray) and per-study classification (dark gray) for cross-validation (left) and testing (right). $N_{ab\_videos} \geq 2$ (number of views classified as abnormal) was used to classify a study as abnormal. Sens = sensitivity, Spec = specificity, Acc = accuracy. Cohen's kappa κ is also reported.

		Cross-Validation				Testing			
		Per-video		Per-study ($N_{ab\_videos} \geq 2$)		Per-video		Per-study ($N_{ab\_videos} \geq 2$)	
		Ground Truth		Ground Truth		Ground Truth		Ground Truth	
		Abnormal	Normal	Abnormal	Normal	Abnormal	Normal	Abnormal	Normal
DL	Abnormal	443	36	87	7	276	45	57	4
	Normal	49	702	6	105	30	477	5	72
		Sens	0.900	Sens	0.935	Sens	0.902	Sens	0.919
		Spec	0.951	Spec	0.938	Spec	0.914	Spec	0.947
		Acc	0.931	Acc	0.937	Acc	0.909	Acc	0.935
		κ	0.855	κ	0.872	κ	0.808	κ	0.868

Table 5.2. DL Classification Performance in CT studies with 40 < LVEF <60%. 47 CT studies with 40%<LVEF<60% were in the cross-validation and 41 CT studies were in the testing.

		Cross-validation				Testing			
		Per-video		Per-study ($N_{ab\_videos} \geq 2$)		Per-video		Per-study ($N_{ab\_videos} \geq 2$)	
		Ground Truth		Ground Truth		Ground Truth		Ground Truth	
		Abnormal	Normal	Abnormal	Normal	Abnormal	Normal	Abnormal	Normal
DL	Abnormal	131	23	33	5	126	23	32	3
	Normal	37	91	4	5	26	71	1	5
		Sens	0.780	Sens	0.892	Sens	0.829	Sens	0.970
		Spec	0.798	Spec	0.500	Spec	0.755	Spec	0.625
		Acc	0.787	Acc	0.809	Acc	0.801	Acc	0.902

Table 5.3. Results re-binned into Six Projection Views. This table shows the per-video classification of our DL model when detecting WMA from each regional view of LV. See the definition of regional LV views in section 5.2.2. Sens = sensitivity, Spec = specificity, Acc = accuracy

		Per-video Classification					
		Cross-validation			Testing		
Projection View θ	Regional LV view	Sens	Spec	Acc	Sens	Spec	Acc
0	Anterolateral	0.845	0.964	0.922	0.886	0.936	0.920
60	Inferolateral	0.938	0.952	0.946	0.909	0.915	0.913
120	Inferior	0.879	0.974	0.932	0.917	0.910	0.913
180	Inferoseptal	0.882	0.946	0.917	0.847	0.861	0.855
240	Anteroseptal	0.963	0.944	0.951	0.927	0.952	0.942
300	Anterior	0.893	0.931	0.917	0.932	0.904	0.913

Table 5.4. Comparison between DL and Expert Visual Assessment. Per-study comparison were run on 100 CT studies randomly selected from the testing cohort.

		Expert Visual Assessment			
		Expert 1		Expert 2	
		Abnormal	Normal	Abnormal	Normal
DL	Abnormal	37	5	33	9
	Normal	4	54	4	54
		κ	0.815	κ	0.729

5.4 Discussion

5.4.1 Main Findings

In this study, we developed and evaluated a DL framework that detects the presence of WMA in dynamic 4D volume rendering (VR videos) depicting the motion of the LV endocardial boundary. VR videos enabled a highly compressed (in terms of memory usage) representation of large regional fields of view with preserved high spatial-resolution features in clinical 4DCT data. Our framework analyzed four frames spanning systole extracted from the VR video and achieved high per-video (regional LV view) and per-study accuracy, sensitivity and specificity ($\geq$0.90) and concordance ($\kappa \geq$0.8) both in cross-validation and testing. By re-binning per-video results into the 6 regional views of the LV we showed DL was accurate (mean accuracy = 92.0%) for every region. DL classification strongly agreed (accuracy = 91.0%, κ: 0.81) with expert visual assessment.

5.4.2 Benefits of the Volume Visualization Approach

Assessment of regional WMA with CT is usually performed on 2D imaging planes reformatted from the 3D volume. However, 2D approaches often confuse the longitudinal bulk displacement of tissue into and out of the short-axis plane with true myocardial contraction.

Various 3D analytical approaches[86,89,192] to quantify 3D motion using image registration and deformable LV models have been developed; our novel use of regional VR videos as input to DL networks has several benefits when compared to these traditional methods. First, VR videos contain 3D endocardial surface motion features which are visually apparent. This enables simultaneous observation of the complex 3D motion of a large region of the LV in a single VR video instead of requiring synthesis of multiple 2D slices. Second, our framework is extremely memory efficient with reduced data size while preserving key anatomical and motion information; a set of 6 VR videos is ~800 times smaller in data size than the original 4DCT data. The use of VR videos also allows our DL experiments to run on the current graphic processing unit (GPU), whereas the original 4DCT data is too large to be imported into the GPU. Third, our framework is simple as it does not require complex and time-consuming computations such as point registration or motion field estimation included in analytical approaches. The efficiency of our technique will enable retrospective analysis of large numbers of functional cardiac CT studies; this cannot be said for traditional 3D tracking methods which require significant resources and time for segmentation and analysis.

5.4.3 Model Performance for each LV view

We re-binned the per-video results into 6 projection views corresponding to 6 regional LV views and showed that our DL model is accurate to detect WMA from specific regions of the LV. The results shown in **Table 5.3** indicate that all results for classification can be labeled with a particular LV region. For example, to evaluate the wall motion on the inferior wall of a CT study, the classification from the VR video with the corresponding projection view θ (=120) would be used.

5.4.4 Concerns about Expert Comparison Study

To evaluate the consistency of our model with standard clinical evaluation, we compared DL results with two cardiovascular imaging experts and showed high per-study classification correspondence. This comparison study has its limitations. First, we did not perform a per-AHA-segment comparison. Expert visual assessment was subjective (by definition) and had greater inter-observer variability on per-AHA-segment basis than the per-study basis the variability (Kappa increased from 0.81 for per-segment to 0.88 for per-study). Second, the interobserver agreement for experts to further classify an abnormal motion as hypokinetic, akinetic or dyskinetic was also too poor (Kappa = 0.34) to use expert visual labels for three severities as the ground truth; therefore, we used one "abnormal" class instead of three levels of severity of WMA. Third, experts could only visualize the wall motion from 2D imaging planes while our DL model evaluated the 3D wall motion from VR videos. A future study using a larger number of observers, and a larger number of cases could be performed in which trends could be observed; however, it is clear that variability in subjective calls for degree of WMA will likely persist in the expert readers.

5.4.5 Limitations

There are limitations in our work. First, direct visualization of wall motion abnormalities in volume rendered movies from 4DCT is a truly original application; hence, as can be expected there are no current clinical standards/guidelines for visual detection of WMA from volume rendered movies. In fact, we believe our study is the first to introduce this method of evaluating myocardial function in a formal pipeline. In our recent experience, visual detection of patches of

endocardial "stasis" in these 3D movies highly correlates with traditional markers of WMA such as wall thickening, circumferential shortening and longitudinal shortening. However, guidance on how to clinically interpret VR movies is not yet available. We expect human interpretation to depend on both experience and training. Thus, we used previously validated quantitative myocardial shortening (RS_{CT}) derived from 3D tracking to delineate regions of endocardial WMA. RS_{CT} has been previously shown to be a robust method for quantifying function[89,90,164,165]. In addition, the large number of subjects included for DL training required a fast and highly automated method for evaluating quantitative function. Second, tuning the inceptionV3 (the CNN) weights to extract features most relevant to detection of WMA is expected to further increase performance as it would further optimize how the images are analyzed. However, given our limited training data, we chose not to train weights of the inception network and the high performance we observed seems to have supported this choice. Last, as stated above, we currently perform binary classification of the presence of WMA in a large region; specifically, VR views enable broad assessment of WMA in particular walls. Future research with larger numbers of studies will aim to estimate the boundary of the WMA regions with spatial resolution equivalent to AHA segments, as well as estimate the severity of the WMA.

5.4.6 Conclusion

In conclusion, we developed a framework that combines the video of the volume rendered LV endocardial blood pool with deep learning classification to detect WMA and observed high per-region (per-video) and per-study accuracy. This approach has promising

clinical utility to screen for cases with WMA simply and accurately from highly compressed data.

5.5 GitHub Repository

The GitHub Repository of our DL technique can be found at https://github.com/ucsd-fcrl/DL_WMA_by_VR_Final_v_ZC.

5.6 Acknowledgement

Chapter 5, in part, is a reprint of the material as it appears in "Development of Deep Learning Pipeline for Direct Observation of Wall Motion Abnormality from 4DCT", Zhennong Chen, Francisco Contijoch, Elliot McVeigh, 2022. The dissertation author was a primary author of this paper.

Chapter 5, in part, has been submitted for publication of the material as it may appear in "Detection of LV Wall Motion Abnormalities from Volume Rendering of 4DCT Cardiac angiograms Using Deep Learning", Zhennong Chen, Francisco Contijoch, Gabrielle M. Colvert, Ashish Manohar, Andrew M. Kahn, Hari Narayan, Elliot McVeigh, 2022. The dissertation author was a primary author of this paper.

Chapter 6: Conclusions and Future Directions

6.1 Contributions

Recent developments in 4D CT allows the evaluation of both coronary artery disease and myocardial function. This dissertation introduces novel analytical-based and deep learning-based techniques to analyze coronary stenosis and myocardial dysfunction from CT. These techniques have remarkable promise to replace existing manual work and lead to automatic, fast, and accurate diagnosis of cardiovascular disease.

In **Chapter 2**, we introduced a novel quantification algorithm to tackle the challenge of accurately quantifying the coronary stenosis with sizes on the order of or below the image resolution. We first demonstrated two important observations: (1) traditional full-width-at-half-maximum (FWHM) can only accurately measure the diameter of larger vessels (above the image resolution) ; the FWHM significantly overestimates the diameter of small vessels; (2) intraluminal maximum CT number reduces rapidly with decreasing vessel diameter for smaller vessels and small diameter stenoses. We then derived a mathematical explanation of this CT number reduction (**Equation 2.2**) and plotted the relationship between intraluminal maximum CT number vs. vessel diameter as a *CT-number calibration curve* (**Figure 2.4**). One important discovery we made is that the calibration curve is dependent on the point-spread-function (PSF) of the CT image. Therefore, we should make an individual calibration curve for each imaging acquisition setting with unique PSF. The final product of this study we developed is a new quantification algorithm (called "CT-number-Calibrated diameter") that utilizes FWHM to measure vessels above a critical diameter related to the image resolution and the calibration curve to measure vessels below the critical diameter. We validated this algorithm using a

stenosis phantom showing only ≈5% error from ground truth stenosis diameter. Looking into the future, we believe our algorithm will have great clinical importance to achieve accurate quantification of severe stenoses and thus estimates of the anatomical significance of stenoses. Further, incorporating our algorithm into the FFR_{CT} pipeline may have a positive impact on the accuracy of FFR_{CT} (functional significance of stenoses).

In **Chapter 3**, we turned our focus to the evaluation of impaired myocardial function via 4DCT. Subjective evaluation from clinicians leads to interobserver variability and can only provide a qualitative assessment. The overarching purpose of this research is to investigate the effectiveness of a developed quantitative metric (RS_{CT}) as an objective decision classifier to detect the presence of segmental LV wall motion abnormality (WMA) from 4DCT. RS_{CT} is the myocardial regional shortening measured via 4DCT using a validated surface feature tracking algorithm[87]. We showed that RS_{CT} is an outstanding decision classifier to detect WMA (AUC = 0.991). A defined optimal threshold of RS_{CT} (RS_{CT}* =-0.20) was defined to maximize the summation of detection sensitivity and specificity. Using this threshold, we achieved high detection performance in all 16 AHA segments when compared with expert visual detection both in the method development (training) cohort and in an independent validation cohort. Driven by the heterogeneity of wall motion in different AHA segments, we evaluated whether using varied AHA-segment-specific thresholds ($RS_{CT,AHA}$*) can improve the performance. We showed that $RS_{CT,AHA}$* took on values in a small interval from -0.16 to -0.23 with relatively low value in the basal segments. Using $RS_{CT,AHA}$* slightly improves the detection sensitivity in the validation cohort (from 0.89 to 0.94) but requires a further dedicated study to increase the number of samples in each AHA segment. Overall, we accomplished our purpose and proved that the

quantitative metric RS_{CT} with optimal threshold = -0.20 is an outstanding decision classifier to detect segmental WMA from 4DCT.

In **Chapter 4**, we utilized deep learning to solve an unmet need in image processing required for myocardial function analysis. First, *quantitative* assessment of myocardial function requires accurate heart chamber segmentation. It often requires manual annotation of the images, which is time-consuming and highly dependent on the user's training and experience. Second, as images are acquired volumetrically, visualization of wall motion abnormalities requires re-slicing the volume data along standard cardiac imaging planes. Currently, this requires specialized viewing software and manual processing which may lead to inter-reader variability, limiting clinical use. Thus, the unmet need is a fully automatic technique to accomplish these two image processing tasks. To fulfill this need, we developed a DL framework to perform multi-chamber segmentation and cardiac imaging plane prediction automatically and simultaneously. DL segmentation showed close agreement with manual LV (Dice = 0.91) and LA (Dice = 0.93) segmentations and a strong correlation with manual ejection fraction (Pearson r = 0.95). DL predicted planes had low localization and angular orientation errors, and more importantly, ≥94% of the reformatted planes were assessed to be diagnostically adequate by two imaging experts. The final product of our DL framework contains (1) accurate chamber segmentations for CT volumes and (2) adequate visualization of myocardial function from a movie of three LAX planes and a SAX stack (see **Figure 4.7**). We recorded that the time to make the reformatted movies in one 4DCT dataset is below 30 seconds, which is dramatically shorter than the time required for manual annotations (usually 15-20 minutes per 4DCT case). We believe our DL framework is capable to replace manual image processing required in routine research and clinics and provides automatic, reproducible and accurate segmentation and planes.

In **Chapter 5**, we made a novel breakthrough in deep learning-driven myocardial function analysis in 4DCT. Myocardial function analysis in 4DCT was an unsolved problem for deep learning due to two primary difficulties: (1) the complexity of 3D LV wall motion and (2) the massive data size of 4DCT which cannot fit into current GPUs. To solve this problem, we turned our attention to a modern computer vision technique: dynamic volume rendering (VR). Dynamic VR has circumvents the primary difficulties. First, the complicated 3D wall motion can be clearly visualized from the dynamic VR, thus it should be easier for the DL model to detect wall motion abnormality by learning the obvious image features of VR. Second, VR is very efficient in data memory usage (only few megabytes) to represent the large 4DCT dataset (usually gigabytes). The compressed data size enables the DL experiments to fit into current GPU memory. Empowered by dynamic VR, we invented the *first* DL framework to accurately detect regional LV WMA from high-resolution 4DCT[133]. Concretely, the raw 4DCT images are input into our framework to first generate a set of 6 videos of dynamic volume-rendered LV automatically, corresponding to the LV endocardial wall visualized from 6 regional LV views. Then, a CNN+RNN DL model takes the video as the input and outputs a binary classification of the presence of WMA in the LV wall shown in that video. We showed our technique achieved both high per-region and per-study classification performance in both a large cross-validation cohort and an independent testing cohort. Apart from the benefits of using VR, this DL technique is simple and fast (prediction is made in <1 second) as it does not require complex and time-consuming computations included in traditional analytical approaches. The efficiency of our technique will enable retrospective screening for studies with WMA from large functional cardiac CT datasets.

6.2 Future Directions and Outlook

In this dissertation we introduced innovative analytical-based and DL-based techniques to analyze coronary stenosis and myocardial function via CT. Despite their remarkable promise, there remains more work to do before implementing them into routine clinical use.

For coronary stenosis quantification, the main challenge of testing our "CT-number-Calibrated Diameter" technique on the clinical patient study is how to define the "true" stenosis diameter. Invasive imaging modalities such as optical coherence tomography (OCT) and intravascular ultrasound (IVUS) provide *in vivo* measurement of stenosis diameter, but they suffer from their own limitations. Several studies have shown that OCT has smaller measurement than IVUS for the same stenosis[199–201], and the correlation between FFR and parameters (e.g., minimal luminal diameter) derived from both OCT[200,202] and IVUS[200] is poor. One potential direction we can follow: instead of comparing the vessel dimension directly, we could compare the ground truth functional significance of a stenosis (invasive FFR) with the functional significance derived from FFR_{CT}[66,81] technique that simulate the blood flows using a vessel diameter map adjusted/corrected by our "CT-number-calibrated diameter". Our vision is that with enhanced accuracy of stenosis quantification for all range of vessel sizes, "CT-number-calibrated diameter" will generate a more accurate vessel diameter map and thus more accurate FFR_{CT} measurements, avoiding patients from suffering from unnecessary invasive treatments. Furthermore, the impacts of coronary calcification and the per-patient variability in fat and soft tissue attenuation need to be further evaluated.

For myocardial function analysis, our ultimate goal is to accurately quantify the regional three-dimensional myocardial strain that help clinicians understand the 3D complicated wall motion across the entire myocardium and better guide the diagnosis and treatment such as CRT

pacing lead implantation[167] and LV arrhythmia ablation. Driven by this goal we have developed the technique to quantify RS_{CT} and showed the effectiveness of RS_{CT} to be an outstanding objective classifier to detect regional LV wall motion abnormality. The detection performance is comparable with a trained imaging expert. One missing piece in the current RS_{CT} pipeline is that it only measures the deformation on the endocardium but not the epicardium while a clinician evaluates both endo- and epicardium in the diagnosis. Thus, the measurement of wall thickness change or epicardial strain can be integrated with RS_{CT} to make the analysis more consistent with clinical standard.

Currently, the RS_{CT} pipeline requires the accurate manual segmentation of the entire LV blood-pool (usually done in ITK-SNAP) that is time-consuming and user dependent, therefore its clinical utility is unfortunately limited. In **Chapter 4** we described our solution: deep learning segmentation. A trained DL model can generate the pixel-wise segmentation of multiple heart chambers for a 4DCT dataset in few seconds. There has been commercial software (e.g., Terarecon, Simpleware) in the market to provide DL segmentation services. However, DL segmentation still has room for improvement. First, we have observed in our experiments that DL performance dramatically decreases in CT images with lead artifacts. The existence of metal changes the attenuation of local tissues. The clear attenuation boundary between high-attenuation blood-pool and low-attenuation myocardium no longer exists when the lead artifacts overlap these regions, therefore it's much harder for the DL model to capture the correct boundary. Potential solutions are to incorporate a metal artifact reduction algorithm[101,102,203] as the image preprocessing or to develop an end-to-end DL model that removes the artifacts and returns the accurate segmentation in one model. Second, researchers will have data memory concerns when running the DL segmentation on their *local* GPU station. One value of CT is its high spatial

resolution, but the entire high-resolution CT volume cannot be fitted into most of the current GPUs. The researchers have to choose from two options which both have their limitations. First, they can use a 2D DL model (using 2D CT slices as the model input) which does the segmentation in a slice-by-slice fashion, but this approach suffers from the inconsistent performance across different slices (e.g., DL usually returned a jagged surface for valve planes based on our experience). Second, they can use a 3D DL model (using 3D CT volume as the input) which generates more smooth and consistent segmentation across slices due to the knowledge of global context, but this approach can only take the down-sampled CT volume (e.g., pixel dimension down-sampled to 1.5mm in our study in Chapter 4) as the input and generate low-resolution segmentation with the loss of the high-resolution features. Approaches that both reduce the data memory and maintain the high-resolution features are needed. For example, the recent work of Octree representation by Gupta et al.[193] provides a promising DL solution to represent the CT volume used for DL with significantly reduced data memory (87.5% reduction) while maintaining the high segmentation fidelity (LV Dice = 0.97). Cheaper cloud computing services with powerful GPU ability should also be more easily available to researchers. Third, a major limitation of the DL approach is the need for a large volume of training data that captures the full spectrum of inputs (e.g., patients with various kinds of diseases) to ensure the generalizability when dealing with heterogeneous clinical data. Unfortunately, the current DL models are often trained on single-institution datasets and suffer from poor performance when transferred to other institutions (with different vendors, protocols or patient populations)[204]. Federated learning[204,205] is a hopeful direction for multi-institutional deep learning that does not require the assembly of the real data from different centers and thus avoid the consequential ethical and legal challenges.

Apart from the requirement of manual segmentation, current 3D regional myocardial function analyses also suffer from complex inverse problems and expensive computation cost. For instance, RS_{CT} measurement requires the 3D point-to-point registration which takes around 10 minutes per 4DCT case to run locally in the Mac laptop. Large data sizes of 4DCT also requires the use of external hard drive. Our invention of the first DL technique (DL + volume rendering) to detect LV WMA successfully solved the problem (see benefits of our technique in section 5.4.2). A trained DL framework can be easily deployed (in any system with a compatible GPU) and generate predictions in <1 second. Volume rendering videos also dramatically decrease the required data memory. We plan to keep improving this technique in four directions. First, the prototype of this DL framework can only predict a binary classification of the presence of WMA in the video (this is a *video classification* problem) while we envision that the next generation should be able to delineate the boundary of WMA in the video (this is a *video object detection* problem) and predict the severity of WMA into one of hypokinetic, akinetic and dyskinetic. Second, a much larger volume of training data should be prepared. Especially, we hypothesize that by preparing more borderline CT studies with LVEF from 40~60% for the training, the DL can increase its performance in these challenging studies. Third, there are many medical image visualization software packages such as OsiriX that provide high-quality volume rendering visualization. A very practical use of our technique is to embed our technique into the existing volume rendering feature in the software so that the user can obtain both the volume rendering and WMA indication simultaneously. Fourth, currently the generation of dynamic volume rendering and the prediction of WMA are two separate sequential steps in our pipeline, but it is possible to design one DL framework to accomplish two things at the same time. State-

of-art DL-driven volume rendering technology[206] directly outputs the volume rendering from the input object, and we may add the WMA detection feature by using its latent space.

References

1. Virani SS, Alonso A, Aparicio HJ, Benjamin EJ, Bittencourt MS, Callaway CW, Carson AP, Chamberlain AM, Cheng S, Delling FN, Elkind MSV, Evenson KR, Ferguson JF, Gupta DK, Khan SS, Kissela BM, Knutson KL, Lee CD, Lewis TT, Liu J, Loop MS, Lutsey PL, Ma J, Mackey J, Martin SS, Matchar DB, Mussolino ME, Navaneethan SD, Perak AM, Roth GA, Samad Z, Satou GM, Schroeder EB, Shah SH, Shay CM, Stokes A, VanWagner LB, Wang NY, Tsao CW, null null. Heart Disease and Stroke Statistics—2021 Update. *Circulation*. 2021;143(8):e254-e743. doi:10.1161/CIR.0000000000000950

2. Timmis A, Townsend N, Gale CP, Torbica A, Lettino M, Petersen SE, Mossialos EA, Maggioni AP, Kazakiewicz D, May HT, De Smedt D, Flather M, Zuhlke L, Beltrame JF, Huculeci R, Tavazzi L, Hindricks G, Bax J, Casadei B, Achenbach S, Wright L, Vardas P, European Society of Cardiology. European Society of Cardiology: Cardiovascular Disease Statistics 2019. *European Heart Journal*. 2020;41(1):12-85. doi:10.1093/eurheartj/ehz859

3. GBD 2013 Mortality and Causes of Death Collaborators. Global, regional, and national age-sex specific all-cause and cause-specific mortality for 240 causes of death, 1990-2013: a systematic analysis for the Global Burden of Disease Study 2013. *Lancet*. 2015;385(9963):117-171. doi:10.1016/S0140-6736(14)61682-2

4. Nichols M, Townsend N, Scarborough P, Rayner M. Cardiovascular disease in Europe 2014: epidemiological update. *European Heart Journal*. 2014;35(42):2950-2959. doi:10.1093/eurheartj/ehu299

5. Malakar AKr, Choudhury D, Halder B, Paul P, Uddin A, Chakraborty S. A review on coronary artery disease, its risk factors, and therapeutics. *Journal of Cellular Physiology*. 2019;234(10):16812-16823. doi:10.1002/jcp.28350

6. Patel SA, Winkel M, Ali MK, Narayan KMV, Mehta NK. Cardiovascular mortality associated with 5 leading risk factors: national and state preventable fractions estimated from survey data. *Ann Intern Med*. 2015;163(4):245-253. doi:10.7326/M14-1753

7. Pagliaro BR, Cannata F, Stefanini GG, Bolognese L. Myocardial ischemia and coronary disease in heart failure. *Heart Fail Rev*. 2020;25(1):53-65. doi:10.1007/s10741-019-09831-z

8. Pijls NH, De Bruyne B, Peels K, Van Der Voort PH, Bonnier HJ, Bartunek J Koolen JJ, Koolen JJ. Measurement of fractional flow reserve to assess the functional severity of coronary-artery stenoses. *N Engl J Med*. 1996;334(26):1703-1708. doi:10.1056/NEJM199606273342604

9. De Bruyne B, Fearon WF, Pijls NHJ, Barbato E, Tonino P, Piroth Z, Jagic N, Mobius-Winckler S, Rioufol G, Witt N, Kala P, MacCarthy P, Engström T, Oldroyd K, Mavromatis K, Manoharan G, Verlee P, Frobert O, Curzen N, Johnson JB, Limacher A, Nüesch E, Jüni P. Fractional Flow Reserve–Guided PCI for Stable Coronary Artery Disease. *New England Journal of Medicine*. 2014;371(13):1208-1217. doi:10.1056/NEJMoa1408758

10. Pijls NHJ, Fearon WF, Tonino PAL, Siebert U, Ikeno F, Bornschein B, van't Veer M, Klauss V, Manoharan G, Engstrøm T, Oldroyd KG, Ver Lee PN, MacCarthy PA, De Bruyne B. Fractional Flow Reserve Versus Angiography for Guiding Percutaneous Coronary Intervention in Patients With Multivessel Coronary Artery Disease: 2-Year Follow-Up of the FAME (Fractional Flow Reserve Versus Angiography for Multivessel Evaluation) Study. *Journal of the American College of Cardiology*. 2010;56(3):177-184. doi:10.1016/j.jacc.2010.04.012

11. Yancy Clyde W., Jessup Mariell, Bozkurt Biykem, Butler Javed, Casey Donald E., Colvin Monica M., Drazner Mark H., Filippatos Gerasimos S., Fonarow Gregg C., Givertz Michael M., Hollenberg Steven M., Lindenfeld JoAnn, Masoudi Frederick A., McBride Patrick E., Peterson Pamela N., Stevenson Lynne Warner, Westlake Cheryl. 2017 ACC/AHA/HFSA Focused Update of the 2013 ACCF/AHA Guideline for the Management of Heart Failure: A Report of the American College of Cardiology/American Heart Association Task Force on Clinical Practice Guidelines and the Heart Failure Society of America. *Circulation*. 2017;136(6):e137-e161. doi:10.1161/CIR.0000000000000509

12. Al-Khatib Sana M., Stevenson William G., Ackerman Michael J., Bryant William J., Callans David J., Curtis Anne B., Deal Barbara J., Dickfeld Timm, Field Michael E., Fonarow Gregg C., Gillis Anne M., Granger Christopher B., Hammill Stephen C., Hlatky Mark A., Joglar José A., Kay G. Neal, Matlock Daniel D., Myerburg Robert J., Page Richard L. 2017 AHA/ACC/HRS Guideline for Management of Patients With Ventricular Arrhythmias and the Prevention of Sudden Cardiac Death: Executive Summary. *Circulation*. 2018;138(13):e210-e271. doi:10.1161/CIR.0000000000000548

13. Nishimura Rick A., Otto Catherine M., Bonow Robert O., Carabello Blase A., Erwin John P., Fleisher Lee A., Jneid Hani, Mack Michael J., McLeod Christopher J., O'Gara Patrick T., Rigolin Vera H., Sundt Thoralf M., Thompson Annemarie. 2017 AHA/ACC Focused Update of the 2014 AHA/ACC Guideline for the Management of Patients With Valvular Heart Disease: A Report of the American College of Cardiology/American Heart Association Task Force on Clinical Practice Guidelines. *Circulation*. 2017;135(25):e1159-e1195. doi:10.1161/CIR.0000000000000503

14. Moss AJ, Zareba W, Hall WJ, Klein H, Wilber DJ, Cannom DS, Daubert JP, Higgins SL, Brown MW, Andrews ML, Multicenter Automatic Defibrillator Implantation Trial II Investigators. Prophylactic implantation of a defibrillator in patients with myocardial infarction and reduced ejection fraction. *N Engl J Med*. 2002;346(12):877-883. doi:10.1056/NEJMoa013474

15. Solomon SD, Anavekar N, Skali H, McMurray JJV, Swedberg K, Yusuf S, Granger CB, Michelson EL, Wang D, Pocock S, Pfeffer MA. Influence of Ejection Fraction on Cardiovascular Outcomes in a Broad Spectrum of Heart Failure Patients. *Circulation*. 2005;112(24):3738-3744. doi:10.1161/CIRCULATIONAHA.105.561423

16. Curtis JP, Sokol SI, Wang Y, Rathore SS, Ko DT, Jadbabaie F, Portnay EL, Marshalko SJ, Radford MJ, Krumholz HM. The association of left ventricular ejection fraction,

mortality, and cause of death in stable outpatients with heart failure. *J Am Coll Cardiol*. 2003;42(4):736-742. doi:10.1016/s0735-1097(03)00789-7

17. Nesbitt GC, Mankad S, Oh JK. Strain imaging in echocardiography: methods and clinical applications. *Int J Cardiovasc Imaging*. 2009;25 Suppl 1:9-22. doi:10.1007/s10554-008-9414-1

18. Kalam K, Otahal P, Marwick TH. Prognostic implications of global LV dysfunction: a systematic review and meta-analysis of global longitudinal strain and ejection fraction. *Heart*. 2014;100(21):1673-1680. doi:10.1136/heartjnl-2014-305538

19. Iacoviello M, Puzzovivo A, Guida P, Forleo C, Monitillo F, Catanzaro R, Lattarulo MS, Antoncecchi V, Favale S. Independent role of left ventricular global longitudinal strain in predicting prognosis of chronic heart failure patients. *Echocardiography*. 2013;30(7):803-811. doi:10.1111/echo.12142

20. Park JJ, Park JB, Park JH, Cho GY. Global Longitudinal Strain to Predict Mortality in Patients With Acute Heart Failure. *J Am Coll Cardiol*. 2018;71(18):1947-1957. doi:10.1016/j.jacc.2018.02.064

21. Cho GY, Marwick TH, Kim HS, Kim MK, Hong KS, Oh DJ. Global 2-dimensional strain as a new prognosticator in patients with heart failure. *J Am Coll Cardiol*. 2009;54(7):618-624. doi:10.1016/j.jacc.2009.04.061

22. Go AS, Mozaffarian D, Roger VL, Benjamin EJ, Berry JD, Borden WB, Bravata DM, Dai S, Ford ES, Fox CS, Franco S, Fullerton HJ, Gillespie C, Hailpern SM, Heit JA, Howard VJ, Huffman MD, Kissela BM, Kittner SJ, Lackland DT, Lichtman JH, Lisabeth LD, Magid D, Marcus GM, Marelli A, Matchar DB, McGuire DK, Mohler ER, Moy CS, Mussolino ME, Nichol G, Paynter NP, Schreiner PJ, Sorlie PD, Stein J, Turan TN, Virani SS, Wong ND, Woo D, Turner MB. Heart Disease and Stroke Statistics—2013 Update. *Circulation*. 2013;127(1):e6-e245. doi:10.1161/CIR.0b013e31828124ad

23. Sharma K, Kass DA. Heart failure with preserved ejection fraction: mechanisms, clinical features, and therapies. *Circ Res*. 2014;115(1):79-96. doi:10.1161/CIRCRESAHA.115.302922

24. Carluccio E, Tommasi S, Bentivoglio M, Buccolieri M, Prosciutti L, Corea L. Usefulness of the severity and extent of wall motion abnormalities as prognostic markers of an adverse outcome after a first myocardial infarction treated with thrombolytic therapy. *Am J Cardiol*. 2000;85(4):411-415. doi:10.1016/s0002-9149(99)00764-x

25. Moore CC, McVeigh ER, Zerhouni EA. Noninvasive measurement of three-dimensional myocardial deformation with tagged magnetic resonance imaging during graded local ischemia. *J Cardiovasc Magn Reson*. 1999;1(3):207-222. doi:10.3109/10976649909088333

26. Jurado-Román A, Agudo-Quílez P, Rubio-Alonso B, Molina J, Díaz B, García-Tejada J, Martín R, Tello R. Superiority of wall motion score index over left ventricle ejection

fraction in predicting cardiovascular events after an acute myocardial infarction. *Eur Heart J Acute Cardiovasc Care*. 2019;8(1):78-85. doi:10.1177/2048872616674464

27. Møller JE, Hillis GS, Oh JK, Reeder GS, Gersh BJ, Pellikka PA. Wall motion score index and ejection fraction for risk stratification after acute myocardial infarction. *Am Heart J*. 2006;151(2):419-425. doi:10.1016/j.ahj.2005.03.042

28. Cerqueira MD, Weissman NJ, Dilsizian V, Jacobs AK, Kaul S, Laskey WK, Pennell DJ, Rumberger JA, Ryan T, Verani MS, American Heart Association Writing Group on Myocardial Segmentation and Registration for Cardiac Imaging. Standardized myocardial segmentation and nomenclature for tomographic imaging of the heart. A statement for healthcare professionals from the Cardiac Imaging Committee of the Council on Clinical Cardiology of the American Heart Association. *Circulation*. 2002;105(4):539-542. doi:10.1161/hc0402.102975

29. Ortiz-Pérez JT, Rodríguez J, Meyers SN, Lee DC, Davidson C, Wu E. Correspondence Between the 17-Segment Model and Coronary Arterial Anatomy Using Contrast-Enhanced Cardiac Magnetic Resonance Imaging. *JACC: Cardiovascular Imaging*. 2008;1(3):282-293. doi:10.1016/j.jcmg.2008.01.014

30. Talaat M, Kharabish A, Homos MD, Fouad M, Nabil DM. The coronary arterial anatomy of the 17-segment model using 3-Tesla cardiac magnetic resonance imaging. *The Egyptian Journal of Radiology and Nuclear Medicine*. 2016;47(4):1303-1311. doi:10.1016/j.ejrnm.2016.06.021

31. Cury RC, Abbara S, Achenbach S, Agatston A, Berman DS, Budoff MJ, Dill KE, Jacobs JE, Maroules CD, Rubin GD, Rybicki FJ, Schoepf UJ, Shaw LJ, Stillman AE, White CS, Woodard PK, Leipsic JA. Coronary Artery Disease - Reporting and Data System (CAD-RADS): An Expert Consensus Document of SCCT, ACR and NASCI: Endorsed by the ACC. *JACC Cardiovasc Imaging*. 2016;9(9):1099-1113. doi:10.1016/j.jcmg.2016.05.005

32. Motoyama S, Ito H, Sarai M, Kondo T, Kawai H, Nagahara Y, Harigaya H, Kan S, Anno H, Takahashi H, Naruse H, Ishii J, Hecht H, Shaw LJ, Ozaki Y, Narula J. Plaque Characterization by Coronary Computed Tomography Angiography and the Likelihood of Acute Coronary Events in Mid-Term Follow-Up. *J Am Coll Cardiol*. 2015;66(4):337-346. doi:10.1016/j.jacc.2015.05.069

33. ACR–NASCI–SPR Practice Parameter for the Performance of Quantification of Cardiovascular Computed Tomography (CT) and Magnetic Resonance Imaging (MRI). :35.

34. Budoff MJ, Dowe D, Jollis JG, Gitter M, Sutherland J, Halamert E, Scherer M, Bellinger R, Martin A, Benton R, Delago A, Min JK. Diagnostic Performance of 64-Multidetector Row Coronary Computed Tomographic Angiography for Evaluation of Coronary Artery Stenosis in Individuals Without Known Coronary Artery Disease: Results From the Prospective Multicenter ACCURACY (Assessment by Coronary Computed Tomographic Angiography of Individuals Undergoing Invasive Coronary Angiography) Trial. *Journal*

of the American College of Cardiology. 2008;52(21):1724-1732. doi:10.1016/j.jacc.2008.07.031

35. Douglas PS, Hoffmann U, Patel MR, Mark DB, Al-Khalidi HR, Cavanaugh B, Cole J, Dolor RJ, Fordyce CB, Huang M, Khan MA, Kosinski AS, Krucoff MW, Malhotra V, Picard MH, Udelson JE, Velazquez EJ, Yow E, Cooper LS, Lee KL. Outcomes of Anatomical versus Functional Testing for Coronary Artery Disease. *New England Journal of Medicine*. 2015;372(14):1291-1300. doi:10.1056/NEJMoa1415516

36. The SCOT-HEART Inverstigators. Coronary CT Angiography and 5-Year Risk of Myocardial Infarction. *New England Journal of Medicine*. 2018;379(10):924-933. doi:10.1056/NEJMoa1805971

37. Goldstein JA, Chinnaiyan KM, Abidov A, Achenbach S, Berman DS, Hayes SW, Hoffmann U, Lesser JR, Mikati IA, O'Neil BJ, Shaw LJ, Shen MYH, Valeti US, Raff GL, CT-STAT Investigators. The CT-STAT (Coronary Computed Tomographic Angiography for Systematic Triage of Acute Chest Pain Patients to Treatment) trial. *J Am Coll Cardiol*. 2011;58(14):1414-1422. doi:10.1016/j.jacc.2011.03.068

38. Hoffmann U, Truong QA, Schoenfeld DA, Chou ET, Woodard PK, Nagurney JT, Pope JH, Hauser TH, White CS, Weiner SG, Kalanjian S, Mullins ME, Mikati I, Peacock WF, Zakroysky P, Hayden D, Goehler A, Lee H, Gazelle GS, Wiviott SD, Fleg JL, Udelson JE. Coronary CT Angiography versus Standard Evaluation in Acute Chest Pain. *New England Journal of Medicine*. 2012;367(4):299-308. doi:10.1056/NEJMoa1201161

39. Litt HI, Gatsonis C, Snyder B, Singh H, Miller CD, Entrikin DW, Leaming JM, Gavin LJ, Pacella CB, Hollander JE. CT Angiography for Safe Discharge of Patients with Possible Acute Coronary Syndromes. *New England Journal of Medicine*. 2012;366(15):1393-1403. doi:10.1056/NEJMoa1201163

40. Pack JD, Edic PM, Claus BEH, Iatrou M, Miller JV. Method for computed tomography motion estimation and compensation. Published online July 17, 2012. Accessed March 16, 2022. https://patents.google.com/patent/US8224056B2/en

41. Manohar A, Pack JD, Schluchter AJ, McVeigh ER. Four-dimensional computed tomography of the left ventricle, Part II: Estimation of mechanical activation times. *Medical Physics*. n/a(n/a). doi:10.1002/mp.15550

42. Stolzmann P, Goetti R, Baumueller S, Plass A, Falk V, Scheffel H, Feuchtner G, Marincek B, Alkadhi H, Leschka S. Prospective and retrospective ECG-gating for CT coronary angiography perform similarly accurate at low heart rates. *European Journal of Radiology*. 2011;79(1):85-91. doi:10.1016/j.ejrad.2009.12.016

43. Huang B, Li J, Law MWM, Zhang J, Shen Y, Khong PL. Radiation dose and cancer risk in retrospectively and prospectively ECG-gated coronary angiography using 64-slice multidetector CT. *Br J Radiol*. 2010;83(986):152-158. doi:10.1259/bjr/29879495

44. Yin X, Wang J, Zheng W, Ma J, Hao P, Chen Y. Diagnostic performance of coronary computed tomography angiography versus exercise electrocardiography for coronary artery disease: a systematic review and meta-analysis. *J Thorac Dis*. 2016;8(7):1688-1696. doi:10.21037/jtd.2016.06.06

45. Kim WY, Danias PG, Stuber M, Flamm SD, Plein S, Nagel E, Langerak SE, Weber OM, Pedersen EM, Schmidt M, Botnar RM, Manning WJ. Coronary magnetic resonance angiography for the detection of coronary stenoses. *N Engl J Med*. 2001;345(26):1863-1869. doi:10.1056/NEJMoa010866

46. Smiseth OA, Torp H, Opdahl A, Haugaa KH, Urheim S. Myocardial strain imaging: how useful is it in clinical decision making? *Eur Heart J*. 2016;37(15):1196-1207. doi:10.1093/eurheartj/ehv529

47. Ünlü S, Duchenne J, Mirea O, Pagourelias ED, Bézy S, Cvijic M, Beela AS, Thomas JD, Badano LP, Voigt JU, EACVI-ASE Industry Standardization Task Force. Impact of apical foreshortening on deformation measurements: a report from the EACVI-ASE Strain Standardization Task Force. *Eur Heart J Cardiovasc Imaging*. 2020;21(3):337-343. doi:10.1093/ehjci/jez189

48. Mondillo S, Galderisi M, Mele D, Cameli M, Lomoriello VS, Zacà V, Ballo P, D'Andrea A, Muraru D, Losi M, Agricola E, D'Errico A, Buralli S, Sciomer S, Nistri S, Badano L, Echocardiography Study Group Of The Italian Society Of Cardiology (Rome, Italy). Speckle-tracking echocardiography: a new technique for assessing myocardial function. *J Ultrasound Med*. 2011;30(1):71-83. doi:10.7863/jum.2011.30.1.71

49. Luis SA, Pellikka PA. Is Speckle Tracking Imaging Ready for Prime Time in Current Echo Clinical Practice? *Progress in Cardiovascular Diseases*. 2018;61(5):437-445. doi:10.1016/j.pcad.2018.11.001

50. Luis SA, Yamada A, Khandheria BK, Speranza V, Benjamin A, Ischenko M, Platts DG, Hamilton-Craig CR, Haseler L, Burstow D, Chan J. Use of three-dimensional speckle-tracking echocardiography for quantitative assessment of global left ventricular function: a comparative study to three-dimensional echocardiography. *J Am Soc Echocardiogr*. 2014;27(3):285-291. doi:10.1016/j.echo.2013.11.002

51. McVeigh ER, Atalar E. Cardiac tagging with breath-hold cine MRI. *Magn Reson Med*. 1992;28(2):318-327. doi:10.1002/mrm.1910280214

52. McVeigh ER. MRI of myocardial function: motion tracking techniques. *Magn Reson Imaging*. 1996;14(2):137-150. doi:10.1016/0730-725x(95)02009-i

53. Götte MJ, van Rossum AC, Twisk JWR null, Kuijer JPA null, Marcus JT, Visser CA. Quantification of regional contractile function after infarction: strain analysis superior to wall thickening analysis in discriminating infarct from remote myocardium. *J Am Coll Cardiol*. 2001;37(3):808-817. doi:10.1016/s0735-1097(00)01186-4

54. Zhang Q, Eagleson R, Peters TM. Volume visualization: a technical overview with a focus on medical applications. *J Digit Imaging*. 2011;24(4):640-664. doi:10.1007/s10278-010-9321-6

55. Nasis A, Moir S, Seneviratne SK, Cameron JD, Mottram PM. Assessment of left ventricular volumes, ejection fraction and regional wall motion with retrospective electrocardiogram triggered 320-detector computed tomography: a comparison with 2D-echocardiography. *Int J Cardiovasc Imaging*. 2012;28(4):955-963. doi:10.1007/s10554-011-9906-2

56. de Graaf FR, Schuijf JD, van Velzen JE, Nucifora G, Kroft LJ, de Roos A, Schalij MJ, Jukema JW, van der Wall EE, Bax JJ. Assessment of global left ventricular function and volumes with 320-row multidetector computed tomography: A comparison with 2D-echocardiography. *J Nucl Cardiol*. 2010;17(2):225-231. doi:10.1007/s12350-009-9173-y

57. Asferg C, Usinger L, Kristensen TS, Abdulla J. Accuracy of multi-slice computed tomography for measurement of left ventricular ejection fraction compared with cardiac magnetic resonance imaging and two-dimensional transthoracic echocardiography: a systematic review and meta-analysis. *Eur J Radiol*. 2012;81(5):e757-762. doi:10.1016/j.ejrad.2012.02.002

58. Ammon F, Bittner D, Hell M, Mansour H, Achenbach S, Arnold M, Marwan M. CT-derived left ventricular global strain: a head-to-head comparison with speckle tracking echocardiography. *Int J Cardiovasc Imaging*. 2019;35(9):1701-1707. doi:10.1007/s10554-019-01596-8

59. Bernhard B, Grogg H, Zurkirchen J, Demirel C, Hagemeyer D, Okuno T, Brugger N, De Marchi S, Huber AT, Berto MB, Spano G, Stortecky S, Windecker S, Pilgrim T, Gräni C. Reproducibility of 4D cardiac computed tomography feature tracking myocardial strain and comparison against speckle-tracking echocardiography in patients with severe aortic stenosis. *Journal of Cardiovascular Computed Tomography*. Published online January 31, 2022. doi:10.1016/j.jcct.2022.01.003

60. Ko SM, Kim YJ, Park JH, Choi NM. Assessment of left ventricular ejection fraction and regional wall motion with 64-slice multidetector CT: a comparison with two-dimensional transthoracic echocardiography. *BJR*. 2010;83(985):28-34. doi:10.1259/bjr/38829806

61. Sharma A, Einstein AJ, Vallakati A, Arbab-Zadeh A, Mukherjee D, Lichstein E. Meta-analysis of global left ventricular function comparing multidetector computed tomography with cardiac magnetic resonance imaging. *Am J Cardiol*. 2014;113(4):731-738. doi:10.1016/j.amjcard.2013.11.016

62. Kaniewska M, Schuetz GM, Willun S, Schlattmann P, Dewey M. Noninvasive evaluation of global and regional left ventricular function using computed tomography and magnetic resonance imaging: a meta-analysis. *Eur Radiol*. 2017;27(4):1640-1659. doi:10.1007/s00330-016-4513-1

63. Backhaus SJ, Metschies G, Billing M, Schmidt-Rimpler J, Kowallick JT, Gertz RJ, Lapinskas T, Pieske-Kraigher E, Pieske B, Lotz J, Bigalke B, Kutty S, Hasenfuß G, Kelle S, Schuster A. Defining the optimal temporal and spatial resolution for cardiovascular magnetic resonance imaging feature tracking. *Journal of Cardiovascular Magnetic Resonance*. 2021;23(1):60. doi:10.1186/s12968-021-00740-5

64. Tee M, Noble JA, Bluemke DA. Imaging techniques for cardiac strain and deformation: comparison of echocardiography, cardiac magnetic resonance and cardiac computed tomography. *Expert Rev Cardiovasc Ther*. 2013;11(2):221-231. doi:10.1586/erc.12.182

65. Hu JY, Bergquist PJ, Hossain R, Ropp AM, Kligerman S, Amin SB, Sechrist JW, Patel P, Jeudy J, White CS. Interobserver Reliability of the Coronary Artery Disease Reporting and Data System in Clinical Practice. *Journal of Thoracic Imaging*. 2021;36(2):95-101. doi:10.1097/RTI.0000000000000503

66. Sankaran S, Kim HJ, Choi G, Taylor CA. Uncertainty quantification in coronary blood flow simulations: Impact of geometry, boundary conditions and blood viscosity. *Journal of Biomechanics*. 2016;49(12):2540-2547. doi:10.1016/j.jbiomech.2016.01.002

67. Arbab-Zadeh A, Hoe J. Quantification of Coronary Arterial Stenoses by Multidetector CT Angiography in Comparison With Conventional Angiography: Methods, Caveats, and Implications. *JACC: Cardiovascular Imaging*. 2011;4(2):191-202. doi:10.1016/j.jcmg.2010.10.011

68. Dey D, Cheng VY, Slomka PJ, Nakazato R, Ramesh A, Gurudevan S, Germano G, Berman DS. Automated 3-dimensional quantification of noncalcified and calcified coronary plaque from coronary CT angiography. *Journal of Cardiovascular Computed Tomography*. 2009;3(6):372-382. doi:10.1016/j.jcct.2009.09.004

69. Renard F, Yang Y. Image analysis for detection of coronary artery soft plaques in MDCT images. In: *2008 5th IEEE International Symposium on Biomedical Imaging: From Nano to Macro*. ; 2008:25-28. doi:10.1109/ISBI.2008.4540923

70. Lavi G, Lessick J, Johnson PC, Khullar D. Single-seeded coronary artery tracking in CT angiography. In: *IEEE Symposium Conference Record Nuclear Science 2004.* Vol 5. ; 2004:3308-3311 Vol. 5. doi:10.1109/NSSMIC.2004.1466397

71. Bouraoui B, Ronse C, Baruthio J, Passat N, Germain Ph. Fully automatic 3D segmentation of coronary arteries based on mathematical morphology. In: *2008 5th IEEE International Symposium on Biomedical Imaging: From Nano to Macro*. ; 2008:1059-1062. doi:10.1109/ISBI.2008.4541182

72. Luengo-Oroz MA, Ledesma-Carbayo MJ, Gómez-Diego JJ, García-Fernández MA, Desco M, Santos A. Extraction of the Coronary Artery Tree in Cardiac Computer Tomographic Images Using Morphological Operators. In: Sachse FB, Seemann G, eds. *Functional Imaging and Modeling of the Heart*. Vol 4466. Lecture Notes in Computer Science. Springer Berlin Heidelberg; 2007:424-432. doi:10.1007/978-3-540-72907-5_43

73. Schaap M, Neefjes L, Metz C, van der Giessen A, Weustink A, Mollet N, Wentzel J, van Walsum TW, Niessen W. Coronary lumen segmentation using graph cuts and robust kernel regression. *Inf Process Med Imaging*. 2009;21:528-539. doi:10.1007/978-3-642-02498-6_44

74. Shahzad R, Kirişli H, Metz C, Tang H, Schaap M, van Vliet L, Niessen W, van Walsum T. Automatic segmentation, detection and quantification of coronary artery stenoses on CTA. *Int J Cardiovasc Imaging*. 2013;29(8):1847-1859. doi:10.1007/s10554-013-0271-1

75. Wang C, Moreno R. Vessel Segmentation Using Implicit Model-Guided Level Sets. *In: Proceedings of 3D Cardiovascular Imaging: A MICCAI Segmentation Challenge Workshop*. Published online 2012.

76. Lugauer F, Zheng Y, Hornegger J, Kelm BM. Precise Lumen Segmentation in Coronary Computed Tomography Angiography. In: Menze B, Langs G, Montillo A, Kelm M, Müller H, Zhang S, Cai W (Tom), Metaxas D, eds. *Medical Computer Vision: Algorithms for Big Data*. Springer International Publishing; 2014:137-147. doi:10.1007/978-3-319-13972-2_13

77. Lesage D, Angelini ED, Bloch I, Funka-Lea G. A review of 3D vessel lumen segmentation techniques: models, features and extraction schemes. *Med Image Anal*. 2009;13(6):819-845. doi:10.1016/j.media.2009.07.011

78. Hampe N, Wolterink JM, van Velzen SGM, Leiner T, Išgum I. Machine Learning for Assessment of Coronary Artery Disease in Cardiac CT: A Survey. *Frontiers in Cardiovascular Medicine*. 2019;6. Accessed March 22, 2022. https://www.frontiersin.org/article/10.3389/fcvm.2019.00172

79. Contijoch F, Stayman JW, McVeigh ER. The impact of small motion on the visualization of coronary vessels and lesions in cardiac CT: A simulation study. *Med Phys*. 2017;44(7):3512-3524. doi:10.1002/mp.12295

80. Chen Z, Contijoch F, Schluchter A, Grady L, Schaap M, Stayman W, Pack J, McVeigh E. Precise measurement of coronary stenosis diameter with CCTA using CT number calibration. *Med Phys*. 2019;46(12):5514-5527. doi:10.1002/mp.13862

81. Taylor CA, Fonte TA, Min JK. Computational fluid dynamics applied to cardiac computed tomography for noninvasive quantification of fractional flow reserve: scientific basis. *J Am Coll Cardiol*. 2013;61(22):2233-2241. doi:10.1016/j.jacc.2012.11.083

82. Tesche C, Vliegenthart R, Duguay TM, De Cecco CN, Albrecht MH, De Santis D, Langenbach MC, Varga-Szemes A, Jacobs BE, Jochheim D, Baquet M, Bayer RR, Litwin SE, Hoffmann E, Steinberg DH, Schoepf UJ. Coronary Computed Tomographic Angiography-Derived Fractional Flow Reserve for Therapeutic Decision Making. *Am J Cardiol*. 2017;120(12):2121-2127. doi:10.1016/j.amjcard.2017.08.034

83. Helle-Valle TM, Yu WC, Fernandes VRS, Rosen BD, Lima JAC. Usefulness of Radial Strain Mapping by Multidetector Computer Tomography to Quantify Regional

Myocardial Function in Patients With Healed Myocardial Infarction. *American Journal of Cardiology*. 2010;106(4):483-491. doi:10.1016/j.amjcard.2010.03.063

84. Buss SJ, Schulz F, Mereles D, Hosch W, Galuschky C, Schummers G, Stapf D, Hofmann N, Giannitsis E, Hardt SE, Kauczor HU, Katus HA, Korosoglou G. Quantitative analysis of left ventricular strain using cardiac computed tomography. *Eur J Radiol*. 2014;83(3):e123-130. doi:10.1016/j.ejrad.2013.11.026

85. Papademetris X, Sinusas AJ, Dione DP, Constable RT, Duncan JS. Estimation of 3-D left ventricular deformation from medical images using biomechanical models. *IEEE Trans Med Imaging*. 2002;21(7):786-800. doi:10.1109/TMI.2002.801163

86. Lamash Y, Fischer A, Carasso S, Lessick J. Strain Analysis From 4-D Cardiac CT Image Data. *IEEE Transactions on Biomedical Engineering*. 2015;62(2):511-521. doi:10.1109/TBME.2014.2359244

87. Pourmorteza Amir, Schuleri Karl H., Herzka Daniel A., Lardo Albert C., McVeigh Elliot R. A New Method for Cardiac Computed Tomography Regional Function Assessment. *Circulation: Cardiovascular Imaging*. 2012;5(2):243-250. doi:10.1161/CIRCIMAGING.111.970061

88. Myronenko A, Song X. Point Set Registration: Coherent Point Drift. *IEEE Transactions on Pattern Analysis and Machine Intelligence*. 2010;32(12):2262-2275. doi:10.1109/TPAMI.2010.46

89. Manohar A, Colvert GM, Schluchter A, Contijoch F, McVeigh ER. Anthropomorphic left ventricular mesh phantom: a framework to investigate the accuracy of SQUEEZ using Coherent Point Drift for the detection of regional wall motion abnormalities. *JMI*. 2019;6(4):045001. doi:10.1117/1.JMI.6.4.045001

90. Pourmorteza A, Chen MY, van der Pals J, Arai AE, McVeigh ER. Correlation of CT-based regional cardiac function (SQUEEZ) with myocardial strain calculated from tagged MRI: an experimental study. *Int J Cardiovasc Imaging*. 2016;32(5):817-823. doi:10.1007/s10554-015-0831-7

91. Manohar A, Colvert G, Ortuno J, Chen Z, Yang J, Colvert B, Bandettini WP, Chen MY, Ledesma-Carbayo M, McVeigh E. Regional left ventricular endocardial strains estimated from low-dose 4DCT: comparison with cardiac magnetic resonance feature tracking. *Medical Physics*. Published online 2022.

92. Yamashita R, Nishio M, Do RKG, Togashi K. Convolutional neural networks: an overview and application in radiology. *Insights Imaging*. 2018;9(4):611-629. doi:10.1007/s13244-018-0639-9

93. You C, Yang L, Zhang Y, Wang G. Low-dose CT via deep CNN with skip connection and network-in-network. In: *Developments in X-Ray Tomography XII*. Vol 11113. SPIE; 2019:429-434. doi:10.1117/12.2534960

94. You C, Li G, Zhang Y, Zhang X, Shan H, Li M, Ju S, Zhao Z, Zhang Z, Cong W, Vannier MW, Saha PK, Hoffman EA, Wang G. CT Super-Resolution GAN Constrained by the Identical, Residual, and Cycle Learning Ensemble (GAN-CIRCLE). *IEEE Transactions on Medical Imaging*. 2020;39(1):188-203. doi:10.1109/TMI.2019.2922960

95. Li Y, Li K, Zhang C, Montoya J, Chen GH. Learning to Reconstruct Computed Tomography Images Directly From Sinogram Data Under A Variety of Data Acquisition Conditions. *IEEE Transactions on Medical Imaging*. 2019;38(10):2469-2481. doi:10.1109/TMI.2019.2910760

96. Ye DH, Buzzard GT, Ruby M, Bouman CA. Deep Back Projection for Sparse-View CT Reconstruction. *arXiv:180702370 [cs, eess]*. Published online July 6, 2018. Accessed March 21, 2022. http://arxiv.org/abs/1807.02370

97. Chen H, Zhang Y, Kalra MK, Lin F, Chen Y, Liao P, Zhou J, Wang G. Low-Dose CT With a Residual Encoder-Decoder Convolutional Neural Network. *IEEE Transactions on Medical Imaging*. 2017;36(12):2524-2535. doi:10.1109/TMI.2017.2715284

98. Wang W, Gang GJ, Iv JWS. A CT denoising neural network with image properties parameterization and control. In: *Medical Imaging 2021: Physics of Medical Imaging*. Vol 11595. SPIE; 2021:136-141. doi:10.1117/12.2582145

99. You C, Yang Q, Shan H, Gjesteby L, Li G, Ju S, Zhang Z, Zhao Z, Zhang Y, Cong W, Wang G. Structurally-Sensitive Multi-Scale Deep Neural Network for Low-Dose CT Denoising. *IEEE Access*. 2018;6:41839-41855. doi:10.1109/ACCESS.2018.2858196

100. Wu P, Sheth N, Sisniega A, Wang T, Uneri A, Han R, Vijayan R, Vagdargi P, Kreher B, Kunze H, Kleinszig G, Vogt S, Lo SFL, Theodore N, Siewerdsen J. C-Arm Non-Circular Orbits: Geometric Calibration, Image Quality, and Avoidance of Metal Artifacts. Published online October 1, 2020. doi:10.48550/arXiv.2010.00175

101. Ghani MU, Karl WC. Fast Enhanced CT Metal Artifact Reduction using Data Domain Deep Learning. Published online April 9, 2019. doi:10.48550/arXiv.1904.04691

102. Zhang Y, Yu H. Convolutional Neural Network Based Metal Artifact Reduction in X-ray Computed Tomography. *IEEE Trans Med Imaging*. 2018;37(6):1370-1381. doi:10.1109/TMI.2018.2823083

103. Zhang C, Li Y, Chen GH. Accurate and robust sparse-view angle CT image reconstruction using deep learning and prior image constrained compressed sensing (DL-PICCS). *Medical Physics*. 2021;48(10):5765-5781. doi:10.1002/mp.15183

104. Hayes JW, Montoya J, Budde A, Zhang C, Li Y, Li K, Hsieh J, Chen GH. High Pitch Helical CT Reconstruction. *IEEE Transactions on Medical Imaging*. 2021;40(11):3077-3088. doi:10.1109/TMI.2021.3083210

105. Zhang C, Li Y, Li K, Chen GH. DeepInterior: new pathway to address the interior tomographic reconstruction problem in CT via direct backprojecting divergent beam

projection data. In: *Medical Imaging 2021: Physics of Medical Imaging*. Vol 11595. SPIE; 2021:453-458. doi:10.1117/12.2581368

106. Griner D, Garrett JW, Li Y, Li K, Chen GH. Correction for cone beam CT image artifacts via a deep learning method. In: *Medical Imaging 2020: Physics of Medical Imaging*. Vol 11312. SPIE; 2020:1104-1110. doi:10.1117/12.2549685

107. Kurakin A, Goodfellow I, Bengio S. Adversarial examples in the physical world. *arXiv:160702533 [cs, stat]*. Published online February 10, 2017. Accessed March 21, 2022. http://arxiv.org/abs/1607.02533

108. Zhang C, Li Y, Chen GH. Deep learning in image reconstruction: vulnerability under adversarial attacks and potential defense strategies. In: *Medical Imaging 2021: Physics of Medical Imaging*. Vol 11595. SPIE; 2021:482-488. doi:10.1117/12.2581369

109. Wu P, Sisniega A, Uneri A, Han R, Jones C, Vagdargi P, Zhang X, Luciano M, Anderson W, Siewerdsen J. Using Uncertainty in Deep Learning Reconstruction for Cone-Beam CT of the Brain. Published online August 20, 2021. doi:10.48550/arXiv.2108.09229

110. Wu W, Hu D, Cong W, Shan H, Wang S, Niu C, Yan P, Yu H, Vardhanabhuti V, Wang G. Stabilizing Deep Tomographic Reconstruction. Published online August 4, 2020. doi:10.48550/arXiv.2008.01846

111. Wang G, Ye JC, De Man B. Deep learning for tomographic image reconstruction. *Nat Mach Intell*. 2020;2(12):737-748. doi:10.1038/s42256-020-00273-z

112. Hwang TJ, Kesselheim AS, Vokinger KN. Lifecycle Regulation of Artificial Intelligence–and Machine Learning–Based Software Devices in Medicine. *JAMA*. 2019;322(23):2285-2286. doi:10.1001/jama.2019.16842

113. Choi AD, Marques H, Kumar V, Griffin WF, Rahban H, Karlsberg RP, Zeman RK, Katz RJ, Earls JP. CT Evaluation by Artificial Intelligence for Atherosclerosis, Stenosis and Vascular Morphology (CLARIFY): A Multi-center, international study. *Journal of Cardiovascular Computed Tomography*. 2021;15(6):470-476. doi:10.1016/j.jcct.2021.05.004

114. Dormer JD, Fei B, Halicek M, Ma L, Reilly CM, Schreibmann E. Heart chamber segmentation from CT using convolutional neural networks. In: Gimi B, Krol A, eds. *Medical Imaging 2018: Biomedical Applications in Molecular, Structural, and Functional Imaging*. Vol 10578. SPIE; 2018:100. doi:10.1117/12.2293554

115. Zreik M, Leiner T, de Vos BD, van Hamersvelt RW, Viergever MA, Isgum I. Automatic segmentation of the left ventricle in cardiac CT angiography using convolutional neural networks. In: *2016 IEEE 13th International Symposium on Biomedical Imaging (ISBI)*. IEEE; 2016:40-43. doi:10.1109/ISBI.2016.7493206

116. Mortazi A, Burt J, Bagci U. Multi-Planar Deep Segmentation Networks for Cardiac Substructures from MRI and CT. Published online August 2, 2017.

117. Wang C, Smedby Ö. Automatic Whole Heart Segmentation Using Deep Learning and Shape Context. In: Pop M, Sermesant M, Jodoin PM, Lalande A, Zhuang X, Yang G, Young A, Bernard O, eds. *Statistical Atlases and Computational Models of the Heart. ACDC and MMWHS Challenges*. Springer International Publishing; 2018:242-249.

118. Ronneberger O, Fischer P, Brox T. U-Net: Convolutional Networks for Biomedical Image Segmentation. In: Navab N, Hornegger J, Wells WM, Frangi AF, eds. *Medical Image Computing and Computer-Assisted Intervention -- MICCAI 2015*. Springer International Publishing; 2015:234-241.

119. Baskaran L, Maliakal G, Al'Aref SJ, Singh G, Xu Z, Michalak K, Dolan K, Gianni U, van Rosendael A, van den Hoogen I, Han D, Stuijfzand W, Pandey M, Lee BC, Lin F, Pontone G, Knaapen P, Marques H, Bax J, Berman D, Chang HJ, Shaw LJ, Min JK. Identification and Quantification of Cardiovascular Structures From CCTA: An End-to-End, Rapid, Pixel-Wise, Deep-Learning Method. *JACC: Cardiovascular Imaging*. 2020;13(5):1163-1171. doi:10.1016/j.jcmg.2019.08.025

120. Xu Z, Wu Z, Feng J. CFUN: Combining Faster R-CNN and U-net Network for Efficient Whole Heart Segmentation. *arXiv:181204914 [cs]*. Published online December 12, 2018. Accessed March 28, 2022. http://arxiv.org/abs/1812.04914

121. Wang C, MacGillivray T, Macnaught G, Yang G, Newby D. A two-stage 3D Unet framework for multi-class segmentation on full resolution image. *arXiv:180404341 [cs]*. Published online April 12, 2018. Accessed March 28, 2022. http://arxiv.org/abs/1804.04341

122. Vaswani A, Shazeer N, Parmar N, Uszkoreit J, Jones L, Gomez AN, Kaiser L, Polosukhin I. Attention Is All You Need. *arXiv:170603762 [cs]*. Published online December 5, 2017. Accessed April 12, 2022. http://arxiv.org/abs/1706.03762

123. You C, Zhao R, Liu F, Chinchali S, Topcu U, Staib L, Duncan JS. Class-Aware Generative Adversarial Transformers for Medical Image Segmentation. *arXiv:220110737 [cs, eess]*. Published online January 27, 2022. Accessed March 22, 2022. http://arxiv.org/abs/2201.10737

124. Chen J, Lu Y, Yu Q, Luo X, Adeli E, Wang Y, Lu L, Yuille AL, Zhou Y. TransUNet: Transformers Make Strong Encoders for Medical Image Segmentation. *arXiv:210204306 [cs]*. Published online February 8, 2021. Accessed March 22, 2022. http://arxiv.org/abs/2102.04306

125. Chen C, Qin C, Qiu H, Tarroni G, Duan J, Bai W, Rueckert D. Deep Learning for Cardiac Image Segmentation: A Review. *Front Cardiovasc Med*. 2020;7. doi:10.3389/fcvm.2020.00025

126. Chen Z, Rigolli M, Vigneault DM, Kligerman S, Hahn L, Narezkina A, Craine A, Lowe K, Contijoch F. Automated cardiac volume assessment and cardiac long- and short-axis imaging plane prediction from electrocardiogram-gated computed tomography volumes

enabled by deep learning. *European Heart Journal - Digital Health*. 2021;2(2):311-322. doi:10.1093/ehjdh/ztab033

127. Chen Z, Rigolli M, Vigneault D, Craine A, Contijoch F. Automated Multi-Chamber Segmentation And Imaging Plane Re-slicing Of Cardiac CT Images Via Deep Learning. *Journal of Cardiovascular Computed Tomography*. 2020;14(3):S20-S21. doi:10.1016/j.jcct.2020.06.017

128. Ferdian E, Suinesiaputra A, Fung K, Aung N, Lukaschuk E, Barutcu A, Maclean E, Paiva J, Piechnik SK, Neubauer S, Petersen SE, Young AA. Fully Automated Myocardial Strain Estimation from Cardiovascular MRI–tagged Images Using a Deep Learning Framework in the UK Biobank. *Radiology: Cardiothoracic Imaging*. 2020;2(1):e190032. doi:10.1148/ryct.2020190032

129. Zhang N, Yang G, Gao Z, Xu C, Zhang Y, Shi R, Keegan J, Xu L, Zhang H, Fan Z, Firmin D. Deep Learning for Diagnosis of Chronic Myocardial Infarction on Nonenhanced Caridac Cine MRI. *Radiology*. 2019;291(3):606-617. doi:10.1148/radiol.2019182304

130. Salte IM, Østvik A, Smistad E, Melichova D, Nguyen TM, Karlsen S, Brunvand H, Haugaa KH, Edvardsen T, Lovstakken L, Grenne B. Artificial Intelligence for Automatic Measurement of Left Ventricular Strain in Echocardiography. *JACC: Cardiovascular Imaging*. 2021;14(10):1918-1928. doi:10.1016/j.jcmg.2021.04.018

131. Morales MA, Boomen M van den, Nguyen C, Kalpathy-Cramer J, Rosen BR, Stultz CM, Izquierdo-Garcia D, Catana C. DeepStrain: A Deep Learning Workflow for the Automated Characterization of Cardiac Mechanics. *bioRxiv*. Published online January 7, 2021:2021.01.05.425266. doi:10.1101/2021.01.05.425266

132. Chen Z, Contijoch F, McVeigh E. Development of deep learning pipeline for direct observation of wall motion abnormality from 4DCT. In: *Medical Imaging 2022: Biomedical Applications in Molecular, Structural, and Functional Imaging*. Vol 12036. SPIE; 2022:429-439. doi:10.1117/12.2607387

133. Chen Z, Contijoch F, Colvert G, Manohar A, Kahn A, Narayan H, McVeigh E. Detection of Left Ventricular Wall Motion Abnormalities from Volume Rendering of 4DCT Cardiac Angiograms Using Deep Learning. *Frontiers in Cardiovascular Medicine*. Published online 2022. doi:10.3389/fcvm.2022.919751

134. Neglia Danilo, Rovai Daniele, Caselli Chiara, Pietila Mikko, Teresinska Anna, Aguadé-Bruix Santiago, Pizzi Maria Nazarena, Todiere Giancarlo, Gimelli Alessia, Schroeder Stephen, Drosch Tanja, Poddighe Rosa, Casolo Giancarlo, Anagnostopoulos Constantinos, Pugliese Francesca, Rouzet Francois, Le Guludec Dominique, Cappelli Francesco, Valente Serafina, Gensini Gian Franco, Zawaideh Camilla, Capitanio Selene, Sambuceti Gianmario, Marsico Fabio, Perrone Filardi Pasquale, Fernández-Golfín Covadonga, Rincón Luis M, Graner Frank P, de Graaf Michiel A., Fiechter Michael, Stehli Julia, Gaemperli Oliver, Reyes Eliana, Nkomo Sandy, Mäki Maija, Lorenzoni Valentina, Turchetti Giuseppe, Carpeggiani Clara, Marinelli Martina, Puzzuoli Stefano, Mangione Maurizio, Marcheschi Paolo, Mariani Fabio, Giannessi Daniela, Nekolla Stephan,

Lombardi Massimo, Sicari Rosa, Scholte Arthur J.H.A., Zamorano José L., Kaufmann Philipp A., Underwood S. Richard, Knuuti Juhani. Detection of Significant Coronary Artery Disease by Noninvasive Anatomical and Functional Imaging. *Circulation: Cardiovascular Imaging*. 2015;8(3):e002179. doi:10.1161/CIRCIMAGING.114.002179

135. Williams MC, Hunter A, Shah ASV, Assi V, Lewis S, Smith J, Berry C, Boon NA, Clark E, Flather M, Forbes J, McLean S, Roditi G, van Beek EJR, Timmis AD, Newby DE, SCOT-HEART Investigators. Use of Coronary Computed Tomographic Angiography to Guide Management of Patients With Coronary Disease. *J Am Coll Cardiol*. 2016;67(15):1759-1768. doi:10.1016/j.jacc.2016.02.026

136. Chen MY, Bandettini WP, Shanbhag SM, Vasu S, Booker OJ, Leung SW, Wilson JR, Kellman P, Hsu LY, Lederman RJ, Arai AE. Concordance and diagnostic accuracy of vasodilator stress cardiac MRI and 320-detector row coronary CTA. *Int J Cardiovasc Imaging*. Published online 2013. doi:10.1007/s10554-013-0300-0

137. ACR–NASCI–SPR. ACR–NASCI–SPR Practice Parameter for the Performance of Quantification of Cardiovascular Computed Tomography (CT) and Magnetic Resonance Imaging (MRI). 2014;1076(Revised 2008):1-28.

138. Pontone G, Bertella E, Mushtaq S, Loguercio M, Cortinovis S, Baggiano A, Conte E, Annoni A, Formenti A, Beltrama V, Guaricci AI, Andreini D. Coronary Artery Disease: Diagnostic Accuracy of CT Coronary Angiography—A Comparison of High and Standard Spatial Resolution Scanning. *Radiology*. 2014;271(3):688-694. doi:10.1148/radiol.13130909

139. Taylor CA, Fonte TA, Min JK. Computational fluid dynamics applied to cardiac computed tomography for noninvasive quantification of fractional flow reserve: Scientific basis. *Journal of the American College of Cardiology*. 2013;61(22):2233-2241. doi:10.1016/j.jacc.2012.11.083

140. Sankaran S, Kim HJ, Choi G, Taylor CA. Uncertainty quantification in coronary blood flow simulations: Impact of geometry, boundary conditions and blood viscosity. *Journal of Biomechanics*. 2016;49(12):2540-2547. doi:10.1016/j.jbiomech.2016.01.002

141. Contijoch F, Stayman JW, McVeigh ER. The impact of small motion on the visualization of coronary vessels and lesions in cardiac CT: A simulation study: A. *Medical Physics*. 2017;44(7):3512-3524. doi:10.1002/mp.12295

142. Rollano-Hijarrubia E, Stokking R, van der Meer F, Niessen WJ. Imaging of Small High-Density Structures in CT. A Phantom Study. *Academic Radiology*. 2006;13(7):893-908. doi:10.1016/j.acra.2006.03.009

143. Hoffmann KR, Nazareth DP, Miskolczi L, Gopal A, Wang Z, Rudin S, Bednarek DR. Vessel size measurements in angiograms: A comparison of techniques. *Medical Physics*. 2002;29(7):1622-1633. doi:10.1118/1.1488603

144. Tilley S, Jacobson M, Cao Q, Brehler M, Sisniega A, Zbijewski W, Stayman JW. Penalized-Likelihood Reconstruction with High-Fidelity Measurement Models for High-Resolution Cone-Beam Imaging. *IEEE Trans Med Imaging*. 2018;37(4):988-999. doi:10.1109/TMI.2017.2779406

145. Shechter G, Resar JR, McVeigh ER. Displacement and velocity of the coronary arteries: cardiac and respiratory motion. *IEEE Trans Med Imaging*. 2006;25(3):369-375. doi:10.1109/TMI.2005.862752

146. Pack JD, Edic PM, Claus BEH, Iatrou M, Miller JV. Method for computed tomography motion estimation and compensation. Published online 2012.

147. Suh YJ, Kim YJ, Kim JY, Chang S, Im DJ, Hong YJ, Choi BW. A whole-heart motion-correction algorithm: Effects on CT image quality and diagnostic accuracy of mechanical valve prosthesis abnormalities. *Journal of cardiovascular computed tomography*. 2017;11(6):474-481.

148. Soon J, Sulaiman N, Park JK, Kueh SHA, Naoum C, Murphy D, Ellis J, Hague CJ, Blanke P, Leipsic J. The effect of a whole heart motion-correction algorithm on CT image quality and measurement reproducibility in Pre-TAVR aortic annulus evaluation. *Journal of cardiovascular computed tomography*. 2016;10(5):386-390.

149. Lee TC, Kashyap RL, Chu CN. Building Skeleton Models via 3-D Medial Surface Axis Thinning Algorithms. *CVGIP: Graphical Models and Image Processing*. 1994;56(6):462-478. doi:10.1006/cgip.1994.1042

150. Lesage D, Angelini ED, Bloch I, Funka-Lea G. A review of 3D vessel lumen segmentation techniques: Models, features and extraction schemes. *Medical Image Analysis*. 2009;13(6):819-845. doi:10.1016/j.media.2009.07.011

151. Barrett JF, Keat N. Artifacts in CT: Recognition and Avoidance. *RadioGraphics*. 2004;24(6):1679-1691. doi:10.1148/rg.246045065

152. Richards T, Sturgeon GM, Ramirez-Giraldo JC, Rubin GD, Koweek LH, Segars WP, Samei E. Quantification of uncertainty in the assessment of coronary plaque in CCTA through a dynamic cardiac phantom and 3D-printed plaque model. *Journal of medical imaging (Bellingham, Wash)*. 2018;5(1):13501. doi:10.1117/1.JMI.5.1.013501

153. Fuchs TA, Stehli J, Dougoud S, Fiechter M, Sah BR, Buechel RR, Bull S, Gaemperli O, Kaufmann PA. Impact of a new motion-correction algorithm on image quality of low-dose coronary CT angiography in patients with insufficient heart rate control. *Academic Radiology*. 2014;21(3):312-317. doi:10.1016/j.acra.2013.10.014

154. Li Q, Li P, Su Z, Yao X, Wang Y, Wang C, Du X, Li K. Effect of a novel motion correction algorithm (SSF) on the image quality of coronary CTA with intermediate heart rates: Segment-based and vessel-based analyses. *European Journal of Radiology*. 2014;83(11):2024-2032. doi:10.1016/j.ejrad.2014.08.002

155. Min JK, Leipsic J, Pencina MJ, Berman DS, Koo BK, van Mieghem C, Erglis A, Lin FY, Dunning AM, Apruzzese P, Budoff MJ, Cole JH, Jaffer FA, Leon MB, Malpeso J, Mancini GB, Park SJ, Schwartz RS, Shaw LJ, Mauri L. Diagnostic accuracy of fractional flow reserve from anatomic CT angiography. *JAMA*. 2012;308(12):1237-1245. doi:10.1001/2012.jama.11274

156. Worz S, Rohr K. Segmentation and quantification of human vessels using a 3-D cylindrical intensity model. *IEEE transactions on image processing : a publication of the IEEE Signal Processing Society*. 2007;16(8):1994-2004.

157. Lardo AC, Rahsepar AA, Seo JH, Eslami P, Korley F, Kishi S, Abd T, Mittal R, George RT. Estimating coronary blood flow using CT transluminal attenuation flow encoding: Formulation, preclinical validation, and clinical feasibility. *Journal of cardiovascular computed tomography*. 2015;9(6):559-66.e1. doi:10.1016/j.jcct.2015.03.018

158. Moore CC, McVeigh ER, Zerhouni EA. Noninvasive Measurement of Three-Dimensional Myocardial Deformation with Tagged Magnetic Resonance Imaging During Graded Local Ischemia. *J Cardiovasc Magn Reson*. 1999;1(3):207-222.

159. Prinzen FW, Hunter WC, Wyman BT, McVeigh ER. Mapping of regional myocardial strain and work during ventricular pacing: experimental study using magnetic resonance imaging tagging. *J Am Coll Cardiol*. 1999;33(6):1735-1742. doi:10.1016/s0735-1097(99)00068-6

160. Yu Y, Villarraga HR, Saleh HK, Cha SS, Pellikka PA. Can ischemia and dyssynchrony be detected during early stages of dobutamine stress echocardiography by 2-dimensional speckle tracking echocardiography? *Int J Cardiovasc Imaging*. 2013;29(1):95-102. doi:10.1007/s10554-012-0074-9

161. Cheung Y fai. Functional Assessment for Congenital Heart Disease. *Korean Circ J*. 2014;44(2):59-73. doi:10.4070/kcj.2014.44.2.59

162. Valente AM, Cook S, Festa P, Ko HH, Krishnamurthy R, Taylor AM, Warnes CA, Kreutzer J, Geva T. Multimodality imaging guidelines for patients with repaired tetralogy of fallot: a report from the AmericanSsociety of Echocardiography: developed in collaboration with the Society for Cardiovascular Magnetic Resonance and the Society for Pediatric Radiology. *J Am Soc Echocardiogr*. 2014;27(2):111-141. doi:10.1016/j.echo.2013.11.009

163. Groves DW, Olivieri LJ, Shanbhag SM, Bronson KC, Yu JH, Nelson EA, Rollison SF, Stagliano MS, John AS, Kuehl K, Chen MY. Feasibility of low radiation dose retrospectively-gated cardiac CT for functional analysis in adult congenital heart disease. *International Journal of Cardiology*. 2017;228:180-183. doi:10.1016/j.ijcard.2016.11.108

164. McVeigh ER, Pourmorteza A, Guttman M, Sandfort V, Contijoch F, Budhiraja S, Chen Z, Bluemke DA, Chen MY. Regional myocardial strain measurements from 4DCT in patients with normal LV function. *J Cardiovasc Comput Tomogr*. 2018;12(5):372-378. doi:10.1016/j.jcct.2018.05.002

165. Colvert GM, Manohar A, Contijoch FJ, Yang J, Glynn J, Blanke P, Leipsic JA, McVeigh ER. Novel 4DCT Method to Measure Regional Left Ventricular Endocardial Shortening Before and After Transcatheter Mitral Valve Implantation. *Structural Heart*. 2021;5(4):410-419. doi:10.1080/24748706.2021.1934617

166. Contijoch FJ, Groves DW, Chen Z, Chen MY, McVeigh ER. A novel method for evaluating regional RV function in the adult congenital heart with low-dose CT and SQUEEZ processing. *Int J Cardiol*. 2017;249:461-466. doi:10.1016/j.ijcard.2017.08.040

167. Manohar A, Colvert GM, Yang J, Chen Z, Ledesma-Carbayo MJ, Kronborg MB, Sommer A, Nørgaard BL, Nielsen JC, McVeigh ER. Prediction of CRT Response Using a Lead Placement Score Derived from 4DCT. *medRxiv*. Published online March 24, 2022:2022.03.23.22272846. doi:10.1101/2022.03.23.22272846

168. Chen Z, Contijoch F, McVeigh E. Regional Shortening From 4DCT Demonstrates High Sensitivity And Specificity For Detecting LV Wall Motion Abnormalities From Clinical Scans. *Journal of Cardiovascular Computed Tomography*. 2021;15(4):S28. doi:10.1016/j.jcct.2021.06.219

169. Yushkevich PA, Piven J, Hazlett HC, Smith RG, Ho S, Gee JC, Gerig G. User-guided 3D active contour segmentation of anatomical structures: Significantly improved efficiency and reliability. *NeuroImage*. 2006;31(3):1116-1128. doi:10.1016/j.neuroimage.2006.01.015

170. Moore CC, Lugo-Olivieri CH, McVeigh ER, Zerhouni EA. Three-dimensional Systolic Strain Patterns in the Normal Human Left Ventricle: Characterization with Tagged MR Imaging. *Radiology*. 2000;214(2):453-466. doi:10.1148/radiology.214.2.r00fe17453

171. Adachi I, Morita K, Imran MB, Konno M, Mochizuki T, Kubo N, Itoh Y, Kato C, Tsukamoto E, Tamaki N. Heterogeneity of myocardial wall motion and thickening in the left ventricle evaluated with quantitative gated SPECT. *J Nucl Cardiol*. 2000;7(4):296-300. doi:10.1067/mnc.2000.104958

172. Fleiss JL. Measuring nominal scale agreement among many raters. *Psychological Bulletin*. 1971;76(5):378-382. doi:10.1037/h0031619

173. Pencina MJ, Steyerberg EW, D'Agostino RB. Extensions of net reclassification improvement calculations to measure usefulness of new biomarkers. *Stat Med*. 2011;30(1):11-21. doi:10.1002/sim.4085

174. Goette A, Kalman JM, Aguinaga L, Akar J, Cabrera JA, Chen SA, Chugh SS, Corradi D, D'Avila A, Dobrev D, Fenelon G, Gonzalez M, Hatem SN, Helm R, Hindricks G, Ho SY, Hoit B, Jalife J, Kim YH, Lip GYH, Ma CS, Marcus GM, Murray K, Nogami A, Sanders P, Uribe W, Van Wagoner DR, Nattel S, Group ESD, Centurion OA, Kuck KH, Patton KK, Sapp JL, Stiles M, Svendsen JH, Upadhyay GA, Coordinator R, Shantsila A. EHRA/HRS/APHRS/SOLAECE expert consensus on atrial cardiomyopathies: definition, characterization, and clinical implication. *Europace*. 2016;18(10):1455-1490. doi:10.1093/europace/euw161

175. Neglia D, Rovai D, Caselli C, Pietila M, Teresinska A, Aguadé-Bruix S, Pizzi MN, Todiere G, Gimelli A, Schroeder S, Drosch T, Poddighe R, Casolo G, Anagnostopoulos C, Pugliese F, Rouzet F, Le Guludec D, Cappelli F, Valente S, Gensini GF, Zawaideh C, Capitanio S, Sambuceti G, Marsico F, Perrone Filardi P, Fernández-Golfín C, Rincón LM, Graner FP, de Graaf MA, Fiechter M, Stehli J, Gaemperli O, Reyes E, Nkomo S, Mäki M, Lorenzoni V, Turchetti G, Carpeggiani C, Marinelli M, Puzzuoli S, Mangione M, Marcheschi P, Mariani F, Giannessi D, Nekolla S, Lombardi M, Sicari R, Scholte AJHA, Zamorano JL, Kaufmann PA, Underwood SR, Knuuti J. Detection of Significant Coronary Artery Disease by Noninvasive Anatomical and Functional Imaging. *Circulation: Cardiovascular Imaging*. 2015;8(3). doi:10.1161/CIRCIMAGING.114.002179

176. Hoffmann U, Truong QA, Schoenfeld DA, Chou ET, Woodard PK, Nagurney JT, Pope JH, Hauser TH, White CS, Weiner SG, Kalanjian S, Mullins ME, Mikati I, Peacock WF, Zakroysky P, Hayden D, Goehler A, Lee H, Gazelle GS, Wiviott SD, Fleg JL, Udelson JE. Coronary CT Angiography versus Standard Evaluation in Acute Chest Pain. *New England Journal of Medicine*. 2012;367(4):299-308. doi:10.1056/NEJMoa1201161

177. Hulten EA, Carbonaro S, Petrillo SP, Mitchell JD, Villines TC. Prognostic value of cardiac computed tomography angiography: a systematic review and meta-analysis. *J Am Coll Cardiol*. 2011;57(10):1237-1247. doi:10.1016/j.jacc.2010.10.011

178. Lu MT, Ersoy H, Whitmore AG, Lipton MJ, Rybicki FJ. Reformatted 4-Chamber and Short Axis Views of the Heart Using Thin Section (≤2mm) MDCT Images. *Acad Radiol*. 2007;14(9):1108-1112. doi:10.1016/j.acra.2007.05.019

179. Ecabert O, Peters J, Walker MJ, Ivanc T, Lorenz C, von Berg J, Lessick J, Vembar M, Weese J. Segmentation of the heart and great vessels in CT images using a model-based adaptation framework. *Med Image Anal*. 2011;15(6):863-876. doi:10.1016/j.media.2011.06.004

180. Litjens G, Ciompi F, Wolterink JM, de Vos BD, Leiner T, Teuwen J, Išgum I. State-of-the-Art Deep Learning in Cardiovascular Image Analysis. *JACC: Cardiovascular Imaging*. 2019;12(8, Part 1):1549-1565. doi:10.1016/j.jcmg.2019.06.009

181. Vigneault DM, Xie W, Ho CY, Bluemke DA, Noble JA. Ω-Net (Omega-Net): Fully automatic, multi-view cardiac MR detection, orientation, and segmentation with deep neural networks. *Medical Image Analysis*. 2018;48:95-106. doi:10.1016/j.media.2018.05.008

182. Kramer CM, Barkhausen J, Bucciarelli-Ducci C, Flamm SD, Kim RJ, Nagel E. Standardized cardiovascular magnetic resonance imaging (CMR) protocols: 2020 update. *Journal of cardiovascular magnetic resonance : official journal of the Society for Cardiovascular Magnetic Resonance*. 2020;22(1):17. doi:10.1186/s12968-020-00607-1

183. Vigneault DM, Xie W, Ho CY, Bluemke DA, Noble JA. Ω-Net (Omega-Net): Fully automatic, multi-view cardiac MR detection, orientation, and segmentation with deep neural networks. *Medical Image Analysis*. 2018;48:95-106. doi:10.1016/j.media.2018.05.008

184. Le M, Lieman-Sifry J, Lau F, Sall S, Hsiao A, Golden D. Computationally efficient cardiac views projection using 3D Convolutional Neural Networks. *arXiv:171101345 [cs]*. Published online November 3, 2017. Accessed October 21, 2020. http://arxiv.org/abs/1711.01345

185. Blansit K, Retson T, Masutani E, Bahrami N, Hsiao A. Deep Learning-based Prescription of Cardiac MRI Planes. *Radiol Artif Intell*. 2019;1(6):e180069. doi:10.1148/ryai.2019180069

186. Bai W, Sinclair M, Tarroni G, Oktay O, Rajchl M, Vaillant G, Lee AM, Aung N, Lukaschuk E, Sanghvi MM, Zemrak F, Fung K, Paiva JM, Carapella V, Kim YJ, Suzuki H, Kainz B, Matthews PM, Petersen SE, Piechnik SK, Neubauer S, Glocker B, Rueckert D. Automated cardiovascular magnetic resonance image analysis with fully convolutional networks. *Journal of Cardiovascular Magnetic Resonance*. 2018;20(1):65. doi:10.1186/s12968-018-0471-x

187. Levoy M. Display of surfaces from volume data. *IEEE Computer Graphics and Applications*. 1988;8(3):29-37. doi:10.1109/38.511

188. Cutroneo G, Bruschetta D, Trimarchi F, Cacciola A, Cinquegrani M, Duca A, Rizzo G, Alati E, Gaeta M, Milardi D. In Vivo CT Direct Volume Rendering: A Three-Dimensional Anatomical Description of the Heart. *Pol J Radiol*. 2016;81:21-28. doi:10.12659/PJR.895476

189. Zhang Q, Eagleson R, Peters TM. Dynamic real-time 4D cardiac MDCT image display using GPU-accelerated volume rendering. *Computerized Medical Imaging and Graphics*. 2009;33(6):461-476. doi:10.1016/j.compmedimag.2009.04.002

190. Mor-Avi V, Sugeng L, Lang RM. Real-time 3-dimensional echocardiography: an integral component of the routine echocardiographic examination in adult patients? *Circulation*. 2009;119(2):314-329. doi:10.1161/CIRCULATIONAHA.107.751354

191. Mori S, Takaya T, Kinugasa M, Ito T, Takamine S, Fujiwara S, Nishii T, Kono AK, Inoue T, Satomi-Kobayashi S, Rikitake Y, Okita Y, Hirata K ichi. Three-dimensional quantification and visualization of aortic calcification by multidetector-row computed tomography: A simple approach using a volume-rendering method. *Atherosclerosis*. 2015;239(2):622-628. doi:10.1016/j.atherosclerosis.2014.12.041

192. Tavakoli V, Sahba N. Cardiac motion and strain detection using 4D CT images: comparison with tagged MRI, and echocardiography. *Int J Cardiovasc Imaging*. 2014;30(1):175-184. doi:10.1007/s10554-013-0305-8

193. Gupta K, Sekhar N, Vigneault DM, Scott AR, Colvert B, Craine A, Raghavan A, Contijoch FJ. Octree Representation Improves Data Fidelity of Cardiac CT Images and Convolutional Neural Network Semantic Segmentation of Left Atrial and Ventricular Chambers. *Radiology: Artificial Intelligence*. Published online September 29, 2021:e210036. doi:10.1148/ryai.2021210036

194. Zreik M, Lessmann N, van Hamersvelt RW, Wolterink JM, Voskuil M, Viergever MA, Leiner T, Išgum I. Deep learning analysis of the myocardium in coronary CT angiography for identification of patients with functionally significant coronary artery stenosis. *Medical Image Analysis*. 2018;44:72-85. doi:10.1016/j.media.2017.11.008

195. Yushkevich PA, Piven J, Hazlett HC, Smith RG, Ho S, Gee JC, Gerig G. User-guided 3D active contour segmentation of anatomical structures: significantly improved efficiency and reliability. *Neuroimage*. 2006;31(3):1116-1128. doi:10.1016/j.neuroimage.2006.01.015

196. Szegedy C, Vanhoucke V, Ioffe S, Shlens J, Wojna Z. Rethinking the Inception Architecture for Computer Vision. *arXiv:151200567 [cs]*. Published online December 11, 2015. Accessed November 16, 2020. http://arxiv.org/abs/1512.00567

197. Deng J, Dong W, Socher R, Li LJ, Li K, Fei-Fei L. ImageNet: A large-scale hierarchical image database. In: *2009 IEEE Conference on Computer Vision and Pattern Recognition*. ; 2009:248-255. doi:10.1109/CVPR.2009.5206848

198. Hochreiter S, Schmidhuber J. Long Short-Term Memory. *Neural Comput*. 1997;9(8):1735-1780. doi:10.1162/neco.1997.9.8.1735

199. Kubo T, Akasaka T, Shite J, Suzuki T, Uemura S, Yu B, Kozuma K, Kitabata H, Shinke T, Habara M, Saito Y, Hou J, Suzuki N, Zhang S. OCT compared with IVUS in a coronary lesion assessment: the OPUS-CLASS study. *JACC Cardiovasc Imaging*. 2013;6(10):1095-1104. doi:10.1016/j.jcmg.2013.04.014

200. Gonzalo N, Escaned J, Alfonso F, Nolte C, Rodriguez V, Jimenez-Quevedo P, Bañuelos C, Fernández-Ortiz A, Garcia E, Hernandez-Antolin R, Macaya C. Morphometric Assessment of Coronary Stenosis Relevance With Optical Coherence Tomography: A Comparison With Fractional Flow Reserve and Intravascular Ultrasound. *J Am Coll Cardiol*. 2012;59(12):1080-1089. doi:10.1016/j.jacc.2011.09.078

201. Bezerra HG, Attizzani GF, Sirbu V, Musumeci G, Lortkipanidze N, Fujino Y, Wang W, Nakamura S, Erglis A, Guagliumi G, Costa MA. Optical coherence tomography versus intravascular ultrasound to evaluate coronary artery disease and percutaneous coronary intervention. *JACC Cardiovasc Interv*. 2013;6(3):228-236. doi:10.1016/j.jcin.2012.09.017

202. Pyxaras SA, Tu S, Barbato E, Barbati G, Di Serafino L, De Vroey F, Toth G, Mangiacapra F, Sinagra G, De Bruyne B, Reiber JHC, Wijns W. Quantitative angiography and optical coherence tomography for the functional assessment of nonobstructive coronary stenoses: comparison with fractional flow reserve. *Am Heart J*. 2013;166(6):1010-1018.e1. doi:10.1016/j.ahj.2013.08.016

203. Katsura M, Sato J, Akahane M, Kunimatsu A, Abe O. Current and Novel Techniques for Metal Artifact Reduction at CT: Practical Guide for Radiologists. *RadioGraphics*. 2018;38(2):450-461. doi:10.1148/rg.2018170102

204. Sarma KV, Harmon S, Sanford T, Roth HR, Xu Z, Tetreault J, Xu D, Flores MG, Raman AG, Kulkarni R, Wood BJ, Choyke PL, Priester AM, Marks LS, Raman SS, Enzmann D, Turkbey B, Speier W, Arnold CW. Federated learning improves site performance in multicenter deep learning without data sharing. *Journal of the American Medical Informatics Association*. 2021;28(6):1259-1264. doi:10.1093/jamia/ocaa341

205. Sheller MJ, Edwards B, Reina GA, Martin J, Pati S, Kotrotsou A, Milchenko M, Xu W, Marcus D, Colen RR, Bakas S. Federated learning in medicine: facilitating multi-institutional collaborations without sharing patient data. *Sci Rep*. 2020;10(1):12598. doi:10.1038/s41598-020-69250-1

206. Weiss J, Navab N. Deep Direct Volume Rendering: Learning Visual Feature Mappings From Exemplary Images. *arXiv:210605429 [cs]*. Published online June 9, 2021. Accessed April 2, 2022. http://arxiv.org/abs/2106.05429